TRANSPORTATION RESEARCH RECORD 945

Subgrade Moisture: Soil Properties, Foundations, Tunnel Reinforcement

TRANSPORTATION RESEARCH BOARD

NATIONAL RESEARCH COUNCIL
NATIONAL ACADEMY OF SCIENCES
WASHINGTON, D.C. 1983

Transportation Research Record 945
Price $8.20
Edited for TRB by Elizabeth W. Kaplan

modes
1 highway transportation
3 rail transportation
4 air transportation

subject areas
24 pavement design and performance
25 structures design and performance
61 soil exploration and classification
62 soil foundations
63 soil and rock mechanics
64 soil science

Library of Congress Cataloging in Publication Data
National Research Council. Transportation Research Board.
Subgrade moisture.

(Transportation research record; 945)
1. Pavements–Subgrades–Addresses, essays, lectures.
I. National Research Council (U.S.). Transportation Research Board. II. Series.
TE7.H5 no. 945 380.5s 84-20546 [TE250] [625.7'3]
ISBN 0-309-03666-6 ISSN 0361-1981

Sponsorship of the Papers in This Transportation Research Record

GROUP 2–DESIGN AND CONSTRUCTION OF TRANSPORTATION FACILITIES
Robert C. Deen, University of Kentucky, chairman

Construction Section
Garland W. Steele, West Virginia Department of Highways, chairman

Committee on Earthwork Construction
Charles M. Higgins, Louisiana Department of Transportation and Development, chairman
Mehmet C. Anday, Marvin L. Byington, Joseph D'Angelo, Robert C. Deen, Albert DiBernardo, William Bryan Greene, Wilbur M. Haas, William P. Hofmann, J.M. Hoover, Eugene Y. Huang, Robert W. Israel, James E. Kelly, Clyde N. Laughter, W. Scott Lovelace, C. William Lovell, Willard G. Puffer, John R. Sallberg, James Chris Schwarzhoff, Walter C. Waidelich

Soil Mechanics Section
Raymond A. Forsyth, California Department of Highways, chairman

Committee on Soils and Rock Instrumentation
William H. Hansmire, Parsons Brinckerhoff, chairman
Michael Bozozuk, Stephen F. Brown, Jerry C. Chang, John B. Gilmore, Gordon E. Green, Joseph B. Hannon, Robert D. Holtz, Richard H. Ledbetter, Verne C. McGuffey, Vincent G. Miller, Gregory N. Richardson, Ernest T. Selig, Anwar E.Z. Wissa

Committee on Foundations of Bridges and Other Structures
Bernard E. Butler, Reinforced Earth Company, chairman
Arnold Aronowitz, Michael Bozozuk, W. Dale Carney, Harry M. Coyle, Albert F. DiMillio, Bengt H. Fellenius, Frank M. Fuller, G.G. Goble, Richard J. Goettle III, James S. Graham, Hal W. Hunt, Gay D. Jones, Jr., Philip Keene, Hugh S. Lacy, Clyde N. Laughter, Robert M. Leary, G.A. Leonards, Richard P. Long, Lyle K. Moulton, Michael Wayne O'Neill, Arthur J. Peters, Alex Rutka, Harvey E. Wahls, John L. Walkinshaw, James Doyle Webb

Committee on Subsurface Soil-Structure Interaction
Michael G. Katona, University of Notre Dame, chairman
George Abdel-Sayed, John F. Abel, Baidar Bakht, Sangchul Bang, C.S. Desai, J.M. Duncan, Delon Hampton, An-Bin Huang, J. Neil Kay, Raymond J. Krizek, Richard W. Lautensleger, G.A. Leonards, Don A. Linger, Michael C. McVay, A.P. Moser, William Thomas Nearn II, Richard A. Parmelee, Russell B. Preuit, Jr., George W. Ring III, Ernest T. Selig, Corwin L. Tracy

Geology and Properties of Earth Materials Section
Clyde N. Laughter, Wisconsin Department of Transportation, chairman

Committee on Soil and Rock Properties
C. William Lovell, Purdue University, chairman
Robert K. Barrett, Roy H. Borden, William F. Brumund, Carl D. Ealy, James P. Gould, Kingsley Harrop-Williams, Robert D. Holtz, Robert B. Johnson, Ernest Jonas, Charles C. Ladd, Gerald P. Raymond, Surendra K. Saxena, Robert L. Schiffman, James J. Schnabel, J. Allan Tice, William D. Trolinger, Mehmet T. Tumay, Harvey E. Wahls, John L. Walkinshaw

Committee on Environmental Factors Except Frost
Malcolm L. Steinberg, Texas State Department of Highways and Public Transportation, chairman
S.S. Bandyopadhyay, Samuel H. Carpenter, T.Y. Chu, Charles Churilla, Barry J. Dempsey, Donald G. Fohs, A. Alexander Fungaroli, K.P. George, George R. Glenn, Richard L. Guthrie, Wilbur M. Haas, Badru M. Kiggundu, Robert P. Lottman, C. William Lovell, Robert L. Lytton, R. Gordon McKeen, Gene R. Morris, James M. Ritchie, Albert C. Ruckman, H.L. Schaaf, Shiraz D. Tayabji, T. Paul Teng, William G. Weber, Jr., Larry M. Younkin

William G. Gunderman and Neil F. Hawks, Transportation Research Board staff

Sponsorship is indicated by a footnote at the end of each report. The organizational units, officers, and members are as of December 31, 1982.

Contents

Authors of the Papers in This Record

Bandyopadhyay, S.S., NFS Services, Inc., 5814 Heffernan Street, Houston, Tex. 77087
Bang, S., Department of Civil Engineering, University of Notre Dame, Notre Dame, Ind. 46556
Brown, Bruce E., Department of Geological and Geophysical Sciences, University of Wisconsin-Milwaukee, Milwaukee, Wis. 53201
Das, Braja M., Civil Engineering Department, The University of Texas at El Paso, El Paso, Tex. 79968
DiBernardo, Albert, Tippetts-Abbett-McCarthy-Stratton, 655 3rd Avenue, New York, N.Y. 10017
Frantzen, J.A., Kansas Department of Transportation, 2300 Van Buren, Topeka, Kans. 66611
Jeyapalan, Jey K., Texas Transportation Institute, Texas A&M University, College Station, Tex. 77843
Larbi-Cherif, Said, Robert Navarro and Associates, 1444 Montana Avenue, El Paso, Tex. 79902
Liu, Shang J., Texas Transportation Institute, Texas A&M University, College Station, Tex. 77843
Lovell, C.W., Department of Civil Engineering, Purdue University, West Lafayette, Ind. 47907
Lytton, Robert L., Texas Transportation Institute, Texas A&M University, College Station, Tex. 77843
Mengel, J.T., Investors Diversified Services, IDS Tower, 80 South 8th Street, Minneapolis, Minn. 55402
Picornell, Miguel, Texas Transportation Institute, Texas A&M University, College Station, Tex. 77843
Rozendal, David B., Civil Engineering Department, The University of Texas at El Paso, El Paso, Tex. 79968
Steinberg, Malcolm, Texas Transportation Institute, Texas A&M University, College Station, Tex. 77843

Characteristics of Base and Subgrade Drainage of Pavements

SHANG J. LIU, JEY K. JEYAPALAN, AND ROBERT L. LYTTON

Base courses beneath highway and airport pavements that become saturated are reduced in modulus and bearing capacity, and pumping may develop at pavement joints. Base-course drainage is often required to preclude this major cause of pavement deterioration. A number of theoretical models for developing design guidelines for drainage requirements of pavements are discussed; the models include the original one by Casagrande and Shannon, which assumed a straight-line phreatic surface and an impermeable subgrade. The influence of subgrade drainage on drainage time and the influence of the use of the more theoretically correct parabolic phreatic surface, especially in deep base courses or on flat slopes, are found to be substantial. New models are developed to include these features and the calculated results are, in general, in good agreement with field data observed on full-scale pavements. Example calculations are presented to illustrate the effect of subgrade drainage on the drainage time for base courses.

A complex interaction among the pavement section, traffic, and environmental conditions influences the performance of pavements. Some of the most detrimental interactions occur more rapidly when excess water is in the base course. As the water content of the base course and subgrade increases, load-bearing capacity and modulus are reduced significantly, and pumping, stripping, and disintegration of stabilized materials increase. Therefore, proper drainage of base course and subgrade must be provided (see Figure 1). The design of highway subdrainage requires a proper analysis of the drainage characteristics of these two layers.

Base-course drainage has received considerable attention during the last 30 years. Casagrande and Shannon (1) made field observations on several airfields in the United States to determine the environmental conditions under which base courses may become saturated. Most of the observations were limited to the two principal causes for the saturation of base courses--frost action and infiltration through the surface course. Casagrande and Shannon (1) made detailed observations of groundwater levels in the subgrade and in the base course beneath both concrete and bituminous pavements at six airfields in Maine, Wisconsin, Michigan, North Dakota, and South Dakota. The discharge through the base-course drainage pipes was also monitored at these fields. Based on these observations they concluded that, during the thawing period, ice segregation in a subgrade may cause saturation of an overlying, free-draining base. They also concluded that infiltration of surface water through pavement cracks, or joints, may cause saturation of a free-draining base that overlies a relatively impervious subgrade. Other causes for the saturation of bases may be inundation of the pavement in an area that might be flooded during certain times of the year or where the natural water table may rise above the bottom of the base course.

Casagrande and Shannon (1) also performed a simplified theoretical analysis of the base-course drainage. They assumed symmetry along the axis of the pavement and developed the equations that govern drainage for one-half of the cross section of the base-course layer ABCD. Figure 2 shows the drainage process divided into two parts. In the first part the free surface gradually changes from position CD to CA because of free drainage through the open edge (CD) of the pavement. Darcy's law and the continuity equation were satisfied to establish a relation among time (t) and x(t) in terms of H, L, α, k_1, and n_1, as shown in Figure 2. In the second part of the figure the free surface rotates from position CA to CB because of the loss of water through the face CD. The subgrade is assumed to be impervious through the entire flow calculation. Casagrande and Shannon (1) established a relation among t and h(t) in terms of other parameters mentioned previously.

Further details and drainage equations are presented in the following sections of this paper. The theoretical results were compared with field observations by Casagrande and Shannon (1), and the deviations between theory and field results are primarily due to the assumptions that the phreatic surface is a straight line and the subgrade is impervious. Later Barber and Sawyer (2) presented Casagrande and Shannon's (1) equations in the form of a dimensionless chart (see Figure 3). Recently Cedergren (3) and Moulton (4) have modified the original definition of the slope factor (S) as the reciprocal of the one shown in Figure 3 and have presented similar drainage charts in their work on highway subdrainage design.

Casagrande and Shannon (1) noted that as the slope of the pavement (tan α) became flatter or the depth of the base (H) became greater, predictions differed more widely from observations. To

Figure 1. Cross section of pavement.

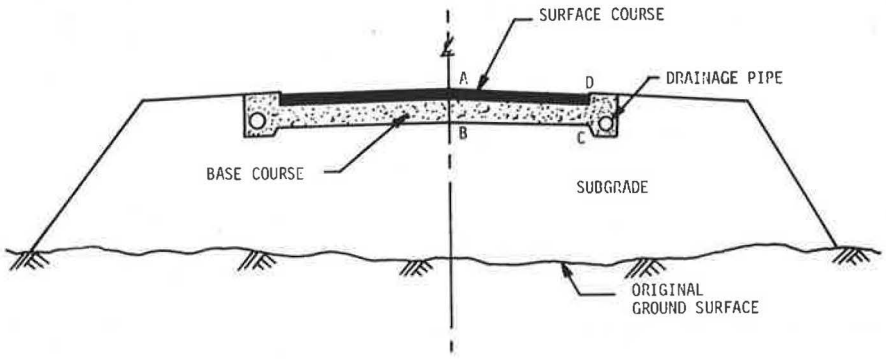

Figure 2. Casagrande-Shannon model for base-course drainage.

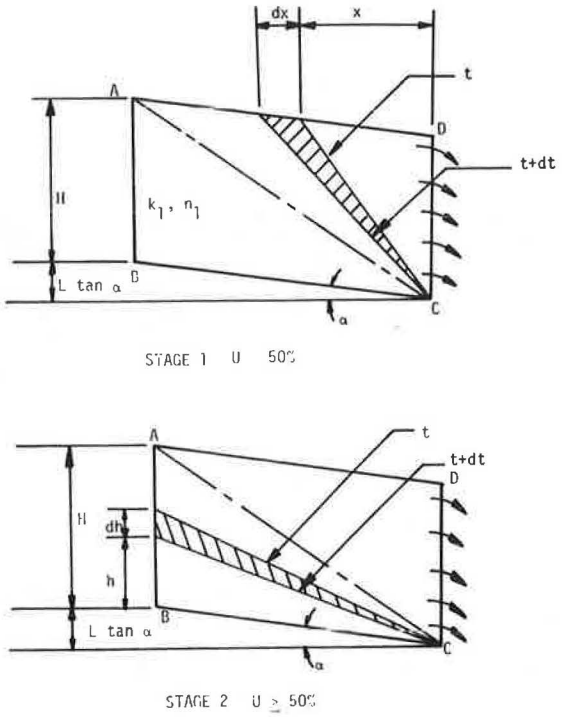

account for this difference Casagrande and Shannon (1) introduced a correction factor that depended on these variables. Also, in the cases reported in this paper, the base course took longer to drain than the theory predicted. Because the Casagrande-Shannon theory underpredicts the amount of time that a base course is wet, which is not conservative especially in the deeper and flatter pavements, a better means was needed for analyzing the drainage from base courses.

In order to develop better analytic procedures for pavement drainage design, a parabolic phreatic surface and a permeable subgrade were used in this research study. The details of these improved analytic models, the numerical results from these models, and their applicability to pavement subdrainage design are discussed in the following sections.

ANALYSES OF BASE DRAINAGE

Drainage of a sloping layer of base course involves an unsteady flow with a phreatic surface. The assumptions of Casagrande and Shannon (1) lead to the simple model shown in Figure 2. In this model the center line of the base course (AB) and the bottom of the base course (BC) are considered to be impervious boundaries. Free discharge is assumed along the outer edge of the base course (CD). When drainage begins, the base layer is assumed to be saturated, and the face CD is immediately opened for free drainage. In the Casagrande-Shannon model the phreatic surface is assumed to be a straight line that rotates with time, as shown in Figure 2. The problem was solved in two parts and the solutions were presented in the following dimensionless form. Noted that U is the degree of drainage, S is the slope factor, and T is the time factor.

For horizontal bases,

Stage 1:

$$0 \leq U \leq 50 \text{ percent} \tag{1a}$$

and

$$T = 2U^2 \tag{1b}$$

Stage 2:

$$50 \text{ percent} \leq U < 100 \text{ percent} \tag{2a}$$

and

$$T = U/(2 - 2U) \tag{2b}$$

For sloping bases,

Stage 1:

Figure 3. Variation of drainage area with slope factor and time factor (after Casagrande and Shannon).

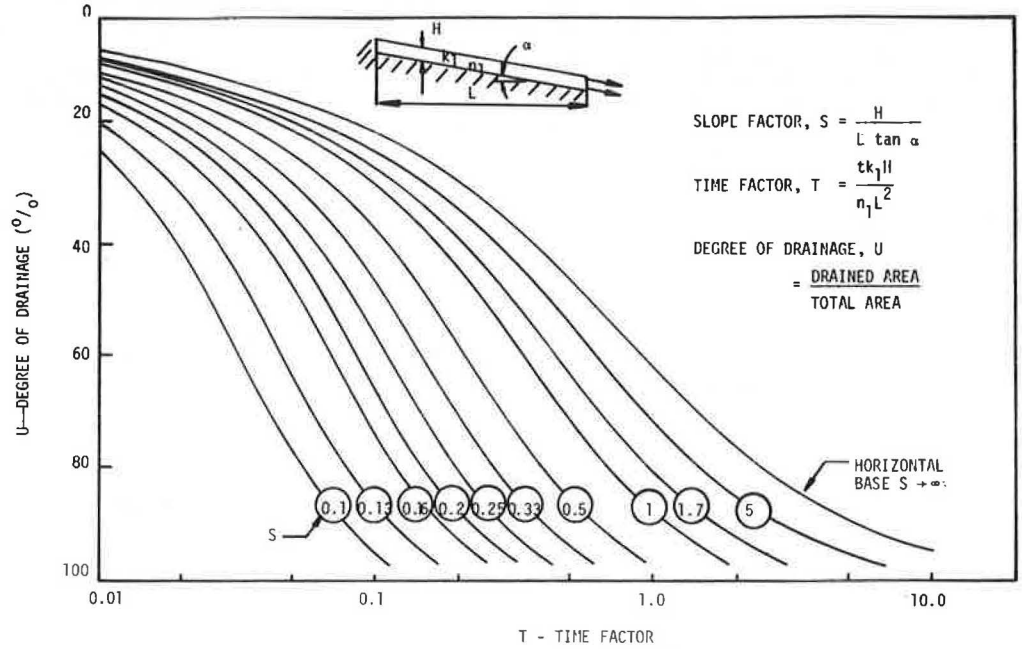

$0 \leq U \leq 50$ percent (3a)

and

$$T = 2US - S^2 \ln [(S + 2U)/S] \quad (3b)$$

Stage 2:

50 percent $\leq U <$ 100 percent (4a)

and

$$T = S + S \ln [(2S - 2US + 1)/(2 - 2U)(S + 1)] - S^2 \ln [(S + 1)/S] \quad (4b)$$

where

U = drained area/total area,
S = H/L tan α,
T = tk_1H/n_1L^2,
H = thickness of base course,
L = one-half the width of the pavement,
α = slope angle,
t = time,
k_1 = coefficient of permeability of base course, and
n_1 = porosity of base course.

The Casagrande-Shannon model has been used extensively by Barber and Sawyer (2), Cedergren (3), Moulton (4), and Markow (5) in the form of a chart shown in Figure 3. However, the theoretical analyses reported by Wallace and Leonardi (6) indicate that the phreatic surface assumes a shape closer to a parabola than a straight line. Dupuit's assumption, as used in related drainage problems by Polubarinova-Kochina (7), also suggests that a parabolic phreatic surface would yield more realistic results for drainage calculations.

To compare the effects of a parabolic phreatic surface with those of the straight line assumed by Casagrande and Shannon (1) an impermeable subgrade was assumed and the resulting drainage equations were developed. Two separate stages were identified (see Figure 4) and the corresponding equations are as follows.

For horizontal bases,

Stage 1:

$0 \leq U \leq 1/3$ (5a)

and

$$T = 3U^2 \quad (5b)$$

Stage 2:

$1/3 \leq U < 1$ (6a)

and

$$T = (8/9)[1/(1 - U)] - 1 \quad (6b)$$

For sloping bases,

Stage 1:

$0 \leq U \leq 1/3$ (7a)

and

$$T = (3/2)SU - (3/8)S^2 \ln [(S + 4U)/S] \quad (7b)$$

Stage 2:

$1/3 \leq U < 1$ (8a)

and

$$T = (S/2) - (3/8)S^2 \ln [(3S + 4)/3S] + S \ln [(9S - 9SU + 8)/3(1 - U)(3S + 4)] \quad (8b)$$

Figure 4. TTI model for base-course drainage with impermeable subgrade.

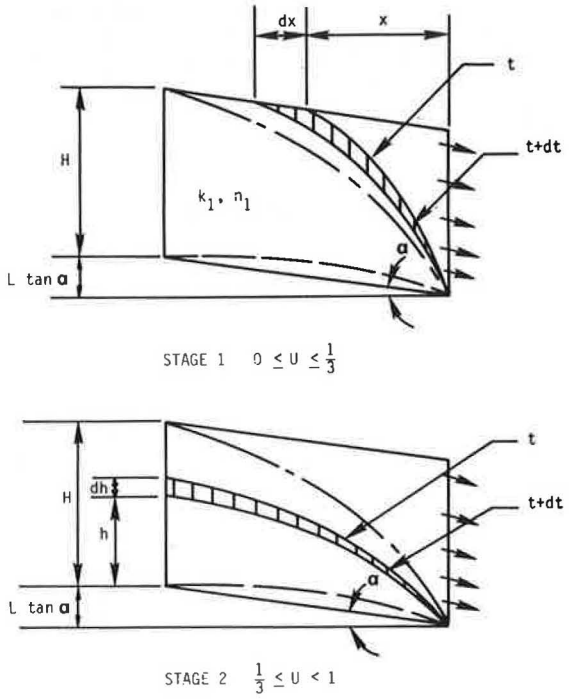

The results of these drainage equations are presented in the form of a dimensionless drainage chart in Figure 5. The results from the new model are compared with field data reported by Casagrande and Shannon (1) on three of their five pavement test sections shown in Figures 6 through 8. In the Texas Transportation Institute (TTI) model, drainage proceeds more slowly than in the Casagrande-Shannon model but has roughly the same shape.

The TTI model could be made to better fit the field data if drainage were allowed to infiltrate a permeable subgrade, thus increasing the initial degree of drainage and shortening the drainage time.

ANALYSES OF BASE AND SUBGRADE DRAINAGE

Two models were developed to study the influence of subgrade drainage on base-course drainage. In these models the phreatic surfaces in the base course were assumed to be linear and parabolic. The two distinct stages of drainage in the first permeable subgrade model are shown in Figure 9. In this model the properties of the subgrade are defined by the coefficient of permeability (k_2) and porosity (n_2). An advancing wetting front (FG) was assumed at an unknown depth of $y_o(t)$ (see Figure 10). The drainage problem, similar to that of the Casagrande-Shannon model, begins with a saturated base-subgrade composite system and the faces EC and DC are opened immediately to allow free drainage. To keep the model simple a one-dimensional flow into the subgrade is assumed (7). Based on this formulation the

velocity of drainage (v) into the subgrade is given by

$$v = [y_o(t) + h(t) - H] / \left([h(t)/k_1] - \{ [y_o(t) - H]/k_2 \} \right) \quad (9)$$

$$y_o(t) = H + (n_1/n_2)\,[H - h(t)] \quad (10)$$

where

$h(t)$ = depth of water in the base course,
$y_o(t)$ = penetration of water into the subgrade,
k_1, n_1 = coefficient of permeability and porosity of the base course, and
k_2, n_2 = coefficient of permeability and porosity of the subgrade.

The modified differential equations for this model do not yield a set of dimensionless variables that permit the preparation of dimensionless drainage charts. Furthermore, the governing equations are too complex to generate any closed-form solutions. A numerical integration scheme was used to solve these governing equations, and the results of four of the five test sections are shown in Figures 11 through 14. In these plots the results from the permeable subgrade using the linear phreatic surface model are shown with the field data reported by Casagrande and Shannon (1).

In Figure 11 the field data are enveloped between the curves for the impermeable subgrade and the subgrade with a permeability that is 10 times

Figure 5. TTI drainage chart with impermeable subgrade.

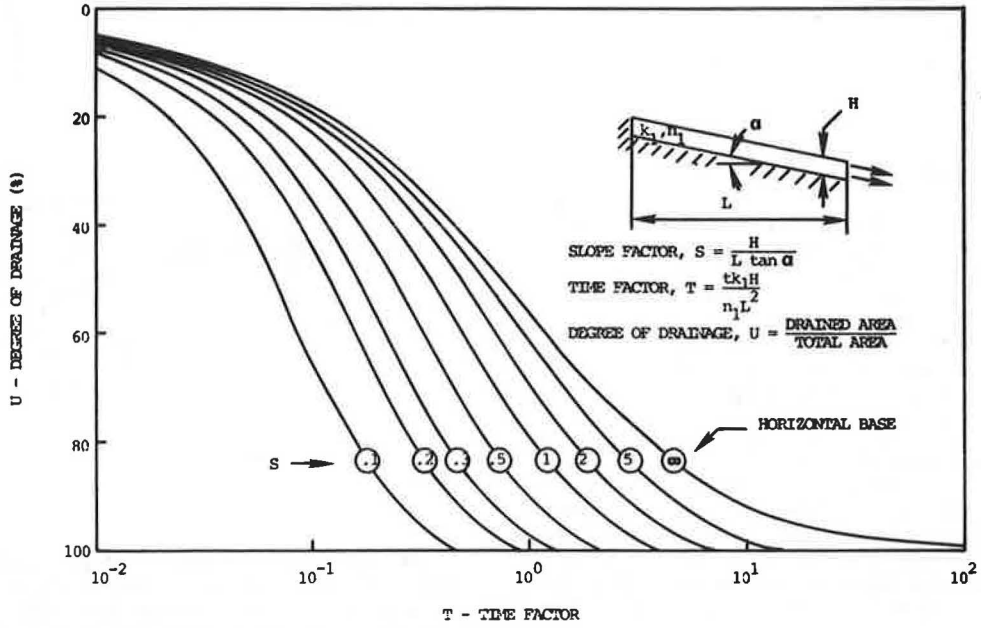

Figure 6. Comparison of results for impermeable subgrade: $n_1 = 0.07$.

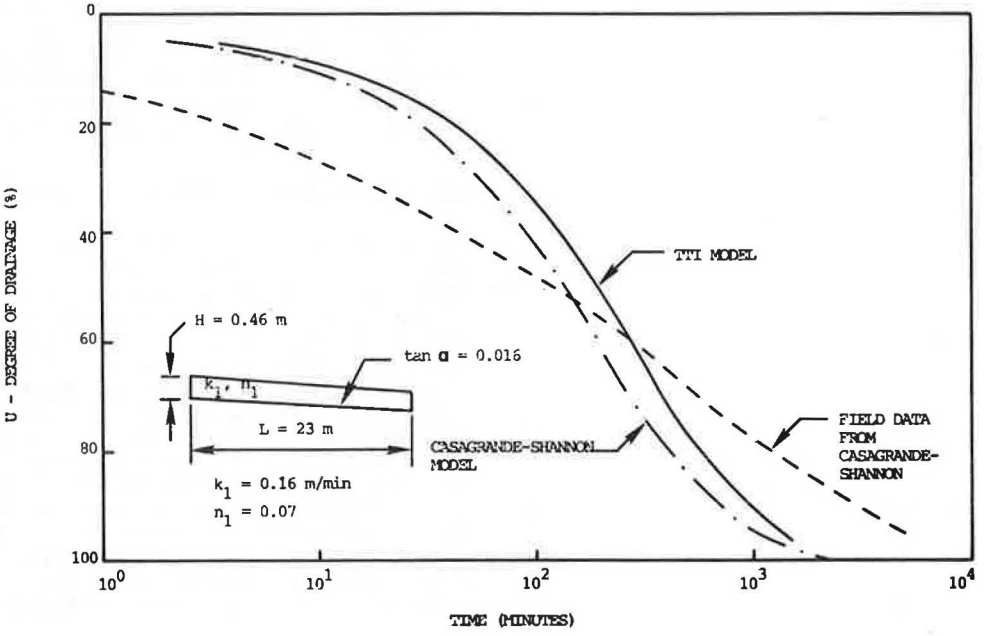

Figure 7. Comparison of results for impermeable subgrade: $n_1 = 0.43$.

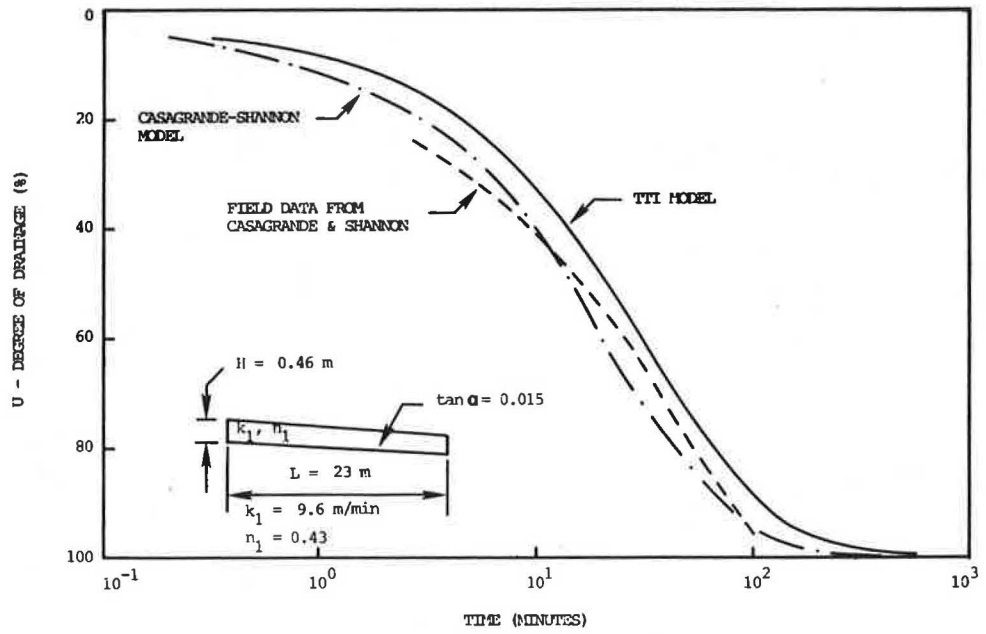

Figure 8. Comparison of results for impermeable subgrade: $n_1 = 0.04$.

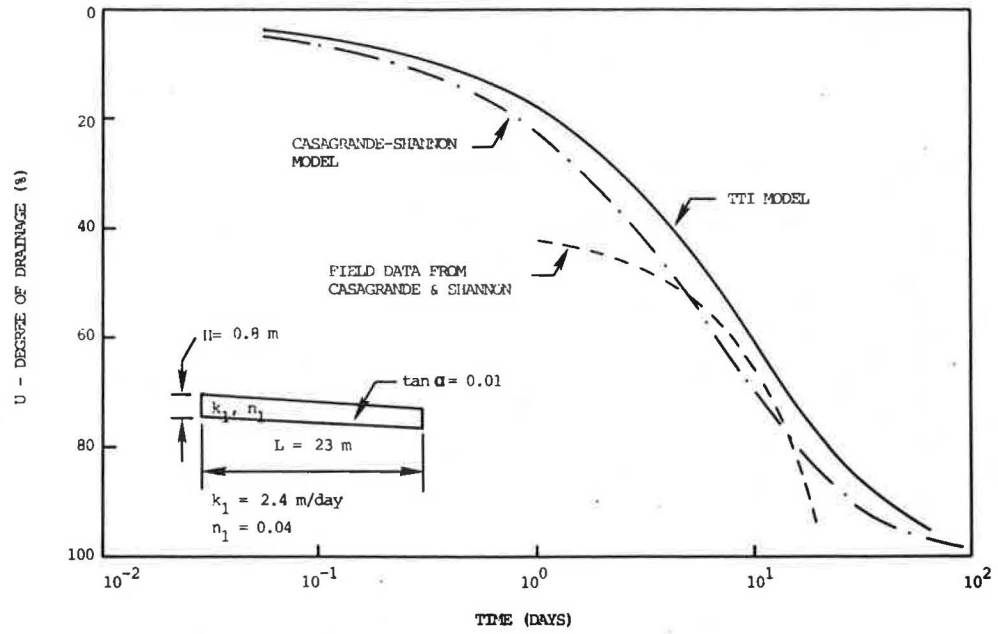

smaller than that of the base course. In Figure 12 both the initial and long-term drainage occur more quickly than predicted by the Casagrande-Shannon model. Figures 11 and 12 indicate the need for including subgrade drainage in a drainage model. In Figures 13 and 14 drainage under field conditions takes longer than predicted by the Casagrande-Shannon model that assumes an impervious subgrade. These two figures indicate the need for a base-course drainage analysis that can account for longer drainage periods. These two requirements, taken together, suggest that the parabolic phreatic surface model with a permeable subgrade may be capable of more realistic predictions. The model includes the same two stages that were identified in Figure 4 and illustrated in Figure 15.

Three of the five field cases were studied using this model, and the results for two of the field cases are shown in Figures 16 and 17, which correspond to Figures 13 and 11. Note that in Figure 16 the field curve follows a trend similar to that of the two drainage curves ($k_2/k_1 = K=0$ and 0.0002) given by the current model and lies between the two theoretical curves. In this case the permeable subgrade model with a parabolic phreatic surface yields results that compare well with field data.

Figure 9. Permeable subgrade with Casagrande-Shannon drainage model.

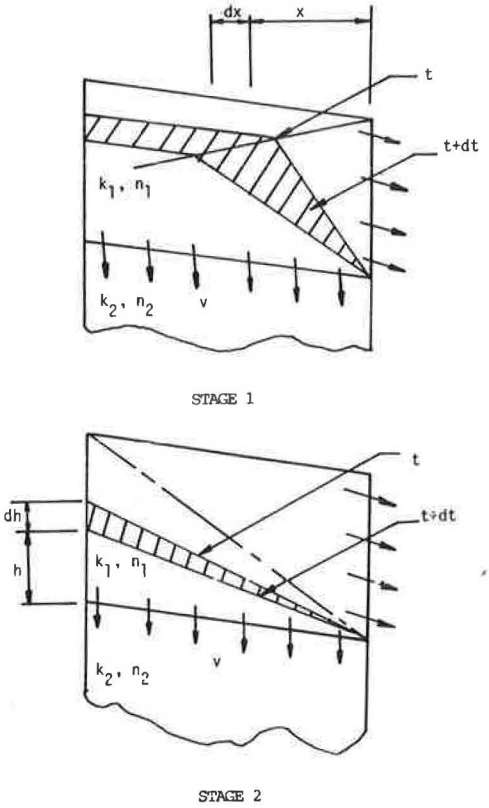

Figure 10. Definition sketch for subgrade drainage model.

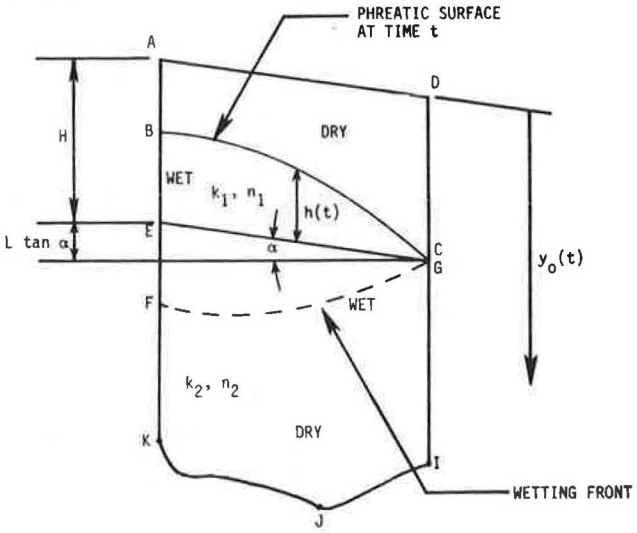

Figure 11. Results of Casagrande-Shannon model with permeable subgrades: test section 1.

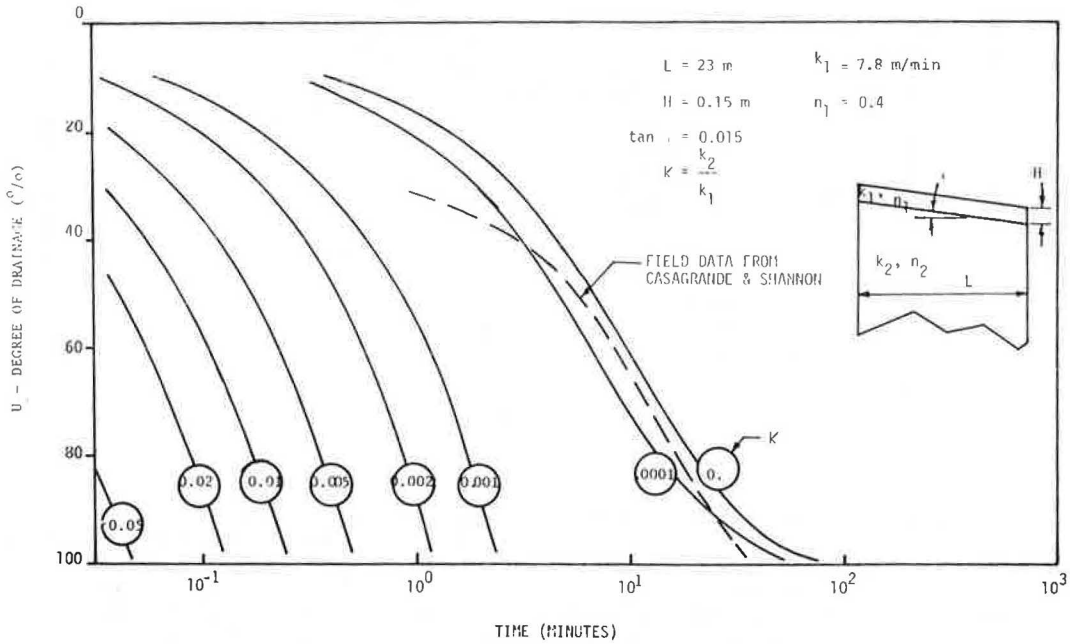

Figure 12. Results of Casagrande-Shannon model with permeable subgrades: test section 2.

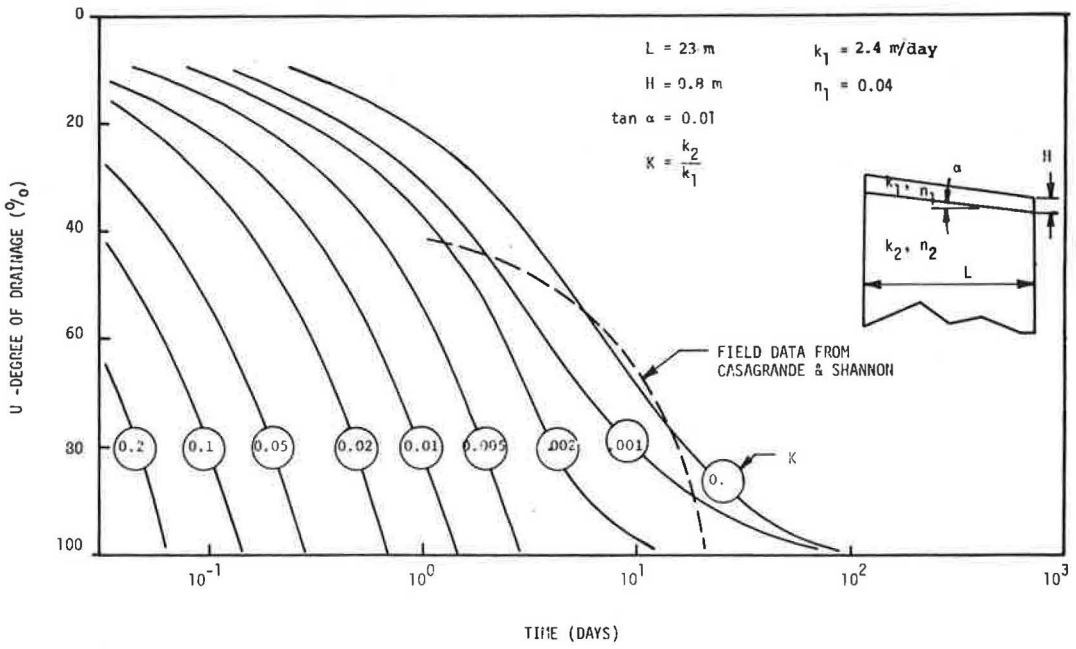

Figure 13. Results of Casagrande-Shannon model with permeable subgrades: test section 3.

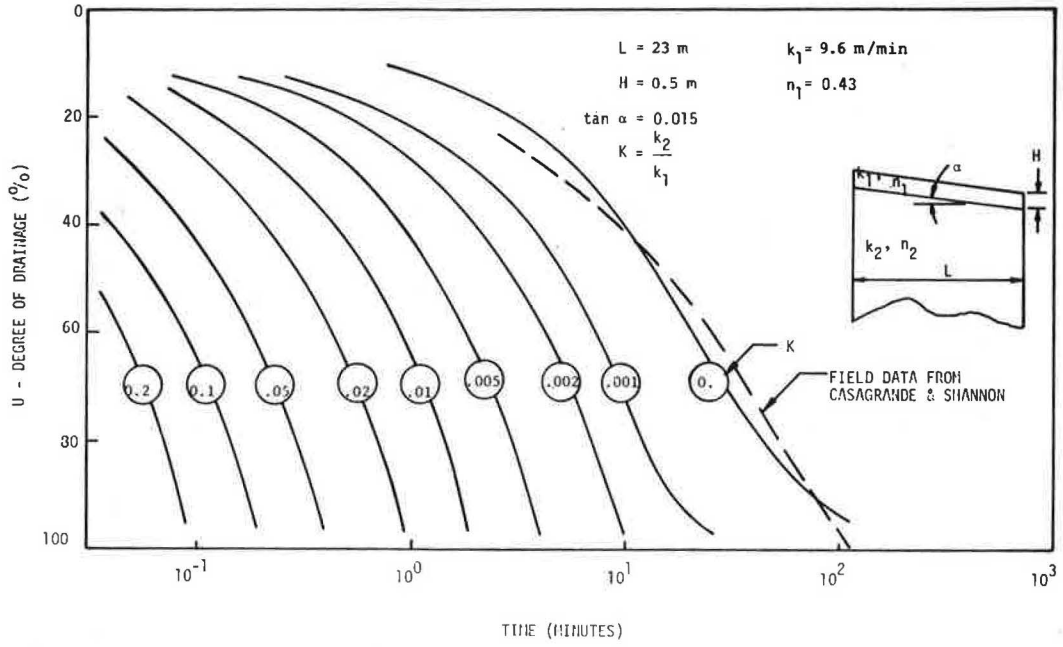

Figure 17 shows the parabolic model with a permeable subgrade (K = 0.0001) to be in closer agreement with the field data than is the Casagrande-Shannon model.

As a result of these studies and others not reported here, the parabolic phreatic surface model with permeable subgrades is recommended for future drainage analyses.

APPLICATION TO PAVEMENT DRAINAGE DESIGN

As an illustration of the importance of subgrade drainage, consider a base course 0.8-m (2.5-ft) thick and 46-m (150-ft) wide with 1 percent cross slope. The base course has its smallest particles in the medium sand range and has a coefficient of permeability, k_1 = 2.4 m/day (7.8 ft/day), and a porosity, n_1 = 0.04. The drainage time for 60 percent drainage of a number of subgrade materials can be determined as follows (see Figure 18 for various values of subgrade permeability):

For subgrade material that is a plastic clay,

k_2 = 0.0024 m/day (0.0078 ft/day),
$K = k_2/k_1$,
= 0.001, and
t = 5 days.

Figure 14. Results of Casagrande-Shannon model with permeable subgrades: test section 4.

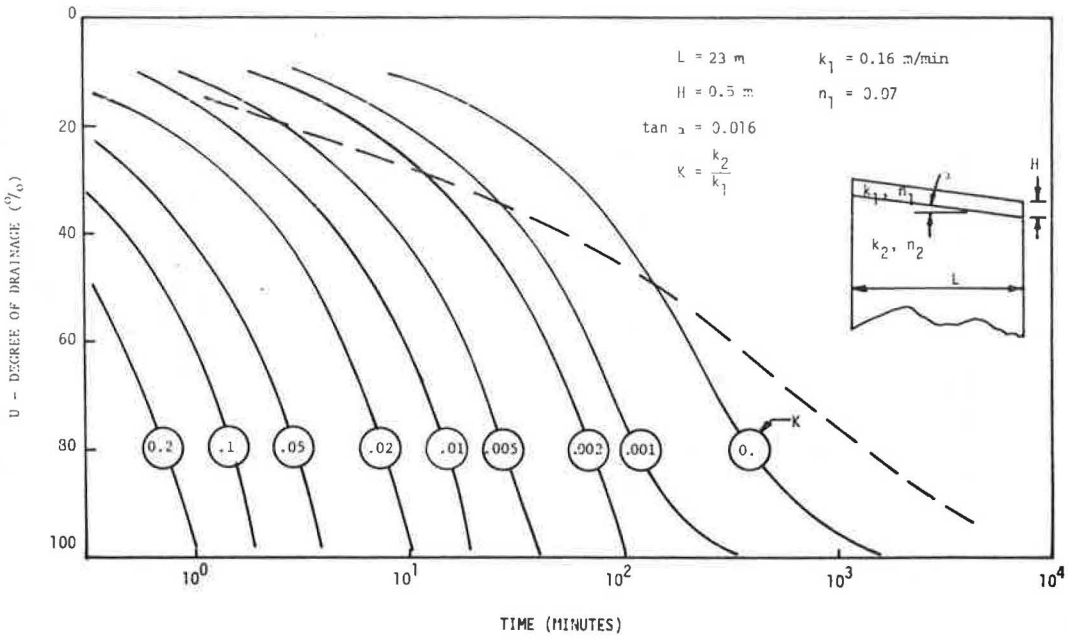

Figure 15. Subgrade drainage model with parabolic phreatic surfaces.

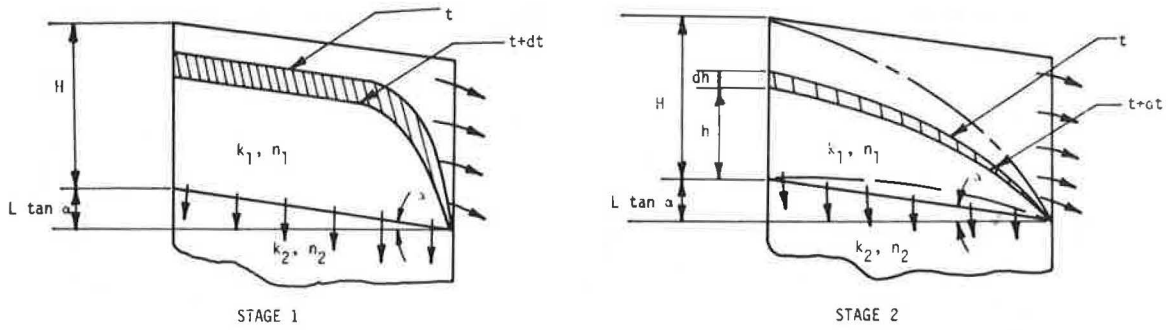

Figure 16. Results of TTI model with permeable subgrades: case 1.

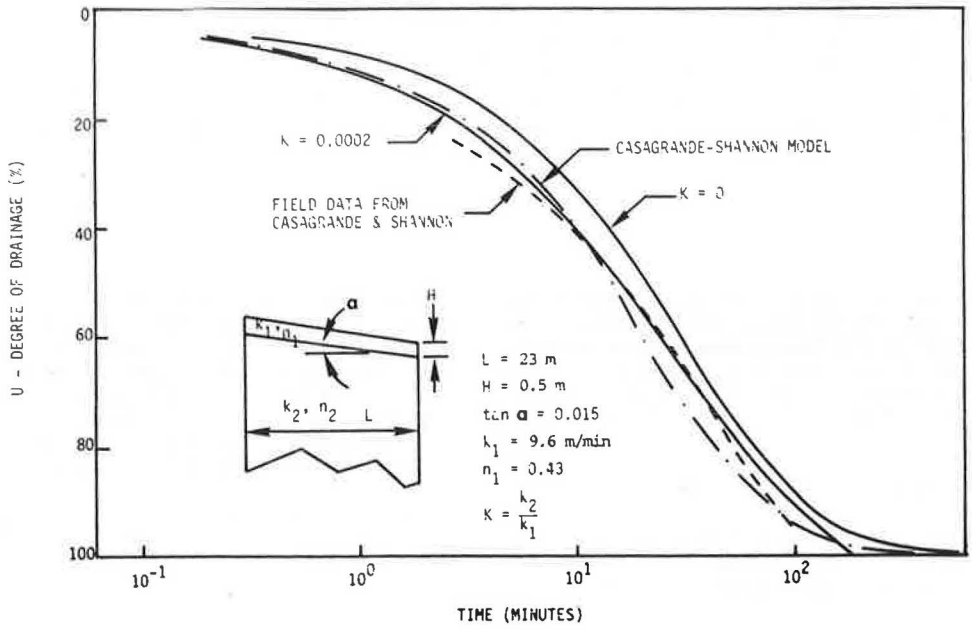

Figure 17. Results of TTI model with permeable subgrades: case 2.

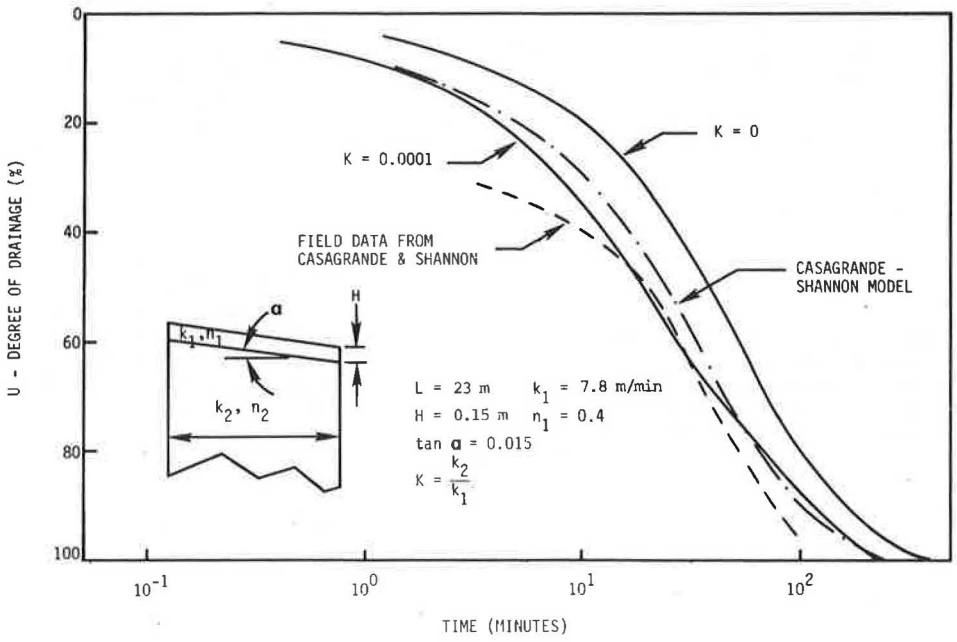

Figure 18. Drainage curves for TTI model with permeable subgrades.

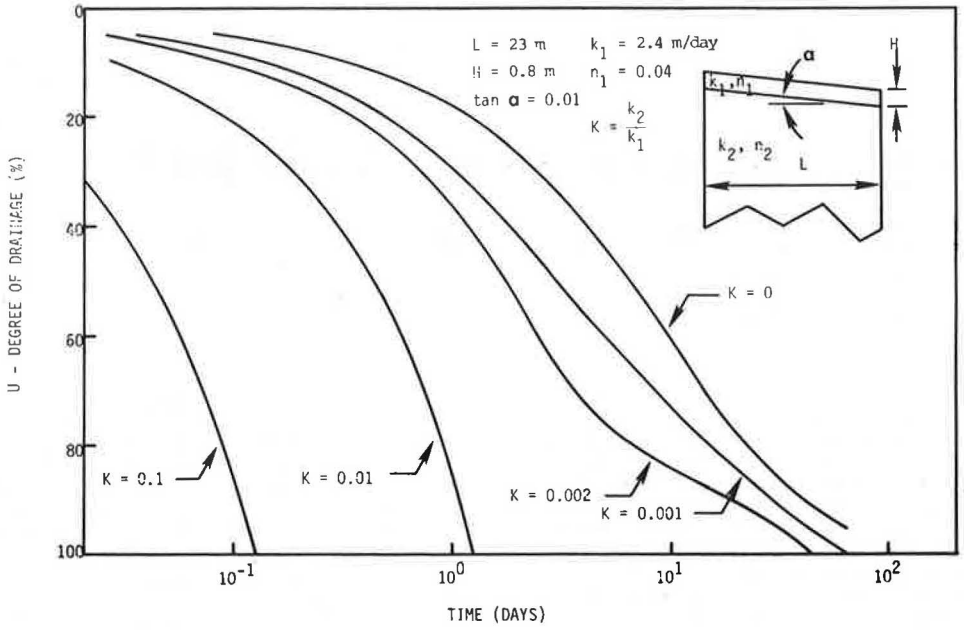

For subgrade material that is a glacial till,

k_2 = 0.0048 m/day (0.0156 ft/day),
K = 0.002, and
t = 2.5 days.

For subgrade material that is a silty sand,

k_2 = 0.24 m/day (0.78 ft/day),
K = 0.1, and
t = 84 min.

These calculations show that subgrade permeability will significantly influence pavement drainage and subdrainage design. A specific example, which uses the data shown in Figure 18, is used here to illustrate the usefulness of the new TTI base-subgrade drainage model. More general pavement drainage design calculations can be performed by using the computer program TTIDRAIN, which was used to make the calculations reported in this paper.

CONCLUSIONS

Saturated base courses beneath highway and airport pavements are reduced in modulus and bearing capacity, and pumping may develop at pavement joints. Base-course drainage is often required to avoid this major cause of pavement deterioration. A number of theoretical drainage models have been discussed

including the original one by Casagrande and Shannon (1), which assumed a straight-line phreatic surface and an impermeable subgrade. The influence of subgrade drainage on drainage time and the influence of the use of the more theoretically correct parabolic phreatic surface, especially in deep base courses or on flat slopes, were found to be substantial. New models were developed to include these features, and the calculated results are generally in good agreement with field data from full-scale pavements. The new models are recommended for future subdrainage calculations.

ACKNOWLEDGMENT

The results reported in this paper were obtained as part of an ongoing research program on Environmental Effects on Zero Maintenance Pavements funded by FHWA. Thanks are extended to B.D. Garrett for his contribution throughout the development of this project.

REFERENCES

1. A. Casagrande and W.L. Shannon. Base Course Drainage for Airport Pavements. Proc., ASCE, Vol. 77, June 1951.
2. E.S. Barber and C.L. Sawyer. Highway Subdrainage. Public Roads, Vol. 26, No. 12, 1952.
3. H.R. Cedergren. Drainage of Highway and Airfield Pavements. Wiley, New York, 1974.
4. L.K. Moulton. Highway Subdrainage Design. FHWA, Rept. FHWA-TS-80-224, Aug. 1980.
5. M.J. Markow. Simulating Pavement Performance Under Various Moisture Conditions. TRB, Transportation Research Record 849, 1982, pp. 24-29.
6. K. Wallace and F. Leonardi. Theoretical Analyses of Pavement Edge Infiltration and Drainage. Dept. of Civil Engineering, James Cook Univ. of North Queensland, Townsville, Queensland, Australia, Res. Rept. 6, 1975.
7. P. Ya. Polubarinova-Kochina. Theory of Ground Water Movement (J.M.R. De Wiest, translator). Princeton Univ. Press, Princeton, N.J., 1962.

Publication of this paper sponsored by Committee on Environmental Factors Except Frost.

Investigation of Moisture-Induced Variation in Subgrade Modulus by Cross-Correlation Method

S.S. BANDYOPADHYAY AND J.A. FRANTZEN

The change in moisture content of subgrade soils and its resultant effects on structural pavement performance are of interest to many highway engineers. One of the primary sources of moisture in the subgrade is water from precipitation. The purpose of this research was to examine the feasibility of statistically relating the variation in subgrade modulus with the corresponding time history of precipitation. Two locations on KS-4 in northeast Kansas were monitored from March through November. Dynamic pavement surface deflections were obtained each week by Dynaflect, and time histories of subgrade moduli were constructed from normalized Dynaflect deflection parameters. A corresponding time history of precipitation at the locations was obtained from the local U.S. Weather Bureau station. A cross-correlation study by computer of the two time series revealed a statistically significant correlation between precipitation history and variation in subgrade modulus. The time required for the subgrade to reach its weakest state after a rainfall was found to be rather long—up to 3 weeks might be required. The interrelationship of other factors, such as runoff characteristics and temperature, that might influence this time delay, was not considered in this study.

The effect of moisture on subgrade strength is an important factor in the evaluation of highway pavement performance and for highway design problems. Variations in subgrade moisture, with corresponding changes in volume and strength characteristics of subgrade soils, may cause severe damage to pavement. The reduction in subgrade strength caused by an influx of moisture with the consequent increase in pavement deflection and decrease in bearing capacity is well documented in the literature (1-6). Attempts to develop mathematical models to predict the variation in pavement deflections with changes in subgrade moisture have also been made (7,8).

Soil moisture migrates as a result of any force that disturbs equilibrium of the soil-water system. Several different viewpoints have been expressed in the literature concerning forces that cause moisture to migrate. A few of the most widely discussed hypotheses are hydrostatic pressure, capillary pressure, disjoining pressure of aqueous films (often referred to as osmotic pressure), chemical potentials, and temperature gradients. Moisture may migrate through soil in the liquid phase, vapor phase, or in a combination of the two, depending on the forces that cause pore-water movement.

Sources of free water must be present for moisture migration to occur in subgrades. The primary source of moisture in the subgrade is undoubtedly precipitation, which can reach the subgrade in several ways--seepage of the water into the subgrade from higher ground, percolation of the water through the pavement surface, and migration of the water from shoulder slopes or verges.

Most of the published material is concerned with

loss of the load-carrying capacity of highways during the spring thaw period. The direct effect of rainfall on subgrade strength has received only minor consideration. Although variations in subgrade moisture are affected considerably by precipitation (4,5,9,10), no direct correlation has been developed because of the complexity of the problem. The primary objective of this study was to examine the feasibility of relating the variation in subgrade modulus statistically with the corresponding time history of precipitation. A secondary objective was to demonstrate the use of the cross-correlation method in geotechnical investigations.

PROJECT HISTORY

Two locations, about 1 mile apart, were selected on KS-4 in Jefferson County, northeast Kansas. The asphalt-concrete pavement was built in 1978 on a glacial till subgrade of the Kansas stage; the highway traverses a region of rolling hills. The A-horizon soils have a plasticity index of about 18 and a standard Proctor density of 100 lb/ft³. The plasticity index of B-horizon soils ranges from 17 to 30 and the standard Proctor density from 96 to 103 lb/ft³. The ranges of plasticity index and standard Proctor density for C-horizon soils are 18 to 39 and 98 to 111 lb/ft³, respectively. Some of the B-horizon and C-horizon soils are moderately expansive in nature. The top 6 in. of the subgrade was lime-treated with 6 percent (by weight) lime. The asphalt-concrete pavement structure consists of a 4-in. surface course and a 7.5-in. base course at location 1, and a 2-in. surface course and a 7.5-in. base course at location 2. The pavement was virtually free of cracks during the period of observation.

EQUIPMENT AND DATA COLLECTION

Pavement surface deflections were monitored weekly by Dynaflect at both locations for 9 months, March through November. The Dynaflect is an electromechanical system for measuring the dynamic deflection of a surface or structure caused by an oscillatory load. Measurements are independent of a fixed surface reference.

The Dynaflect system consists of a dynamic force generator mounted on a small two-wheel trailer, a control unit, a sensor assembly, and a sensor calibration unit. The cyclic force generator uses a pair of unbalanced fly wheels that rotate in opposite directions at a speed of 480 rpm, or 8 cycles per second. The vertical component of the acceleration of the unbalanced mass produces the cyclic force that is applied to the ground through a pair of rigid wheels. The amount of fly wheel unbalance is chosen precisely to produce a 1,000-lb peak-to-peak variation of force during each rotation of the fly wheels at the proper speed. Considering the dead weight of the trailer, the resulting sinusoidal load ranges between 2,500 and 1,500 lb at 8 cycles per second.

Deflections are measured while the trailer is halted for a brief time at the desired location. The displacement measurements are performed by using motion sensors located midway between the two loading wheels and spaced in the longitudinal direction at 1.0-ft intervals. There are five such sensors with an extra one that can be used anywhere on the pavement, if desired, within 20 ft of the loading wheels. The sensor array and the deflection basin parameters associated with the Dynaflect measurements are shown in Figure 1. The five parameters associated with each Dynaflect measurement are described as follows (11-16):

1. Dynaflect maximum deflection (DMD), or the first sensor deflection, is a measure of the pavement structural characteristics and support conditions;
2. Surface curvature index (SCI), or the numerical difference of the first and second sensor deflections, is predominantly an indicator of the structural condition of the surface layer;
3. Base curvature index (BCI), or the numerical difference of the fourth and fifth sensor deflections, measures the base support conditions;
4. Spreadability (SP), or the average deflection as a percentage of maximum deflection, measures the load-carrying capacity and stiffness ratio of the pavement structure; and
5. Fifth sensor deflection (W_5) is an indirect measure of subgrade modulus.

The five parameters, considered either individually or jointly, can provide an estimate of the structural characteristics of the measured pavement structure (11-16). Because deflection parameters are functions of pavement temperature, adjustment factors are needed to normalize measured deflections with respect to a base temperature (11). Temperature adjustment factors for Dynaflect parameters have recently been developed for Kansas road conditions (12) and are shown in Figures 2-4. No adjustment factors are found necessary for BCI and W_5 (12). A summary of deflection parameters obtained at the site and normalized with respect to temperature is given in Table 1. The adequacy of the sample size of Dynaflect deflection measurements was checked in the field by using the nomograph shown in Figure 5. This nomograph is based on appropriate statistical procedures described elsewhere (17-19). The pavement and the subgrade moduli may be estimated from values of DMD and SP (20). By using the normalized values of DMD and SP, weekly subgrade modulus values at locations 1 and 2 were determined and are shown in Figure 6. Daily precipitation data at the location were acquired from a U.S. Weather Bureau station located within 2 miles of the site. The precipita-

Figure 1. Dynaflect sensor array and deflection parameters.

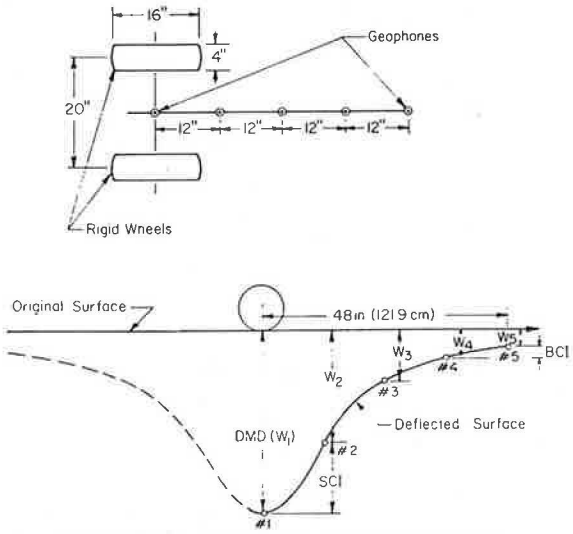

W_{max} = Dynaflect Maximum Deflection (numerical value of sensor #1)
SCI = Surface Curvature Index (numerical difference of sensor #1 and #2)
BCI = Base Curvature Index (numerical difference of sensor #4 and #5)

$$SP\% = \frac{W_1 + W_2 + W_3 + W_4 + W_5}{5\,W_1} \times 100$$

W_5 = Numerical value of sensor #5

Figure 2. Temperature adjustment factors for DMD (12).

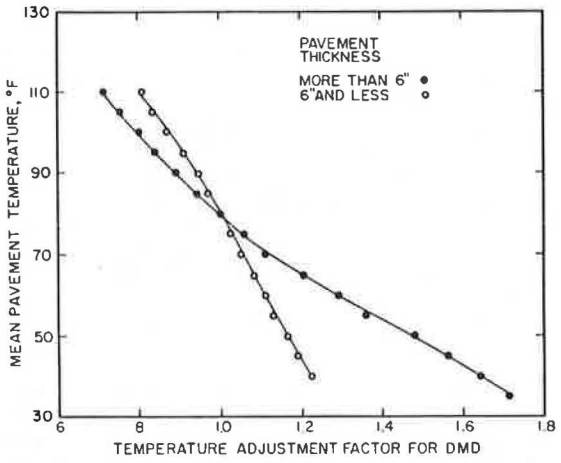

Figure 3. Temperature adjustment factors for SCI (12).

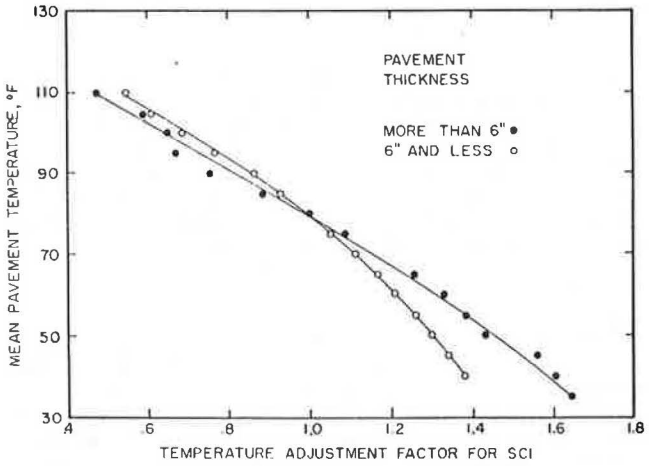

Table 1. Summary of normalized deflection parameters.

	Dynaflect Deflection Parameters									
	DMD(in. x 10^{-3})		SCI(in. x 10^{-3})		BCI(in. x 10^{-3})		SP(%)		W_5(in. x 10^{-3})	
	Location		Location		Location		Location		Location	
Date	#1	#2	#1	#2	#1	#2	#1	#2	#1	#2
March 6	0.57	0.70	0.05	0.07	0.06	0.07	69	69	0.18	0.21
March 14	0.64	0.69	0.07	0.07	0.06	0.07	66	67	0.19	0.21
March 20	0.64	0.72	0.08	0.08	0.06	0.07	66	66	0.19	0.21
March 27	0.58	0.58	0.06	0.05	0.06	0.06	69	69	0.20	0.21
April 3	0.55	0.62	0.06	0.06	0.06	0.06	68	69	0.18	0.20
April 10	0.50	0.56	0.08	0.07	0.07	0.08	69	70	0.19	0.21
April 17	0.62	0.64	0.06	0.06	0.06	0.07	66	67	0.19	0.21
April 24	0.62	0.59	0.07	0.06	0.08	0.09	66	70	0.20	0.22
May 8	0.62	0.66	0.10	0.10	0.07	0.09	66	67	0.20	0.21
May 15	0.62	0.63	0.09	0.07	0.09	0.09	66	68	0.20	0.21
May 23	0.56	0.55	0.09	0.07	0.07	0.08	67	69	0.19	0.20
May 30	0.68	0.62	0.10	0.09	0.08	0.07	65	67	0.22	0.20
June 5	0.63	0.58	0.08	0.07	0.08	0.08	64	71	0.21	0.22
July 3	0.59	0.59	0.08	0.08	0.08	0.08	66	67	0.19	0.20
July 18	0.69	0.63	0.13	0.10	0.10	0.10	64	70	0.19	0.23
July 25	0.70	0.68	0.10	0.10	0.12	0.11	66	65	0.23	0.22
Aug. 15	0.61	0.57	0.09	0.08	0.08	0.08	68	68	0.21	0.21
Aug. 28	0.62	0.60	0.08	0.08	0.09	0.11	69	70	0.23	0.22
Sept. 11	0.55	0.55	0.07	0.07	0.07	0.07	68	69	0.21	0.22
Sept. 19	0.59	0.57	0.09	0.08	0.06	0.07	66	68	0.21	0.24
Sept. 26	0.57	0.57	0.07	0.07	0.07	0.07	68	68	0.20	0.20
Oct. 3	0.61	0.60	0.04	0.04	0.06	0.06	67	68	0.19	0.20
Oct. 16	0.65	0.58	0.11	0.08	0.08	0.08	65	67	0.20	0.21
Oct. 31	0.51	0.55	0.03	0.05	0.05	0.06	68	67	0.18	0.18
Nov. 13	0.61	0.70	0.05	0.07	0.01	0.04	69	66	0.19	0.19
Nov. 26	0.55	0.60	0.04	0.06	0.05	0.06	67	66	0.17	0.18

tion data corresponding to subgrade modulus values are also plotted in Figure 6.

CROSS-CORRELATION

Comparison of two time series--subgrade modulus and precipitation--was made by examination of the cross-correlation coefficient. The correlation coefficient summarizes in a single quantity the extent to which pairs of the data subsets vary linearly with each other. Because the correlation coefficient ranges from -1 to +1 and indicates an increasingly large linear correlation as it approaches either end of its range, examination of the correlation coefficients provides a simple way to compare data of different groups.

One way of comparing two similar parts of a curve is to break the two segments apart and fit one to the other. The goodness-of-fit, measured in some manner, would be an index of their similarity. Autocorrelation, in effect, does this except the entire sequence is compared to itself at all possible positions. The autocorrelation of a time series (Y_i) at lag(L) is given by

$$r_L = \mathrm{Cov}[Y_i, Y_{i+L}]/S_y^2 \quad (1)$$

where

Figure 4. Temperature adjustment factors for SP (12).

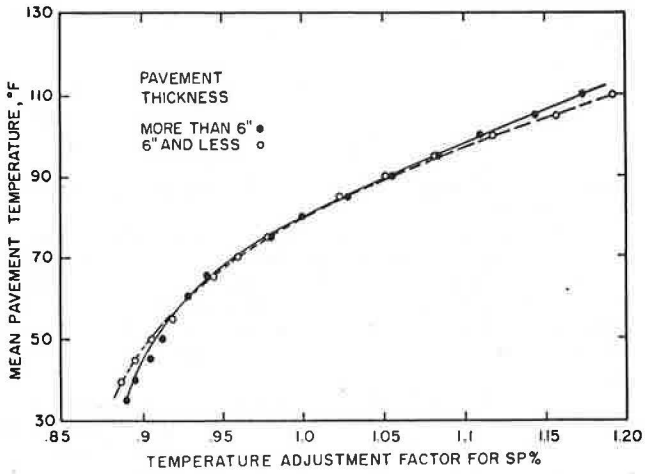

Figure 6. Time histories of subgrade modulus and precipitation at locations 1 and 2.

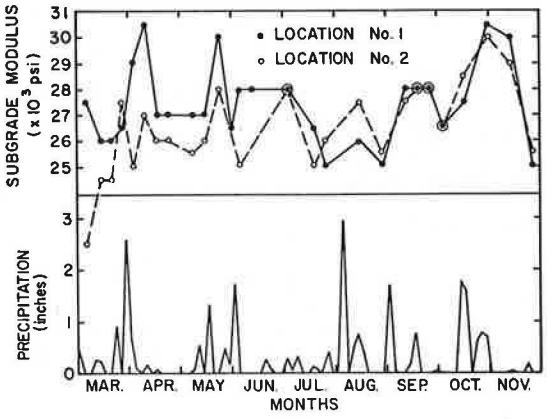

Figure 5. Nomograph to determine sample size at 95 percent confidence level for Dynaflect deflections (19).

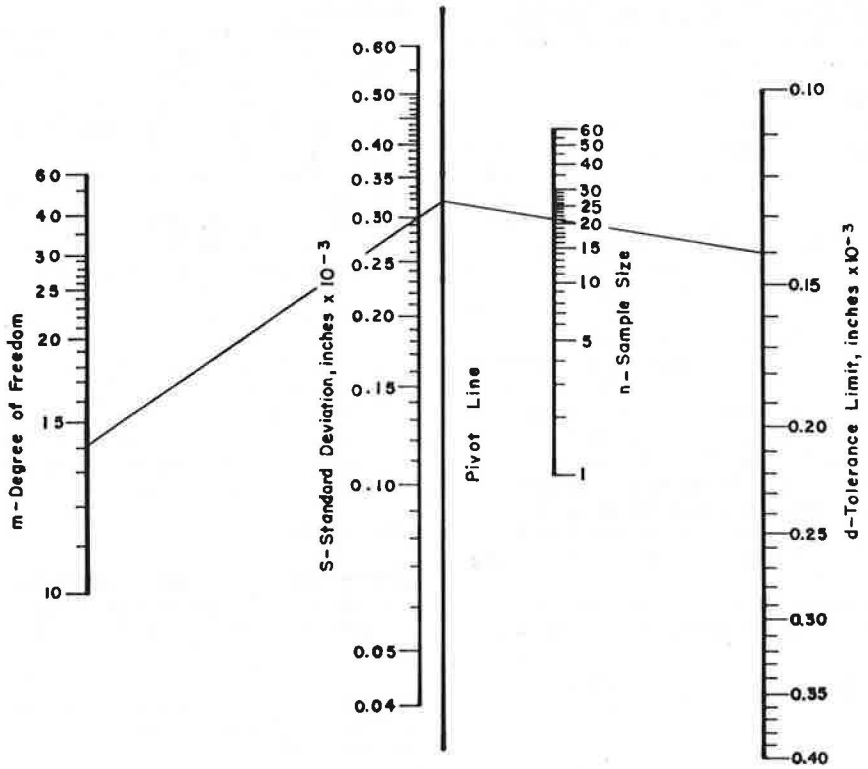

Cov = covariance,
S_y = standard deviation, and
L = amount of offset between the two series being compared.

To perform cross-correlation, however, the technique for moving the sequences past one another must be modified. When two different series are being compared, cross-correlations must be made. Because one sequence is being moved past the other rather than being lagged behind from a position of initial equivalence, the successive comparisons are referred to as match positions rather than lags. A plot of match positions versus cross-correlation is called a cross-correlogram. A typical example is shown in Figure 7, which explains the construction of a correlogram produced by two dissimilar sequences.

The cross-correlation for comparison of two time series (Y_1 and Y_2) is defined as (21)

$$r_m = (n\Sigma Y_1 Y_2 - \Sigma Y_1 \Sigma Y_2)/\left\{[n\Sigma Y_1^2 - (\Sigma Y_1)^2]\,[n\Sigma Y_2^2 - (\Sigma Y_2)^2]\right\}^{1/2} \quad (2)$$

or

$$r_m = \mathrm{Cov}\,[Y_1, Y_2]/S_1 S_2 \quad (3)$$

where

r_m = cross-correlation coefficient,
n = number of overlapped positions between the two series,

$\text{Cov}\ [Y_1, Y_2]$ = covariance of the overlapped portions of the two sequences, and

S_1, S_2 = standard deviations of the overlapped segments of sequences 1 and 2.

The summations are understood to extend only over the segments of the two sequences that are overlapped at the match position.

The significance of the cross-correlation coefficient can be assessed by the approximate test (21),

$$t = r_m\ [(n-2)/(1-r_m^2)]^{1/2} \quad (4)$$

which has n-2 degrees of freedom. This test has been derived from a test for the significance of the correlation between two samples drawn from normal populations. The null hypothesis is that the correlation is zero.

DISCUSSION OF RESULTS

A computer program CROSCR (21) is used to compute the cross-correlation between the two time series. The program slides the first chain past the second by an incrementing DO loop in which the correlation coefficient is calculated. Successive values of r_m are printed with corresponding values of the t-statistic calculated by Equation 4.

Figure 8 shows the cross-correlograms for locations 1 and 2 and the corresponding t-statistic. Each series was represented by 90 data points with match position 1 defined by the overlap of the first three points of the precipitation series and the last three points of the modulus series. Because the effect of precipitation is to reduce the subgrade modulus value, negative values of the cross-correlation coefficient need to be studied for a specified matching position. Match position 88 defines the two time series with zero lag and match positions in its vicinity, but positions greater than position 88 should be of interest for comparison study. It is evident from Figure 8 that the highest correlation is obtained at match position 92 for location 1 and match position 95 for location 2. Because there are 3 days between two successive match positions, the inference could be made that it took 12 to 21 days for the subgrade at the locations investigated to reach its critical state after the corresponding precipitation.

The time lag between the precipitation and the critical state of the subgrade seems to be large and must be interpreted cautiously within the limitations of the investigation. The frequency of the deflection measurements is not less than 7 days, and the precipitation scale represents the amount of precipitation for 3 consecutive days. Furthermore, the subgrade modulus values are arrived at indirectly. Even with these limitations, the cyclic nature of the cross-correlogram, which is also true for other match positions not shown in Figure 8, certainly indicates the interdependency of the two time series.

An estimate of the significance of the correlation can be made from the plot of t-statistic for each match position shown in the top part of Figure 8. To determine the probability that the correlation coefficients represent causative rather than fortuitous relationships or linkages between pairs of parameters, two confidence levels were selected. At the 95 percent confidence level, the null hypothesis (no correlation) can be rejected for match positions 90 through 94, and at the 99 percent confidence level, the same conclusion can be drawn for match positions 92 and 93 for location 1. High confidence levels should be considered because there is some probability that even pairs of numbers selected completely at random will show some degree of correlation.

The extent of the variation in subgrade modulus due to precipitation will depend, in part, on the geotechnical properties of the subgrade soils and the topography of the location. The general topography around the test locations is rolling. Both test sites are located on a fill section 5 to 6 ft high. The subgrade soils are predominantly glacial and alluvial. The maximum, minimum, and average values of the subgrade modulus during the 9-month period were found to be 30,500, 25,000, and 27,375 psi at location 1 and 30,000, 22,000, and 26,604 psi at location 2, respectively. In other words, the variation in the average subgrade modulus at location 1 ranges from +11.4 percent to -8.6 percent, whereas that at location 2 ranges from +12.8 percent to -17.3 percent. Although no extrapolation or generalizations can be made from these values, the magnitude of variation probably would have been greater for the same pavement structure without the lime-treated subgrade.

CONCLUSIONS

Within the scope and limitations of this study the following conclusions can be advanced. The subgrade modulus is directly affected by precipitation. The

Figure 7. Example of correlogram produced by cross-correlation of two dissimilar sequences (correlogram is asymmetric unless both sequences are identical).

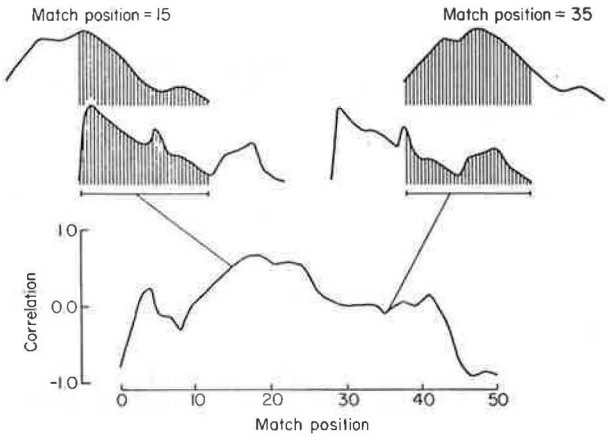

Figure 8. Correlogram and t-statistics produced by subgrade modulus and precipitation data sequences at two locations.

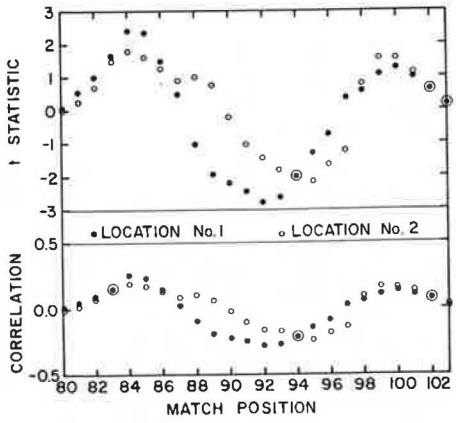

time required for the subgrade to reach its weakest state after a rainfall is quite long; depending on local factors, it might be as long as 3 weeks. At the 95 and 99 percent confidence levels a correlation is found to exist between the two time series--precipitation history and corresponding variation in subgrade modulus. The variation in the average modulus of the lime-treated subgrade ranges from +11.4 to -8.6 percent at location 1 and from +12.8 to -17.3 percent at location 2.

ACKNOWLEDGMENT

The senior writer acknowledges support provided by the professional development program of NFS Services during the preparation of this paper.

REFERENCES

1. F.H. Scivner, R. Peohl, W.M. Moore, and M.B. Phillips. Detecting Seasonal Changes in Load-Carrying Capabilities of Flexible Pavements. NCHRP, Rept. 76, 1969.
2. B.B. Broms. Effect of Degree of Saturation on Bearing Capacity of Flexible Pavements. HRB, Highway Research Record 71, 1965, pp. 1-14.
3. G.L. Hoffman, G. Cumberledge and A.C. Bhajandas. Frost Action Effects on Pavements--Executive Summary. Pennsylvania Department of Transportation, Rept. FHWA-PA-RD-68-30, Dec. 1979.
4. N.K. Vaswani. Case Studies of Variations in Subgrade Moisture and Temperature Under Road Pavements in Virginia. TRB, Transportation Research Record 532, 1975, pp. 30-42.
5. B.D. Marks and T.A. Haliburton. Subgrade Moisture Variations Studied with Nuclear Gages. HRB, Highway Research Record 276, 1969, pp. 14-24.
6. J.N. Guinnee. Field Studies on Subgrade Moisture Conditions. HRB, Special Rept. 40, 1958, pp. 253-267.
7. R.J. Krizek. Seasonal Variation in Flexible Pavement Deflections. Journal of the Highway Division, ASCE, Vol. 94, No. HW2, Nov. 1968, pp. 219-228.
8. G. Cumberledge, G.L. Hoffman, A.C. Bhajandas, and R.J. Cominsky. Moisture Variation in Highway Subgrades and the Associated Change in Surface Deflections. TRB, Transportation Research Record 497, 1974, pp. 40-49.
9. K. Russam. Subgrade Moisture Studies by the British Road Research Laboratory. HRB, Highway Research Record 301, 1970, pp. 5-17.
10. G. Way. Environmental Factor Determination from In-Place Temperature and Moisture Measurements Under Arizona Pavements. Arizona Department of Transportation, Rept. FHWA-AZ-80/157, Aug. 1980.
11. S.S. Bandyopadhyay. Developing a Functional Subsystem of Overlay Design Using Dynamic Deflections. Journal of Civil Engineering Design, Marcel Dekker, Vol. 2, No. 4, 1980, pp. 443-457.
12. S.S. Bandyopadhyay. Flexible Pavement Evaluation and Overlay Design. Transportation Engineering Journal, ASCE, Vol. 108, No. TE6, Nov. 1982, pp. 523-539.
13. S.S. Bandyopadhyay. Structural Performance Evaluation of Recycled Pavements by Using Dynamic Deflections Measurements. TRB, Transportation Research Record 888, 1982, pp. 38-43.
14. S.S. Bandyopadhyay. Dynamic Deflection of Pavement: Measurements, Interpretations and Applications. Proc., International Symposium on Bearing Capacity of Roads and Airfields, Trondheim, Norway, June 1982, pp. 858-869.
15. S.S. Bandyopadhyay. Design and Structural Condition Evaluation of a Cold Recycled Pavement. In Properties of Flexible Pavement Materials, ASTM, Special Tech. Publication 807, 1983.
16. S.S. Bandyopadhyay. Pavement Distress Identification and Condition Evaluation. Journal of Civil Engineers for Practicing and Design Engineers, Pergamon Press, Vol. 2, No. 6, 1983.
17. S.S. Bandyopadhyay. Sample Size of Pavement Deflections. Journal of Civil Engineering Design, Marcel Dekker, Vol. 2, No. 4, 1980, pp. 339-346.
18. S.S. Bandyopadhyay. Determining Sample Size of Pavement Deflections by Nomograph. Civil Engineering, ASCE, Vol. 53, No. 3, March 1983, pp. 57-59.
19. S.S. Bandyopadhyay. Sample Size of Pavement Deflections by Nomograph. Transportation Engineering Journal, ASCE, Vol. 109, No. TE4, July 1983.
20. K. Majidzadeh. Dynamic Deflection Study for Pavement Condition Investigation. Ohio Department of Transportation, Final Rept., June 1974.
21. J.C. Davis. Statistics and Data Analysis in Geology. Wiley, New York, 1973.

Publication of this paper sponsored by Committee on Environmental Factors Except Frost.

Matrix Suction Instrumentation of a Vertical Moisture Barrier

MIGUEL PICORNELL, ROBERT L. LYTTON, AND MALCOLM STEINBERG

The rehabilitation of a section of Interstate 37 in San Antonio, Texas, was undertaken to correct a chronic problem of expansive clay roughness. A vertical moisture barrier was placed down to a depth of 8 ft (2.4 m) along the outside shoulders of the northbound and southbound lanes. Several concurrent measurements, including the measurement of matrix suction at both sides of the membrane at several depths, were made in the laboratory and in the field to evaluate the effectiveness of the moisture barrier. The calibration of the thermal moisture sensors that are used to measure suction, the difficulties encountered in the calibration process and how they were overcome, and the installation of the sensors in boreholes on each side of the moisture barrier are described in this paper. The devices are sensitive and accurate in measuring suctions above -1 bar but lose sensitivity below that level of suction. The sensors are expected to provide stable readings for several years. The site and soil conditions, the placement and cost of installing the vertical moisture barrier, and subsequent indications of moisture changes inside and outside of the barrier are also described.

The rehabilitation of a section of I-37 in San Antonio was undertaken to correct a chronic problem of expansive clay roughness. A vertical moisture barrier was placed down to a depth of 8 ft (2.4 m) along the outside shoulders of the northbound and southbound lanes. Several types of measurements have since been made to evaluate the effectiveness of the moisture barrier. These measurements include (a) periodic measurements of the matrix suction with devices that are the subject of this paper, (b) pavement surface profile measurements with the GM profilometer, and (c) a variety of laboratory tests on the soil from the site to determine its engineering, chemical, and mineralogical characteristics. The site location and existing subsurface conditions, the installation of the moisture barrier, and the calibration and installation of the moisture sensors are outlined in this paper. Some of the preliminary results of the study are presented and interpreted.

SITE LOCATION

Figure 1 shows a location map of the project site within the city of San Antonio on I-37. Where the deep, vertical, fabric moisture barrier was placed I-37 is an eight-lane divided highway (see Figure 2). The main lanes were separated by a sodded median, 28 to 36 ft (8.5 to 11.0 m) wide that had a concrete median ditch 3 ft (0.9 m) wide and a steel medium barrier guardrail. Each of the travel lanes was 12 ft (3.66 m) wide, with a 10-ft (3.05-m) outside shoulder and a 6-ft (1.8-m) inside shoulder. The main lanes were constructed on 6 in. (15 cm) of lime-treated subgrade, 6 in. (15 cm) of lime-stabilized base, and 8 in. (20 cm) of concrete pavement.

The rehabilitation contract included a rubberized asphalt seal coat, an asphaltic concrete level-up, and a finish course. Reconstruction of the median provided positive drainage from a built-up section with a concrete Jersey-type median barrier on base, which was sealed with asphalt (see Figure 3). A moisture barrier was placed 8 ft (2.4 m) deep along the outside shoulders of the northbound and southbound lanes. A perforated underdrain pipe 6 in. (15 cm) in diameter was placed in some areas outside the fabric. The fabric's trench was backfilled with gravel and the top 3 ft (0.9 m) were cement stabilized. Project contract quantities called for placement of 23,750 yd² (19 860 m²) of the fabric. The work extended from South Hackberry Street on I-37 to south of Pecan Valley Drive, a distance of more than 2 miles (3.2 km).

The depth of the barrier was selected on the basis of the monitoring records (1,2) of heave and moisture changes in a nearby, similar site. The heave records indicated that most of the heave took place above the 8-ft depth. Below 8 ft (2.4 m), the moisture content versus depth curves remained approximately parallel during the whole monitoring period, which indicates that moisture content below this depth is not affected by seasonal changes.

SUBSURFACE CONDITIONS

Subsurface conditions were investigated by drilling eight borings with a hand auger to a depth of 3 ft (0.9 m). For the field installation of the matrix

Figure 1. Location map.

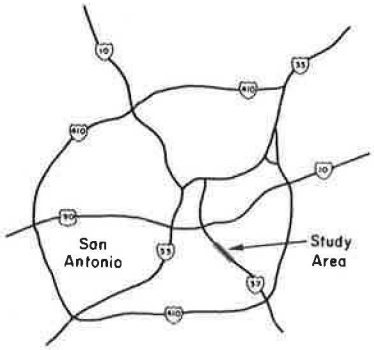

Figure 2. Cross section of existing pavement.

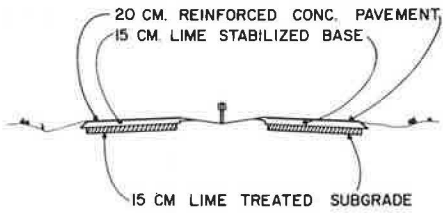

Figure 3. Cross section of rehabilitated pavement showing vertical moisture barriers.

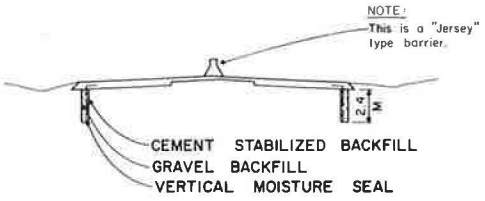

suction sensors four mechanical borings were also drilled to a depth of 9 ft (2.7 m). The approximate locations of these borings are shown in Figure 4.

Figure 4. Site plan of sensor installations.

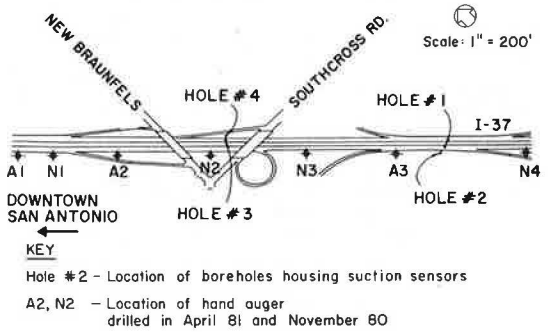

The hand-auger borings were drilled at two different times, the first half in November 1980 and the second half in April 1981. The deeper borings were drilled in October 1981.

Throughout the depth investigated, the subsoil consisted of highly weathered claystone. The soil is a highly plastic silty clay (CH), light gray mottled yellow and brown, with some sand and fine gravel. The grain-size distribution was investigated by sieving through No. 200 sieve, complemented by a hydrometer determination of the colloid content. The sand fraction represented less than 5 percent of the majority of the samples, the silt fraction amounted to from 35 to 45 percent, and the clay size particles made up from 50 to 65 percent of the total dry weight.

The liquid limit oscillated between 70 and 85 percent, and the plasticity index ranged from 40 to 50 percent. The general trend was for plasticity to increase with depth within the upper 3 ft (0.9 m). The activity (3) of these soils averaged about 0.85, which corresponds to that of a normally active clay.

The moisture contents of the soil samples obtained in the first hand-auger borings showed a marked increase with depth. The average moisture content of the soils was only 83 percent of their plastic limits in the first foot (0.3 m), but it was 91 percent in the second foot (0.6 m). The moisture content in the third foot (0.9 m) was higher than that of the plastic limit. Therefore, moisture contents that were higher than the plastic limit could be expected within the 8 ft (2.4 m) of membrane penetration. Furthermore, before the sampling in the summer of 1980 the weather was extremely hot and there was a long period of drought; as a result the samples taken in October 1981 had low moisture contents, probably the lowest to be encountered during the entire monitoring period.

To determine the mineralogical composition the soil was fractionated into sand, silt, coarse clay, and fine clay. Both clay fractions were dialyzed and freeze-dried. The minerals in each clay fraction were identified in subsamples, previously saturated with the appropriate cations, by X-ray diffraction, infrared spectroscopy, and electron microscopy. Quantitative analysis using analytic procedures was attempted. Smectite and vermiculite percentages were determined by the methods of Alexiades and Jackson (4,5). Micas were determined through the total potassium content (6). The predominant mineral was montmorillonite, which made up 27 percent of the total soil dry weight. Other minerals were muscovite (13 percent), kaolinite (8 percent), and vermiculite (2 percent).

PLACEMENT OF VERTICAL MOISTURE BARRIER

The contractor engaged a subcontractor for the fabric placement. The subcontractor used a Parson's 500 trenching machine with a special attachment that loaded the excavated material directly onto a dump truck. The trenching machine boom was fitted with a sliding shoring to hold the Typar roll vertically in the excavation, unroll it as the machine progressed, and prevent collapse of the earth wall. A portable paving machine batched the one-sack cement-stabilized base that topped the trench gravel backfill.

The subcontractor began placing the fabric on February 4, 1980, and completed the work on May 21. On the most successful day 485 ft (147.7 m) of the fabric were placed. The daily average was 350 ft (106.6 m). The subcontractor said that if the specification had been less rigid for the backfill the work would have been done for $16 per foot rather than the bid price of $21 per foot.

MATRIX SUCTION SENSORS

Suction is the energy per unit weight of water with which the water is held within the soil. The most common types of field sensors of soil suction include porous blocks (resistivity or thermal blocks) and psychrometers. The selection of sensor type was based primarily on two criteria, the proposed length of the monitoring period and the range of the suctions expected.

Because the site response would be monitored for several years, stable equipment was required. The long-range stability of thermal blocks is dramatically higher than that of resistivity blocks, and thermal blocks are less susceptibile to contamination or corrosion than are psychrometers, which are sensitive to corrosion of the thermocouple.

The preliminary site reconnaissance indicated moisture contents at and above the plastic limit, which corresponds approximately to suctions above -3 bars. Therefore, most of the time the measurements were expected to lie in the range of 0 to -1 bar, and only occasionally were they expected to become more negative. In this range the sensitivity of suction with respect to changes in relative humidity is drastic, and so is its dependence on temperature. This sensitivity and dependence greatly reduce the accuracy of suction measurements by psychrometers. Thermal blocks are accurate in this suction range, and their sensitivity drops off only at somewhat more negative suction levels.

Thermal blocks were selected as the best alternative, and a commercially available portable data acquisition system, the MCS 6000 of Moisture Control Systems, Inc., was selected. Each sensor consists of two modules housed in cylindrical polyvinylchloride (PVC) containers and connected in-line (see Figures 5 and 6). The first module has a porous ceramic tip in which are embedded a miniature heater and temperature sensing devices. The second module contains the rest of the circuitry, including amplification and timing devices. The sensors are connected to the data display by airtight and waterproof leads and connectors.

The measurement technique consists of sensing the rate of heat dissipation in a porous material of low heat conductivity compared with that of water (7). The operation requires that a precisely controlled amount of heat be released at a fixed rate. The release takes place at the center of the block, and the temperature rise after a fixed time is then measured. The temperature rise is inversely related to the moisture content in the porous block, and moisture content is, in turn, related to the matrix suction in the block.

Figure 5. Moisture sensor timing and amplification module (top) and sensing module (bottom).

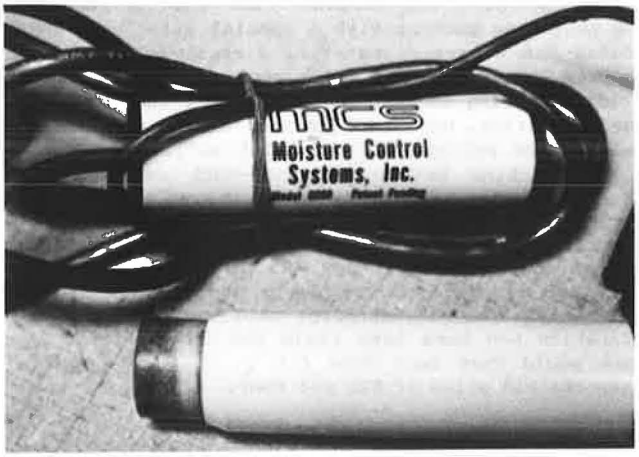

Figure 6. Sensing module ready for installation.

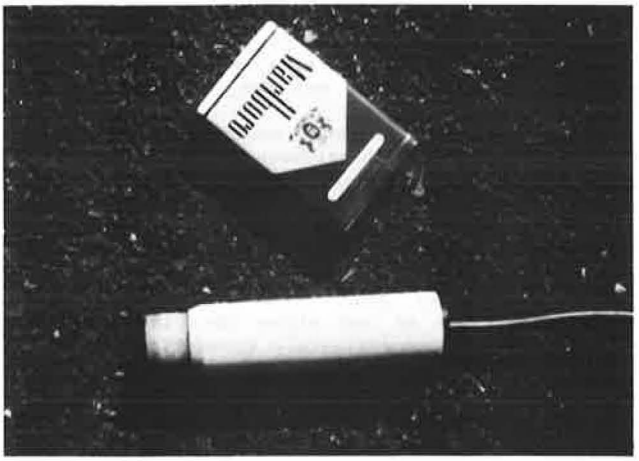

The porous block is designed to achieve two main objectives:

1. The pore size distribution has to be such as to prevent complete desaturation within the range of matrix suctions to be measured, and
2. The size of the block has to be sufficient to prevent the heat pulse from affecting the temperature of the pore water in the surrounding soil (8). (The heat pulse must be contained within the block to avoid the need to calibrate the sensor for each specific soil.)

The sensor's output is not affected by the conductivity of the soil solution (9). The only environmental changes, other than matrix suction changes, that can affect the sensor's output are temperature changes. Temperature changes can cause changes in the thermal conductivity of the soil solution and in the output of the temperature sensing devices. This dependence has been found (9) to be small for higher suctions, but below -10 bar it can become significant. Nevertheless, the MCS sensors (7) are temperature compensated. The induced changes can be neglected provided that the rate of temperature change is less than 0.1°C per minute.

Two major uncertainties are associated with measurements with thermal blocks: (a) the nonunique suction-moisture content relationship of the block and (b) whether the measurement is purely matrix suction or is intermediate between this and the free energy of the soil solution.

Characterization of the hysteresis of the MCS thermal blocks was not attempted. However, reported typical errors due to hysteresis (10, p. 128) are ±0.25 pF. Because the expected suction range falls in the upper (less negative) suctions, any error due to hysteresis will be small and can be neglected.

The second uncertainty occurs because the boundary between the porous block and the clay will behave as a Donan membrane (11), which will allow the passage of water and ions but will prevent the passage of clay particles. This will cause a Donan potential across the boundary, and, consequently, the pore solution in the block will be somewhat different from the soil solution. Therefore, the sensor reading will include, to some undetermined extent, part of the osmotic suction of the soil solution.

SENSOR CALIBRATION

The sensors were calibrated using pressure-plate extractors. The sensor was placed within a soil clod on a high-air-entry porous plate. The plate, the soil, and the sensor were then enclosed in a pressure-plate extractor. The desired suction level was achieved by increasing the air pressure in the pressure chamber and letting the pore water be in contact with water at atmospheric pressure through a high-air-entry porous plate (see Figure 7).

The porous block of the sensor had to be saturated before attempting to calibrate the sensor. This was accomplished through four cycles of vacuum-assisted saturation and desaturation by air drying. After the fourth saturation cycle the sensors were kept underwater until their installation in the field.

In this calibration technique hydraulic contact must be maintained between the pore water within the block and in the pressure plate interstices. The selection of the soil type to achieve this is critical. The water-holding capacity of the soil has to be high enough to prevent complete desaturation at the maximum suction level to be achieved, and the shrinking potential of the soil has to be low enough to prevent excessive cracking or drying of the soil mass. The soil selected for this study was Norwood silty loam, a silty clay of low plasticity.

The soil was brought to approximately the saturation percentage, and then a 1-in.-thick layer was spread over three-fourths of the surface area of the pressure plate. The sensor was placed horizontally on the soil and pushed in, leaving the porous block side approximately 0.5 in. from the plate. More soil was then piled on the porous block. The total amount of soil used was about 3 or 4 lb. Much attention was paid to obtaining a good contact between

Figure 7. Cross section of calibration set-up.

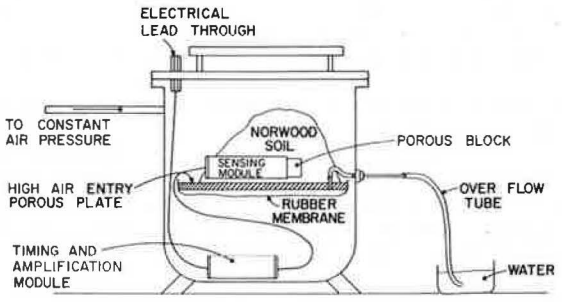

the soil and the porous block, as well as to preventing air bubbles from becoming trapped in the soil mass. The sensor was connected to an electrical lead through the wall of the pressure chamber and the connections were protected by silicone cement and impermeable tape. The soil and plate were wetted by leaving 0.5 in. of water standing on the pressure plate overnight.

The pressure chamber was closed and the air pressure was increased gradually to the desired value. Thereafter the discharge end of the outflow tube was kept underwater at all times. The assembly was maintained under constant air pressure for about 2 weeks. Then the sensors were read for several consecutive days until the reading stabilized. The air pressure was then increased to the next desired calibration value. The outflow tube was inspected periodically to detect any excessive air bubbling, which would indicate faulty behavior of the system.

The high air pressure in the chamber has little effect on the thermal conductivity of the pore air; however, it has been reported (9) to have an appreciable effect on the output of the temperature-sensing units. This effect results in an erroneous sensor reading. To eliminate this error the sensor reading is taken after the air pressure is released from the chamber (12). The first step in reading the sensor is to clamp the outflow tube to reduce the backflow of water from the drainage line when the air pressure is released. The pressure release causes adiabatic cooling within the pressure chamber, which results in temperature gradients that can cause an erroneous reading. To eliminate the latter source of error the system is allowed to come to a uniform temperature for 15 min before reading the sensor. No attempt was made to evacuate the outflow tube; the large amount of soil used on the plates renders negligible any changes of moisture content due to backflow of the water.

The major difficulties encountered were loss of contact between the soil and the plate or between the soil and the sensor, waterproofing the electrical connections, and stopping air leaks out of the system. Most of the time the loss of contact was caused by upward bending on the perimeter of the soil clod that separated from the pressure plate. A partly successful corrective measure was to load the soil clod with a 2-lb porous stone. This was successful for air pressures below 1 bar, but above 1 bar it was not consistently successful. Loss of contact between the soil and the plate was checked for when the pressure chamber was opened.

The high air pressures in the chamber cause high partial pressures of water vapor. The excess vapor left by releasing the air pressure is partly expelled with the air and partly condensed within the pressure chamber. Condensation on the soil clod will result in the alteration of its moisture content, an effect that is minimized by using a large amount of soil. A more difficult problem is created by condensation on the electrical connections of the sensor. Connections must be airtight under several atmospheres of pressure differential between the interior of the connection and the outside of the waterproofing. Waterproofing with silicone cement and impermeable tape was used in this study, but the technique was not consistently successful.

Minor air leaks from the system can be difficult to detect but can induce excessive drying of the plate due to loss of vapor. In the short run this will alter the matrix suction within the chamber and will cause a defective calibration; however, after a somewhat longer time the air leaks will desaturate the porous plate. This is evidenced as frequent bubbling through the outflow tube. The sensor readings provide another indication--the readings will not stabilize but will continue to increase constantly. As an attempt to minimize these effects equilibration time was extended and the sensors were read several days after they appeared to have stabilized.

The sensors had been calibrated by the manufacturer with pressure-plate extractors at suction levels of -0.3 and -0.6 bar. In this investigation they were calibrated at approximately -0.6 and -1.0 bar using a 1-bar pressure-plate extractor, and at -2.0 and -4.0 bar using a 15-bar pressure-plate extractor. All of the calibration data available are shown in Figure 8. The broad band of scatter of the results is a clear indication of the variability of porous blocks.

The manufacturer describes a procedure to extrapolate the calibration curve based on the -0.6 bar calibration point. This curve for one of the sensors is presented in Figure 9. The calibration data

Figure 8. Calibration results.

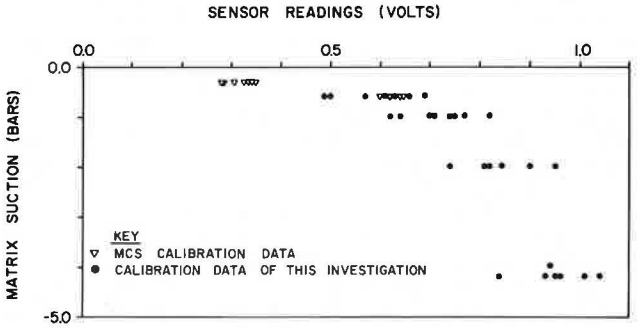

Figure 9. Comparison of typical calibration results.

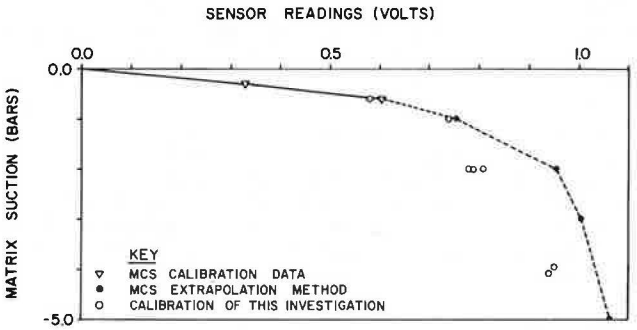

obtained by the manufacturer match those obtained in this study; however, the extrapolated curve does not provide an acceptable approximation to the calibration points below -0.6 bar. The errors that can occur when using this approximate method are so great that they render the method questionable. The stabilization of readings was good and they repeated fairly well, except when there was condensation on the electrical connections.

All of the results indicate that the sensors are sensitive down to about -0.6 bar. Below this suction level sensitivity is progressively lost. Sensitivity below -2.0 bar is so low that the readings are considered questionable beyond this point. The wide scatter of the calibration points is an indication that the average or typical calibration curves should not be used and that a particular calibration curve is needed for each sensor.

FIELD INSTALLATION OF SENSORS

Ten sensors were installed in four boreholes in two areas: boreholes 1 and 2 were drilled in the south end-west side of the highway section, and boreholes 3 and 4 were drilled in the north end-east side of the highway section. Boreholes 1 and 3 were drilled inside the moisture barrier, and 2 and 4 were drilled outside. In both areas the two borings were located approximately 3 ft (0.9 m) from one another. The relative location of the two areas is shown in Figure 4.

At the south end-west side location three sensors were installed in each borehole at depths of 3 ft (0.9 m), 6 ft (1.8 m), and 9 ft (2.7 m) from the paved surface. At the north end-east side only two sensors per boring were installed at 4 ft (1.2 m) and 9 ft (2.7 m). The relative location of the sensors, the barrier, and the paved surface is shown in Figure 4.

The main concern in the field installation was to achieve good hydraulic contact between the porous block and the in situ soil. This is especially crucial for soils that have a high potential for shrinkage. If the contact between the porous block and the surrounding soil is lost, the water transfer will take place only in the vapor phase (10). This will cause a dramatic increase in equilibration time, and when equilibrium is reached the suction in the porous block will be the total suction of the surrounding soil instead of that of the matrix suction. To minimize the risk of losing contact between the block and the surrounding soil the sensors were embedded in a layer of Norwood soil identical to that use in the laboratory calibration of the sensors. The borings were 8 in. (20 cm) in diameter and 9 ft (2.7 m) deep. The bottom of the boring was tamped and a layer of Norwood soil was placed. The sensor was laid horizontally with the porous block located close to the wall of the boring. More Norwood soil was added to cover the sensor and then lightly tamped. The borehole was backfilled to the next installation level with the soil extracted during drilling. The soil was backfilled in lifts 1 ft (30.5 cm) thick. Between lifts the soil was tamped to achieve a good seal at the side of the borehole. The electrical connections were run up the borehole walls. Boreholes 1 and 3, which were drilled within the barrier, were also covered with asphalt concrete when the backfilling operation was completed in order to restore the original pavement surface and prevent any extraneous water infiltration.

PRELIMINARY RESULTS OF MEASUREMENTS

The sensors were installed in October 1981. At the time of installation the porous blocks were saturated, but the Norwood soil was in an air-dry condition. Therefore, the surrounding soil had to give water to the Norwood soil to reach equilibrium. This is believed to have imposed a long but undetermined equilibration time.

At present, records are available for only 1 year, and it is thought that longer records are needed before appropriate conclusions can be formulated about the trends and the performance of the vertical moisture barrier. The available readings of three pairs of sensors are presented in Figure 10. The two sensors of the left part of Figure 10 are installed in boreholes 3 and 4 at a depth of 4 ft (1.2 m). The two sensors of the center part of the figure are installed in boreholes 1 and 2 at a depth of 6 ft (1.8 m). The two sensors of the right part of the figure are installed in boreholes 3 and 4 at a depth of 9 ft (2.7 m). In each case the readings of the pairs of sensors reflect the suction change across the vertical moisture barrier. Two readings of the sensor at 9 ft inside the barrier are thought to be in error; both readings were out of the range of the sensor. In both cases the faulty reading is attributed to malfunction of the sensor, probably caused by water leaks that affected the electrical circuitry.

The purpose of a vertical moisture barrier is to protect the soil mass inside from extreme fluctuations of water content. This is accomplished by increasing the distance water must travel to get into or out of the soil. A very deep barrier would eventually reduce to zero the fluctuations of water content on the inside. However, from a practical standpoint, the depth of the barrier has to represent a compromise between the cost of installation and an acceptable level of moisture content oscillations of the foundation soil. With the 9-ft barrier depth selected for this study, it was expected that the soil suction inside the barrier would follow the outside trend to some extent but that the oscillations would be considerably damped out. The measurements to date clearly show that this is the case.

During the first half of the monitoring period the soils outside the barrier showed suctions close to zero, which indicates that the soils are almost saturated. The soils inside the barrier were not saturated to start with, but they gradually wetted up as indicated by their suctions that approach zero. However, it took soils inside the barrier about 35 weeks to reach suction levels similar to those of soils outside the barrier. The unusually wet conditions outside the barrier were caused by the long rainy season that occurred during the autumn and winter months of 1981 and 1982. During the second half of the monitoring period, the soils inside the barrier have shown almost no variation in suction level; however, the soils outside have dried out to significant negative suction levels that correspond to the dry conditions during the summer of 1982.

Other measurements are being made. In the laboratory suction-moisture content relations are being determined for soils from various depths. Other fundamental characteristics of the soil, such as cation exchange capacity and exchange sodium percentage, are also being measured. In the field periodic profile measurements are being made with the GM digital profilometer and changing roughness patterns are being analyzed. It is too early in the life of the rehabilitated pavement to expect any significant increase in roughness or other distress, and none has been observed.

SUMMARY AND CONCLUSIONS

A vertical moisture barrier was installed on I-37 in San Antonio and has been in service for more than 2 years. Precise matrix suction sensors were placed on both sides of the moisture barrier at various depths below the surface to monitor the changes of moisture and suction as they are affected by ambient conditions. The sensors are sensitive and accurate in their readings of suction above -1 bar and are expected to provide stable readings for several years. Calibration of the sensors required the use of a pressure-plate extractor in which the sensors were surrounded by a soil (Norwood silty loam) that has a known suction-moisture relation and low plasticity that helps to keep it in good hydraulic contact with the water films in the ceramic disk on which it rests during calibration. There is enough variation in the characteristic slope of the calibration curve of these thermal moisture sensors to

Figure 10. Readings of sensors at various depths.

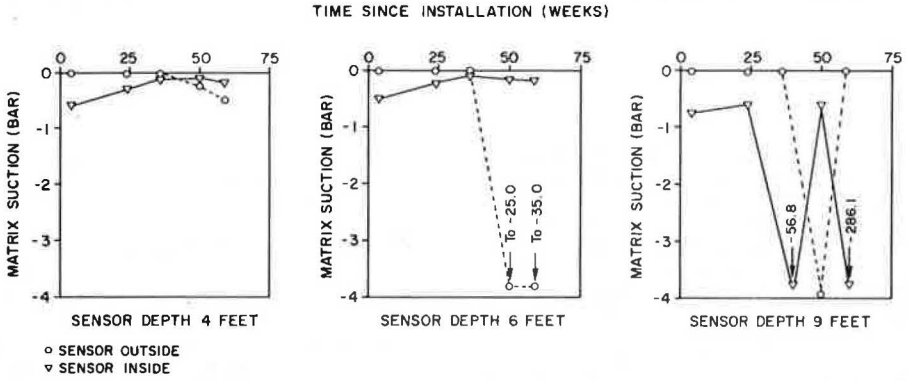

necessitate the separate calibration of each sensor instead of the use of an average curve supplied by the manufacturer. At suctions below -1 bar the devices lose sensitivity and large variations occur in the calibration curves.

The sensors were installed in boreholes surrounded by the same soil (Norwood silty loam) in which they were calibrated and placed close to the wall of the borehole to reduce the time before they would begin to sense the suction in the surrounding soil. Subsequent readings indicate that the soil on the inside of the vertical moisture barrier has remained at a relatively stable suction level whereas the soil on the outside of the moisture barrier has had significant suction changes following seasonal climatic changes. To date, the sensors have performed as expected and have proven to be sensitive devices for measuring suctions above -1 bar.

REFERENCES

1. W.G. Watt and M.L. Steinberg. Measurements of a Swelling Clay in a Ponded Cut. Univ. of Texas at Austin, Center for Highway Research, Res. Rept. 118-6, 1972.
2. M.L. Steinberg. Continuing Measurements of a Swelling Clay in a Ponded Cut. Univ. of Texas at Austin, Center for Highway Research, Res. Rept. 118-8, 1974.
3. A.W. Skempton. The Colloidal Activity of Clay. Proc., Third International Conference on Soil Mechanics and Foundation Engineering, Vol. 1, 1953, pp. 57-61.
4. C.A. Alexiades and M.L. Jackson. Quantitative Determination of Vermiculite in Soils. Soil Science Society of America, Proc. 29, 1965, pp. 522-527.
5. C.A. Alexiades and M.L. Jackson. Quantitative Clay Mineralogical Analysis of Soils and Sediments. Clays and Clay Minerals 14, 1966, pp. 35-52.
6. M.L. Jackson. Soil Chemical Analysis--Advanced Course. 2nd ed. Privately printed, Madison, Wis., 1969.
7. MCS 6000 Instruction Manual. Moisture Control Systems, Inc., Findley, Ohio, n.d.
8. C.J. Phene, G.J. Hoffman, and S.L. Rawlins. Measuring Soil Matric Potential in situ by Sensing Heat Dissipation Within a Porous Body: I. Theory and Sensor Construction. Soil Science Society of America, Proc. 35, 1971, pp. 27-33.
9. W.O. Willis and J.R. Hadley. Electrothermal Unit for Measuring Soil Suction. U.S. Salinity Laboratory, Riverside, Calif., Res. Rept. 91, 1959.
10. B.G. Richards. Behavior of Unsaturated Soils. In Soil Mechanics--New Horizons (E.K. Lee, ed.). Newness-Butterworths, London, 1974.
11. K.L. Babcock. Theory of the Chemical Properties of Soil Colloidal Systems at Equilibrium. Hilgardia 34, 1963, pp. 417-454.
12. M.S. Mayhugh. Electrothermal Unit for Measuring Soil Suction: II. Improved Calibration Procedure. U.S. Salinity Laboratory, Riverside, Calif., Res. Rept. 94, 1960.

Publication of this paper sponsored by Committee on Environmental Factors Except Frost and Committee on Soils and Rock Instrumentation.

Notice: The Transportation Research Board does not endorse products or manufacturers. Trade and manufacturers' names appear in this report because they are considered essential to its subject.

Characteristics of Red Clay of Douglas County, Wisconsin

BRUCE E. BROWN AND J.T. MENGEL

In the red clay region of Douglas County, Wisconsin, three types of stratigraphic succession are observed from borehole data: red clay 8 m (25 ft) thick over older red clay, red clay over brown or gray clay, and red clay over brown sand. The mean contents with standard deviation of sand (>44 μm), silt (44 to 2 μm), coarse clay (2 to 0.2 μm), and fine clay (<0.2 μm) in red clay from 28 borehole samples are 4 ± 4, 24 ± 12, 42 ± 7, and 30 ± 6. Smectite clay is dominant in the fine clay fraction; illite and chlorite are dominant in the coarse clays; and quartz, feldspars, and carbonates are dominant in the silt and sand fractions. Particle-size distribution and mineral contents correlate with the Atterberg limit values. The equations Liquid limit = 10.0 + 0.78 (% <2 μm clay) and Plasticity index = -0.1 + 0.51 (% <2 μm clay) have correlation coefficients of 0.76 and 0.84, respectively, for this body of data. The dominant failure mode in the Little Balsam Creek drainage south of Superior and in other similar locales involves drying and cracking of a surficial layer of clay that then slides as a decollement sheet over the underlying clay. This failure may have been promoted by recent cultural practice in the area.

Along the shore of Lake Superior from Michigan to the Minnesota border, is an extensive area of red-brown clay-rich sediments that have locally been dubbed the "red clay." The focus of this paper is on the characteristics of this material in Douglas County, Wisconsin. As the observed properties of the red clay are roughly similar throughout Douglas County, it is probable that the characteristics described here will be found throughout the red clay region. The red clay underlies the gently sloping Superior plain that, in Douglas County, ranges from about 190 m (625 ft) above mean sea level along the lake to about 335 m (1,100 ft) along the South Range, a sand-covered highland with a lava bedrock core. The South Range is the south boundary of the red clay region (see Figure 1). The red clay is glacially derived and consists of a thick surface layer of red-brown and associated grayish clays and brown sands. It rests on a vaguely stratified clay layer that contains large, but variable, amounts of silt, sand, gravel, and coarser material. These Quaternary age sediments are underlain, in turn, by red sandstones or black basaltic lava flows of late Precambrian (Keweenawan) age.

Figure 1. The area occupied by the red clay in Douglas County, Wisconsin.

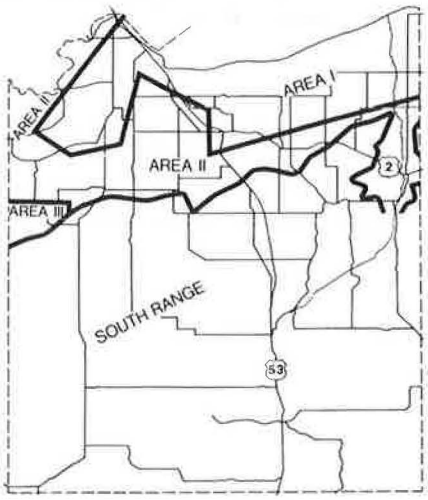

DOUGLAS COUNTY
SLOPE STABILITY TYPE AREAS

STRATIGRAPHIC SUCCESSION

The Quaternary age sediments accumulated at a time when the last continental glacier to cover the region was retreating but still filled the eastern end of the Lake Superior basin, impounding high level lakes in the western end (1). The floor of these lakes, now the surface of the plain, is dissected by a drainage system that is still in a geologically youthful stage of evolution and undergoing the kind of valley deepening and widening characteristic of such a stage.

In Little Balsam Creek drainage, south of the 320-m (1,050-ft) topographic contour, the stratigraphic succession within about 9 m of the upland surface is a clean, fine- to medium-grained brown sand containing small amounts of gravel and rare boulders. A similar sand is present along the South Range across the county. The sands are above the level of strong lake action and exhibit a knob and kettle or channeled outwash topography that contrasts sharply with the smooth upland surface of the red clay plain below an elevation of 335 m. In the Little Balsam area and elsewhere, the sand grades laterally into the clay of the plain within a short distance.

North of the 320-m contour, in the Little Balsam drainage, the gently rolling upland surface of the plain is underlain by a red-brown clay layer that can be up to 8 m thick. Beneath this layer the succession may include one of three other layers: (a) a second, older red clay; (b) brownish-gray or grayish-brown clays that show varves in some outcrops (SW1/4 sec. 34, T. 47 N., R. 15 W., for example); and (c) a fine- to medium-grained brown sand. The sands and varved clays may represent a time of temporary ice retreat between the times of ice advance recorded by the two red clays. The top of the older red clay layer shows markedly higher resistance to indentation by a simple spring penetrometer (2 to 3 TSf) than does the varved clay or basal part of the younger red clay (0.4 to 1.5 TSf). (Such resistance measurements were made as auger flights were removed from the drill hole.)

Figure 1 shows the portions of the red clay area underlain by each type of stratigraphic succession. Area I, including the coastal townships, much of Superior, and the area south of the city, is underlain by two red clays having little other material between. Area II, the St. Louis River valley and the higher elevation adjacent to the South Range, is the portion of the red clay area where upper and lower red clay layers are separated by considerable thicknesses of sand. Area III includes portions of the red clay where the varved clays occur between the two red clays.

NATURE OF RED CLAY MATERIAL

Samples from a number of representative boreholes (Figure 2) were used to determine particle-size distribution, mineral content, and Atterberg limit values.

Particle-Size Distribution in Red Clay

Samples were separated into sand (>44 μm), silt (44 to 2 μm), coarse clay (2 to 0.2 μm), and fine clay (<0.2 μm) separates using a centrifuge washing procedure after Jackson (2); dispersion was first accomplished using iron oxide removal (3) and sodium hexametaphosphate dispersant (0.5 percent). Two triangular diagrams (see Figures 3 and 4) are plotted from the observed distributions. Figure 3 (sand, silt, clay) shows this material to range from clay to silty clay with sand contents typically below 10 percent. Figure 4 (silt, coarse clay, fine clay) shows a relatively uniform ratio of coarse clay to fine clay of about 60/40 with greater variation in silt contents.

Figure 2. Locations of boreholes from which red clay samples were taken.

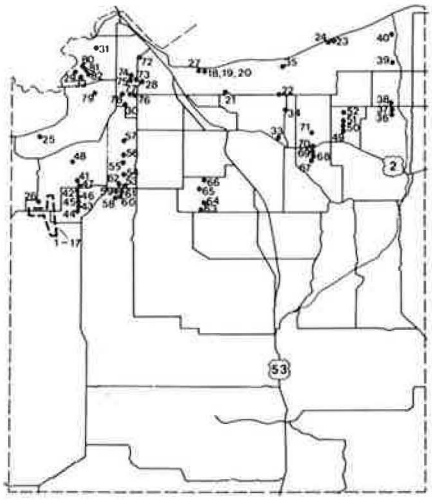

Mineralogy of Red Clay

Both nonlayer silicate minerals (quartz, feldspars, dolomite, calcite) and layer silicate clays were determined on the silt, coarse clay, and fine clay separates. The amounts of nonlayer silicate minerals were determined using an internal standard X-ray method.

For quartz, calcite, and dolomite, it was possible to prepare standard mixtures with an alpha-alumina (corundum) internal standard. The results for these three minerals are thought to be reliable to within ±5 percent. No adequate primary standards are available for the feldspars in these samples. Using relative line intensities it was possible to achieve good relative values for the feldspars from sample to sample, but the absolute amounts are estimates only. From this procedure, an estimate of the total clay mineral content can be derived by difference (i.e., 100 - percentage quartz + percentage calcite + percentage dolomite + percentage feldspars). Three major clay species were identified in all of the red clay samples. Smectite (montmorillonite) is indicated by the presence of a line near 18A on glycolated samples, chlorite by the presence of a heatstable 14A line plus subsidiary orders, and illite by the presence of a line at 10A plus subsidiary orders. Interstratified clays were present but minor and kaolinite, also minor, was not easily identified because of the presence of chlorite. To accurately determine the amounts of smectite it is necessary to carry out size separations. Whole-sample X-raying underestimates smectite and results in less consistent data.

Clay mineral percentages were derived from X-ray peak intensities using scale factors appropriate to the clay species and normalizing sums to 100 percent. Table 1 gives a summary of mineral content data. Triangular diagrams (Figures 5 and 6) summarize the proportions of clay versus nonclay minerals in the red clay and the proportions of illite to chlorite to smectite in the fine clay (where no nonclay minerals are detected).

Figure 6 shows smectite as the most variable component of the fine clay fraction. There is a rela-

Figure 3. Sand, silt, and clay contents for red clay samples taken from boreholes 12, 18, 21-33, 35, 36, 38-40, 42, 72, 74, 75, 77, and 79-82.

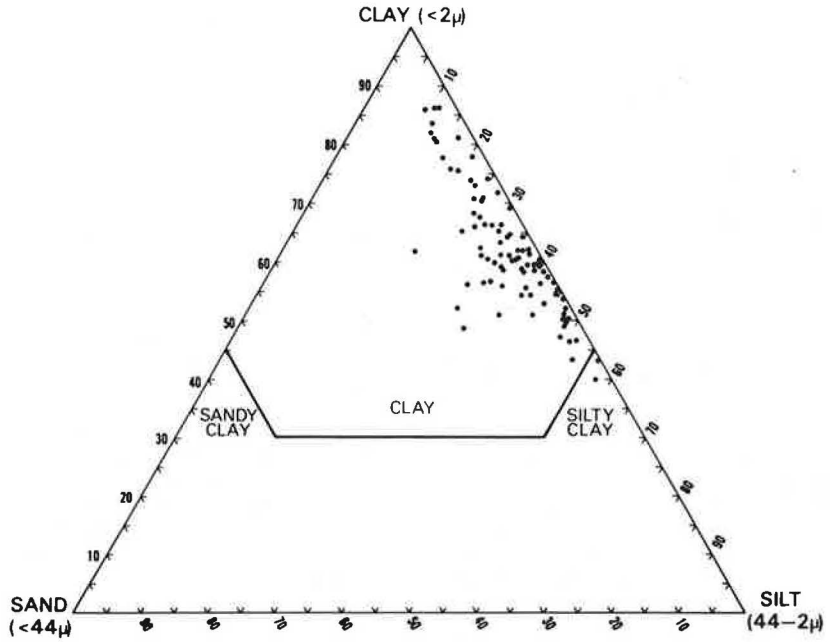

Figure 4. Silt, coarse clay, and fine clay contents for the red clay from boreholes 12, 18, 21, 22, 23, 24, 42, 72, 74, 75, 77, and 79-82.

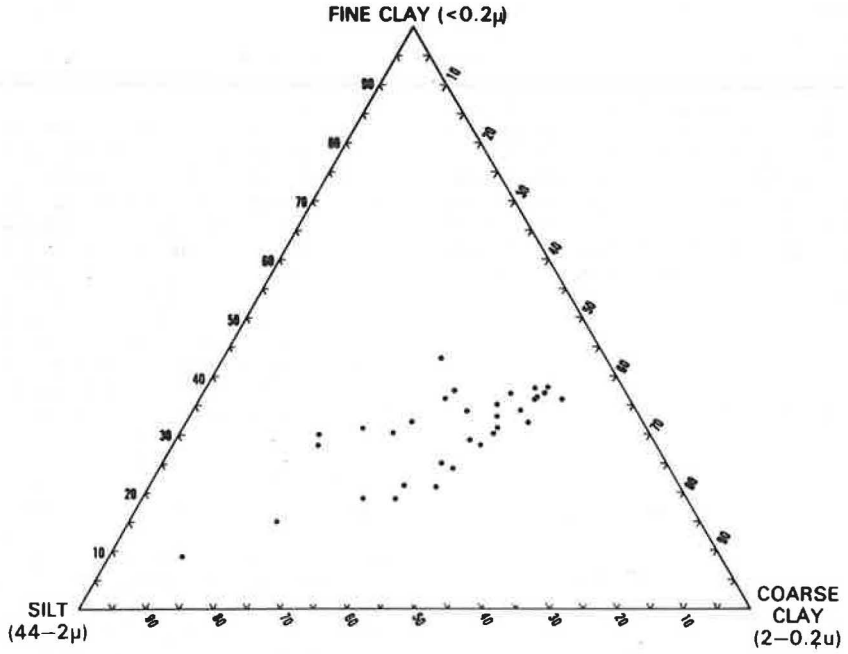

Figure 5. Relative proportions of clay minerals (quartz and feldspars) and carbonates in red clay.

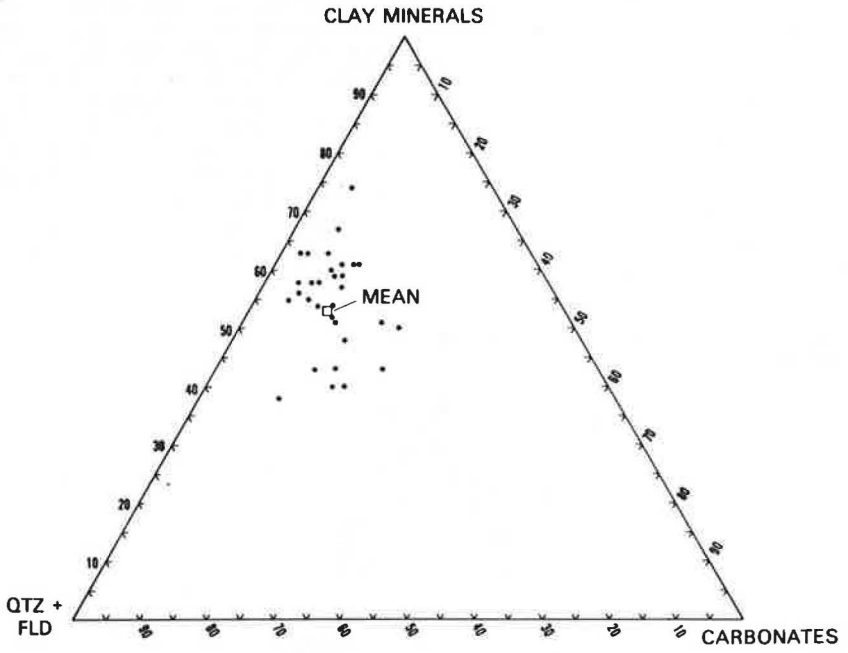

tionship between the mineral content of a separated fraction and the size range of the separate. This relationship is shown in Figures 7 and 8. Figure 7 contains cumulative curves where each component considered (quartz, feldspar, carbonates, whole sample) is normalized to 100 percent and its cumulative distribution is plotted versus the logarithmic phi scale. As expected, the nonclay minerals are coarser than the red clay as a whole. When the derivatives of these cumulative curves are plotted in Figure 8 (percent phi/phi unit versus phi), all of the nonclay minerals peak in the region of 9 phi (μm). Carbonate has a high differential peak because there is little carbonate in the sand or clay fraction so the cumulative curve for carbonate (Figure 7) rises very fast in the silt range. The high proportion of primary minerals in the size range 90 to 120 (2 to 0.2 μ) is indicative of the glacial rock flour component of the red clay and of the lack of weathering attack on the material.

The distribution of clay mineral species as a function of particle size is given in Table 2 where the percentage of illite in silt plus the percentage of illite in coarse clay plus the percentage of illite in fine clay is set to 100 percent, and the same is done for smectite and chlorite. These nor-

Figure 6. Relative proportions of smectite, illite, and chlorite in fine clay (<0.2 μm) fraction.

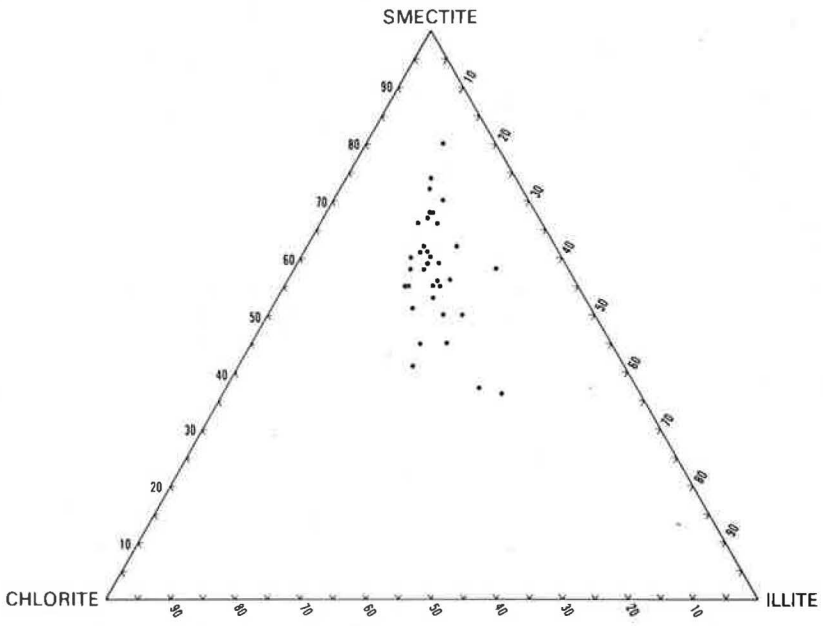

Figure 7. Cumulative curves for mineral species in red clay.

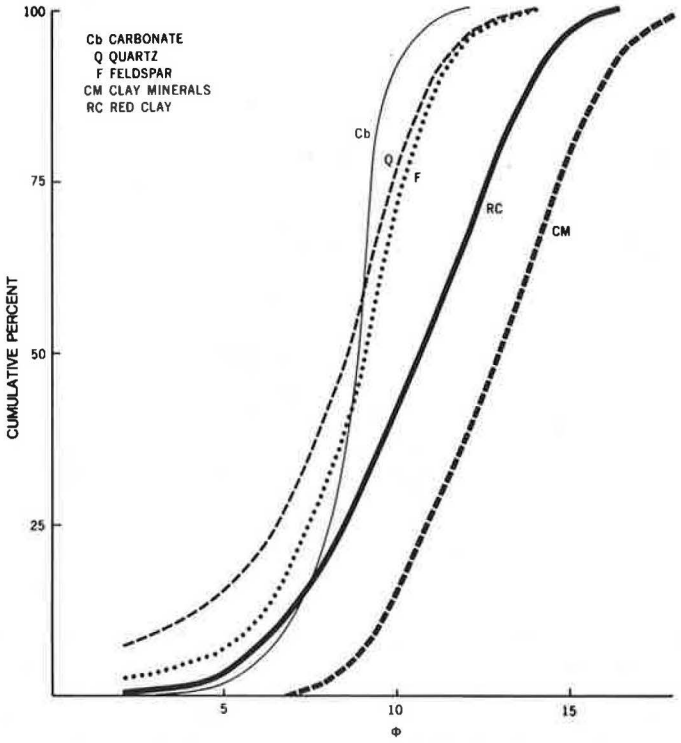

Table 1. Average percentage of components of red clay derived from the boreholes shown in Figure 2.

Size Fraction	Weight Percent Size Fraction	Quartz	Potassium Feldspar	Plagio-clase Feldspar	Calcite	Dolomite	Smectite	Illite	Chlorite	Total
>44 μm	4 (4)[a]	60 (5)	24 (10)	14 (5)	2 (1)	2 (1)	–	–	–	102
44 to 2 μm	24 (12)	34 (4)	15 (4)	14 (4)	7 (5)	15 (5)	2 (2)	5 (2)	8 (4)	100
2 to 0.2 μm	42 (7)	19 (5)	13 (4)	10 (4)	5 (5)	6 (3)	9 (3)	13 (4)	25 (4)	101
<0.2 μm	30 (6)	–	–	–	–	–	60 (7)	19 (4)	20 (5)	99
Weighted sum	100	19	10	8	4	6	22	12	18	99

[a]Values in parentheses are standard deviations.

Table 2. Normalization of clay mineral contents so that each species sums to 100 percent: cumulative results.

Mineral Species	Size Fraction	Average Percent of Mineral in Separate	Average Weight Fraction of Separate	Percent in Whole Clay[a]	Normalized Clay Percent	Cumulative Sum of Clay Species
Smectite	Silt	2.4	0.256	0.61	2.8	2.8
Smectite	Coarse clay	9.0	0.398	3.58	16.3	19.1
Smectite	Fine clay	61.8	0.288	17.8	80.9	100.0
Illite	Silt	4.6	0.256	1.18	10.7	10.7
Illite	Coarse clay	11.4	0.398	4.54	41.1	51.8
Illite	Fine clay	18.5	0.288	5.33	48.2	100.0
Chlorite	Silt	7.1	0.256	1.82	10.7	10.7
Chlorite	Coarse clay	23.8	0.398	9.47	55.8	66.5
Chlorite	Fine clay	19.7	0.288	5.67	33.4	100.0

[a]Product of average percent of mineral in separate and average weight fraction of separate.

Figure 8. Curves derived from Figure 7.

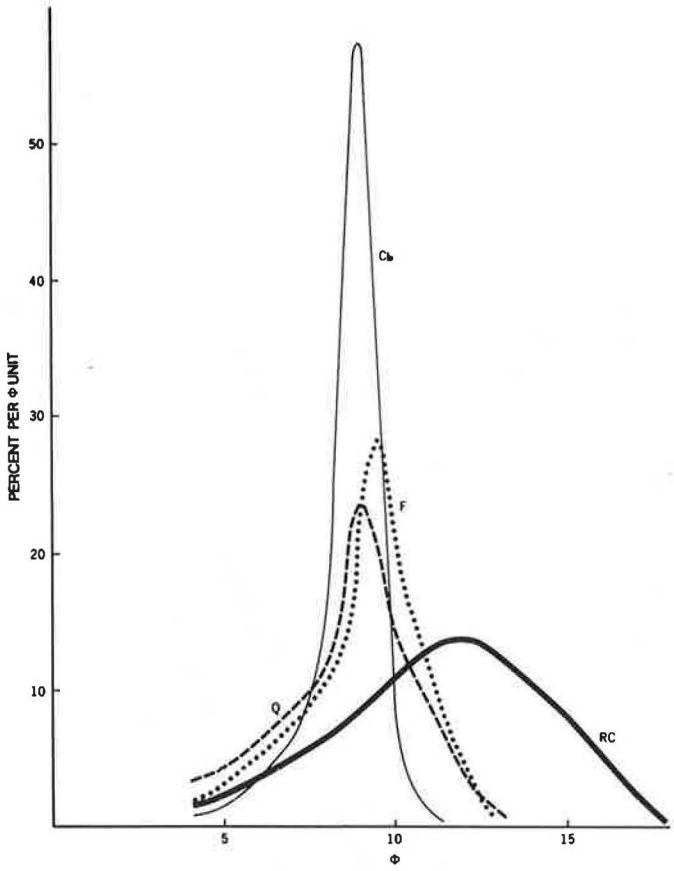

malized values show that more than 80 percent of the smectite occurs in the fraction finer than 0.2 μm, and more than 50 percent of the illite and chlorite occurs in the silt and coarse clay fractions. This suggests that the shrink-swell behavior of the red clay is closely related to the amount of <0.2 μm clay. However, the Atterberg limit values correlate no more strongly with the percentage <0.2 μm clay than with the <2 μm clay.

CORRELATION OF ATTERBERG LIMIT DATA WITH MINERALOGICAL AND SIZE DISTRIBUTION DATA

The data distribution shown in Figure 9, a plot of liquid limit versus plasticity index, is another indication of the mineralogic uniformity of the red clay (represented by points in the figure). Casagrande (4) has shown that sample groups following the A line come from soils having mineralogic uniformity.

Figures 10 and 11 show the relationship of the plasticity index (PI) values and the liquid limit (LL) values to the content of <2 μm clay (circled values are not included in the regression calculation). This relationship defines "activity" (5, p. 107). A least squares fit of a straight line to these two data clusters generates the following equations.

$$PI = -0.1 + 0.51\ (\%<2\ \mu m\ clay) \quad r = 0.84,\ s_{y.x} = 3.0 \tag{1}$$

$$LL = 10.0 + 0.78\ (\%<2\ \mu m\ clay) \quad r = 0.76,\ s_{y.x} = 5.8 \tag{2}$$

$$PI = 0.65\ LL - 6.6 \tag{3}$$

Figure 9. Plasticity index versus liquid limit.

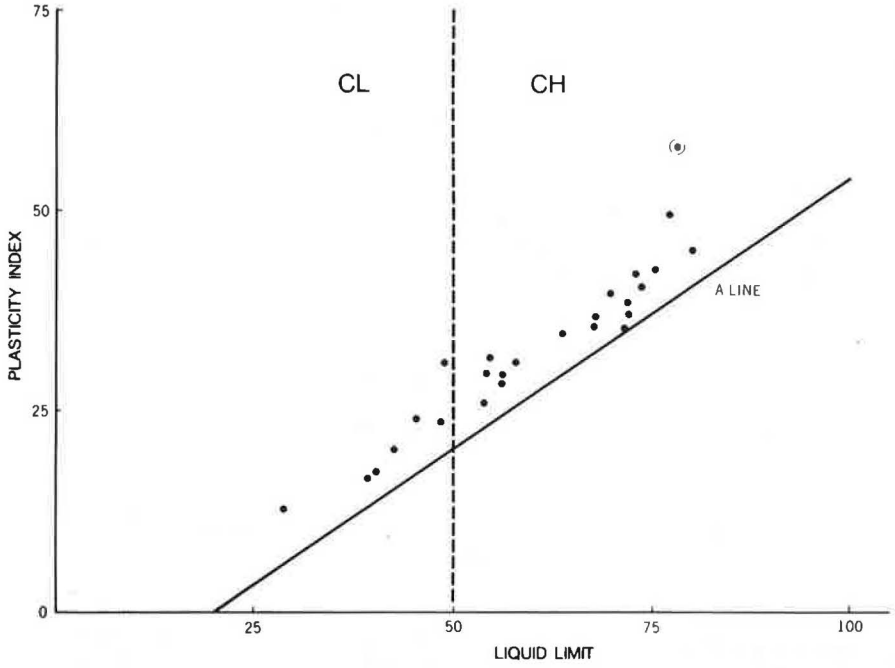

Figure 10. Plasticity index versus percent <2 μm clay.

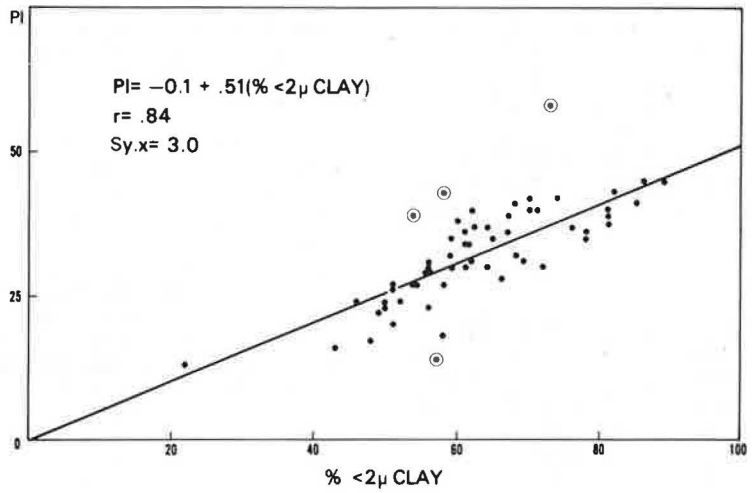

The slope of the line (activity) for Equation 1 falls about midway between accepted values (5) for illite clays (activity = 0.9) and kaolinite clays (activity = 0.3). This clay contains significant smectite which, when pure, can give rise to very high activities (1.5 or more). The <2 μm fraction contains, on the average, about one-third minerals (quartz, feldspars, carbonates), one-third chlorite + illite, and one-third smectite. This distribution will produce a slope in the vicinity of 0.7 if chlorite is assumed to be like kaolinite and the primary minerals are assumed to have zero slope. The observed slope of 0.51 is therefore lower than what would be predicted on the basis of mineral content.

Equation 2 relating LL to % <2 μm clay is combined with Equation 1 to give the relationship between plasticity index and liquid limit. The parameter N (0.65) is in reasonable agreement with the value from Seed et al. (5) for a clay with 0.5 activity.

Angle of Internal Friction

Undrained triaxial shear tests run at a slow rate (6 hours to obtain failure) on three sets of core samples taken in the NE1/4 sec. 36, T. 49 N., R. 14 W. provide the best data currently available from which values of internal friction angles (0 angles) and cohesion can be obtained (Table 3). Construction site data give internal friction angles ranging from a low of 11 degrees to a high of 32 degrees. Present data suggest that an internal friction angle of about 18 to 20 degrees for the effective state is reasonable. Based on long-term natural slope angles, an internal friction angle about half as great is

Figure 11. Liquid limits versus percent <2 μm clay.

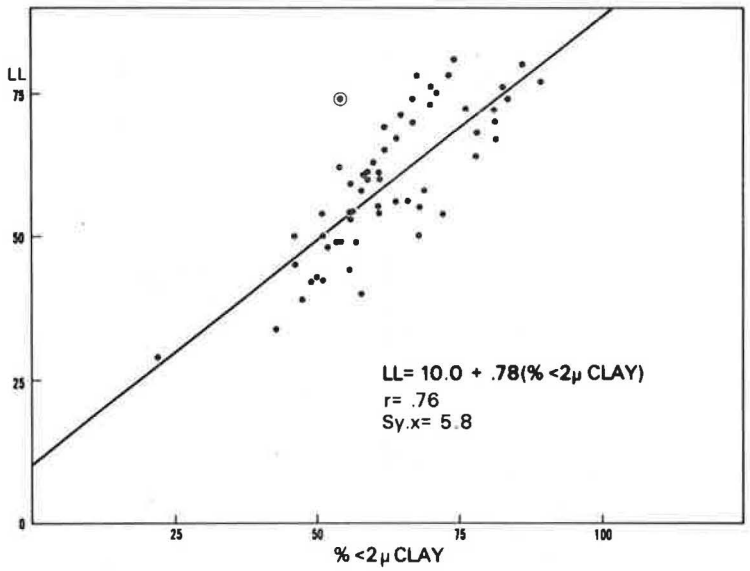

Table 3. Cohesion and angles of internal friction of three cores (NW1/4 sec. 36, T. 49 N., R. 14 W).

	Angle of Internal Friction		
Depth (ft)	Total Stress	Effective Stress	Cohesion
12 to 14	12.5	17.0	0.05 kg/cm^2
32 to 35	9.0	14.0	0.20 kg/cm^2
80 to 82	8.5	9.5	0.35 kg/cm^2

indicated for the total stress state. More study is needed to establish regional variations in materials and to associate internal friction angles with particular stratigraphic units.

SLOPE FAILURE IN RED CLAY

An important failure mode, which has been observed in the red clay material and studied in the valley of Little Balsam Creek (tributary to the Nemadjii River) (6), involves (a) loss of toe support at the valley bottom, (b) surficial cracking of the clay, and (c) sliding of blocks of clay material as on a decollement surface. Factors that appear to favor such failure include (a) smectite-rich clay with substantial shrink-swell capacity, (b) decreased infiltration and greater runoff in recent times with consequent rapid stream erosion, due perhaps to logging and agricultural practices, and (c) a possible increase in surficial drying of the clay since the cutting of the climax forest.

Cracking of these soils during the growing season is well known (1, p. 114). Such behavior is not unlike that of soil order Vertisol (8, p. 375). Vertisol soils are smectite-rich soils that develop in climates with a pronounced dry season and that cause problems for construction and agriculture even on the flat. Logging operations of the past century may have exacerbated the cracking behavior and contributed to the rate of slope failure. This possibility can still be examined; Hole (7, p. 114) reports virgin soils (Ontonagon series) under two-century-old white pine trees on Madeline Island of the Apostle group. Cracking behavior of virgin and cultivated soils can still be compared.

Cracking apparently contributes to slope failure by providing conduits that rapidly transmit water to the base of the cracked zone. In this zone a subsurface layer, which is a layer of weakness due to its higher moisture content, develops. This weak zone promotes decollement-sheet-like sliding of the surficial blocks. This type of failure is particularly evident on slopes that average 15 to 18 degrees toe to crest, and such slopes are common on drainage ways in the red clay region.

CONCLUSIONS

Most of the highly active clay (smectite) is in the <0.2-μm fraction, yet the Atterberg limit values correlate no more strongly with the 0.2-μm fraction than with the <2-μm clay.

The <2 μm fraction contains about one-third primary minerals, one-third less-active clay minerals (chlorite and illite), and one-third active clay (smectite). This distribution will produce an activity in the vicinity of 0.7 if chlorite is assumed to be like kaolinite and the primary minerals are assumed to have zero slope. The observed activity of 0.5 is therefore lower than would be predicted based on the sums of the mineral contents.

An internal friction angle of about 18 to 20 degrees for the effective state is a reasonable assumption. Long-term natural slope angles indicate an internal friction angle about half as great.

Slope failure in stream valleys frequently takes the form of a cracked surficial layer sliding on a more plastic substratum.

ACKNOWLEDGMENT

This work was supported by U.S. Environmental Protection Agency grant No. G-005140-01. We wish to thank the Douglas County Highway Department and Emil Meintzner whose crew and equipment were necessary for sample collection and who ran the Atterberg limits on the samples.

REFERENCES

1. R.W. Farrand. The Quaternary History of Lake Superior. Proc. Twelfth Conference of Great Lakes Research, International Association for Great Lakes Research, 1969, pp. 181-197.
2. M.L. Jackson. Soil Chemical Analysis: Advanced

Course. Privately printed, Madison, Wis., 1956.
3. N.V. Aquilers and M.L. Jackson. Iron Oxide Removal from Soils and Clays. Proc. 17 of the Soil Science Society of America, 1973, pp. 359-364.
4. A. Casagrande. The Determination of Pre-consolidation Load and its Practical Significance. Proc., First International Conference on Soil Mechanics and Foundations, 1936.
5. H.B. Seed, R.J. Woodward, Jr., and R. Lundgren. Clay Mineralogical Aspects of the Atterberg Limits. Journal of Soil Mechanics and Foundations Division, ASCE, Vol. 90, No. SM4, 1964.
6. J.T. Mengel, Jr., and B.E. Brown. Red Clay Slope Stability Factors. Wisconsin Department of Transportation, District 8; U.S. Environmental Protection Agency, Final Rept., 1976.
7. F.J. Hole. Soils of Wisconsin. Univ. of Wisconsin Press, Madison, Wis., 1976.
8. Soil Taxonomy. Soil Conservation Service, U.S. Department of Agriculture, 1975.

Publication of this paper sponsored by Committee on Soil and Rock Properties.

Geotechnical Evaluation of Loessial Soils in Kansas

S.S. BANDYOPADHYAY

Much of western, central, and northeastern Kansas is covered with loess deposits from Bignell, Peoria, and Loveland formations along with Sangamon soils above Loveland unit. In this paper their significant geological and engineering properties are defined, and design guidelines are presented. Montmorillonite is the chief cementing agent in Kansas loess. The Sangamon soil and the Loveland loess contain more clay than the Bignell loess and the Peoria loess and have higher in situ density and less permeability. The in situ density of Bignell loess and Peoria loess is less than 85 pcf, and consolidation tests and field experience indicate that they are highly susceptible to hydroconsolidation. A key factor in the collapse potential of Kansas loessial soils appears to be the mineralogy of the soils, specifically the presence of montmorillonite as the chief cementing agent; montmorillonite has the ability to adsorb more hydrogen cations than kaolinite and thus is able to adsorb more water. Total stress parameters must be used to design loess slopes approaching the vertical, and effective stress methods are particularly applicable in dealing with saturated loess and with seepage stresses where flattened slopes are required. Saturated loess may liquefy due to the cyclic nature of earthquake loading. Stabilization and compaction of loess represent not only an antisubsidence but also an antiliquefaction measure. Proper consideration should be given to zoning of areas of collapsible loessial soils.

Loess, a wind-deposited soil composed predominantly of silt-sized particles, is found in western, central, and northeastern Kansas. Loess is also found in approximately 17 percent of the United States, 17 percent of Europe, 15 percent of Russia and Siberia, and large areas of China as well as in New Zealand and the plains region of Argentina and Uruguay. Loess appears to be formed by wind-borne deposits traveling over glacial outwash with the higher humidity of the outwash causing precipitation of the soil particles. The geotechnical properties of loess deposits and their unique characteristics are of special practical importance to the geotechnical engineer, as well as to the agriculturist. Even though Terzaghi (1) described the properties of loess as "international" when comparing the data presented by Scheidig (2) and Holtz and Gibbs (3), Peck and Ireland (4) regarded loess "not as a soil of remarkably constant and uniform properties, but as one possessing local and regional variations almost as striking as those of some glacial materials."

Present foundation and earthwork design procedures, used in connection with this incompletely understood deposit, are still nearly all empirically based. The purpose of this paper is to define the significant geologic and engineering properties of Kansas loessial soils, to identify the potential geotechnical problems associated with them, and to present design guidelines related to these soils. Data from numerous open project files of the Kansas Department of Transportation have been used in developing this paper as well as material from a variety of published reports.

GEOLOGY

The major sources of loessial soils in Kansas are the Platte River valley of western Nebraska, the Missouri River valley, and the Republican River valley. The deposition of silts from these sources is generally attributed to eolian action. The stratigraphy of the major loess members and associated Pleistocene strata in Kansas is shown in Figure 1.

Bignell Member

Significant deposits of Bignell, the youngest of the major loess units, have been found in northwestern (thin and discontinuous) and northeastern (Missouri River valley bluffs in Doniphan County) Kansas. Bignell loess is so similar to Peoria loess that they can hardly be distinguished unless the Brady soil occurs stratigraphically below it (5). The Brady soil was formed during a short interglacial interval known as the Bradyan substage. The Brady profile is moderately to poorly drained and the depth of leaching ranges from 1 to 3 feet. Molluscan fauna fossils are sometimes contained within the Bignell loess.

Peoria Member

Typically yellow-tan in color, the Peoria loess occurs predominantly in Kansas and was deposited during the interval between the Iowan and Mankato glacial substages in Iowa. The deposition of the Peoria loess may have occurred during the relatively dry cycle following the melting of the ice sheet. The Peoria member ranges in texture from a very fine

Figure 1. Pleistocene stratigraphy in Kansas.

Time - Stratigraphy	Rock - Stratigraphy
RECENT STAGE	Low Terraces and Alluvium
WISCONSINAN STAGE	Bignell Loess
	Fluvial Deposits
	Brady Soils
	Peoria Loess
	Fluvial Deposits
SANGAMONIAN STAGE	Sangamon Soils
	Loveland Loess
ILLINOISAN STAGE	Fluvial Deposits
YARMOUTHIAN STAGE	Yarmouth Soils
KANSAN STAGE	Pearlette Ash Bed Fluvial and Eolian Deposits Till
AFTONIAN STAGE	Afton Soils
NEBRASKAN STAGE	Fluvial and Eolian Deposits Till

sand along the Republican River in northwestern and north central areas of Kansas to medium silt and silty clay in northeastern Kansas. It is at or near the surface in approximately one-third of the area of Kansas and can be as much as 90 ft thick in some areas (Cheyenne and Doniphan Counties). The Peoria member is usually fossiliferous and calcareous (5). The base of the Peoria loess frequently displays a leached zone above the Sangamon soil.

Loveland Member

Loveland loess is well exposed in northeastern Kansas (Doniphan and Brown Counties) and has been studied in auger borings and cuts in Atchison, Leavenworth, and Wyandotte Counties. The Loveland loess is also encountered in some localities in central Kansas, particularly in Rice and McPherson Counties. The Loveland loess is yellowish brown with a grayish tint. The soil developed on the Loveland loess has been termed the Sangamon soil (5), occurs from the Missouri River valley to the Colorado state line, and has been used successfully as a stratigraphic datum. When exposed, the Sangamon soil profile is usually quite evident because of its reddish brown color.

ENGINEERING PROPERTIES

Texture, Fabric, and Clay Mineralogy

Most of the Kansas loess can be classified as silty clay loam or silt loam according to the textural classification system followed by the Kansas Department of Transportation. Results of numerous grain-size analyses on loess samples from different counties clearly show that, in general, there is a decrease in the average clay content of the samples from east to west across the state. The Sangamon soil and Loveland loess each contains more clay than the Bignell loess and Peoria loess. A general decrease in clay content with depth in Peoria loess is also noticed throughout the state. There is, however, an increase with increasing depth within the Sangamon soil. Typical grain-size distributions of four loess samples obtained from four Kansas counties and their gradation range are shown in Figure 2; the samples are identified in Table 1. About 75 percent of Kansas loess can be classified as silty loess, 20 percent as clayey loess, and the rest as sandy loess. Almost all of the loess has some plasticity when remolded. The amount of clay present has a significant influence on the engineering properties of the loess.

Figure 2. Typical grain-size distribution of Kansas loess.

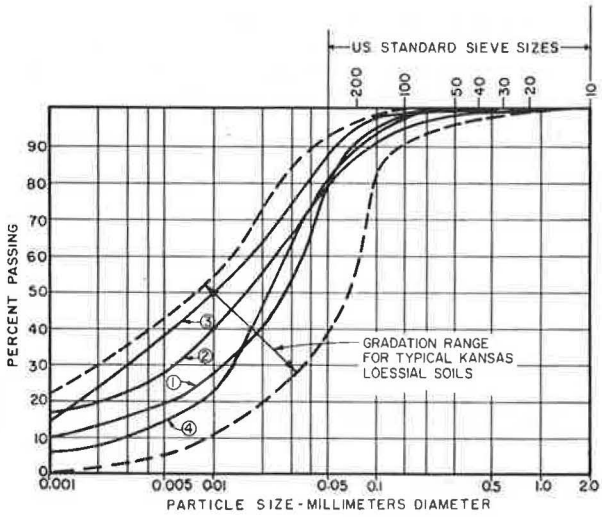

Table 1. Identification of four samples shown in Figure 2.

Sample No.	County	Member	Depth (ft)	Liquid Limit	Plasticity Index	Specific Gravity
1	Finney	Peoria	1.2	32	12	2.59
2	Wyandotte	Loveland	3.5	40	19	2.67
3	Phillips	Sangamon	4.6	47	17	2.65
4	Rawlins	Bignell	0.4	28	6	2.62

A study (6) of the elementary fabric of 224 loess samples obtained from nine counties of northeastern, north central, and northwestern Kansas revealed that the nonclay mineralogy of the sand and silt grains of all three loess units was similar. The units contained from 40 to 50 percent quartz grains, and feldspars made up about 40 percent of the nonclay mineralogy. Peoria loess had about 7 percent volcanic-ash shards. The mineral grains were partly coated with clay and sometimes carbonate and were held together by intergranular braces of clay. The Sangamon soil and Loveland loess contained more intergranular braces of clay than did the Peoria loess. The Sangamon soil also contained waxy coatings of dark-colored humic substances that must have been in the peptized state during Sangamon formation. Binocular microscope studies of 3-in. blocks of loess revealed an open, loose-textured fabric with many root holes, worm holes, and irregular openings in all three loess units.

The silt-size fraction of the loessial deposits in Kansas contains quartz, feldspars, volcanic-ash shards, carbonates, and micas, with quartz making up more than half the volume (7). The clay fraction consists of montmorillonite, illite, calcite, quartz, and feldspar, with a trace of kaolinite mineral. Montmorillonite or montmorillonite-illite interlayers are the most predominant clay constituents in Kansas loess. The presence of montmorillonite is attributed to the weathering of volcanic glass.

Figure 3 shows the X-ray diffraction patterns of the clay fraction of part of a series of samples from a failed section of road in Jewell County, Kansas (6). The major difference in the X-ray patterns of the various zones is shown by the intensity of the montmorillonite 001 reflection. The Sanagamon soil A_{1b} and B_{2b} horizons usually show a broad diffuse peak of low intensity attributed to interstratification of montmorillonite and illite. The intensity of the illite 001 and kaolinite 001 peaks does not vary significantly from one horizon to the next.

Figure 3. Typical X-ray diffractograms representative of clay fraction in Kansas loess (6).

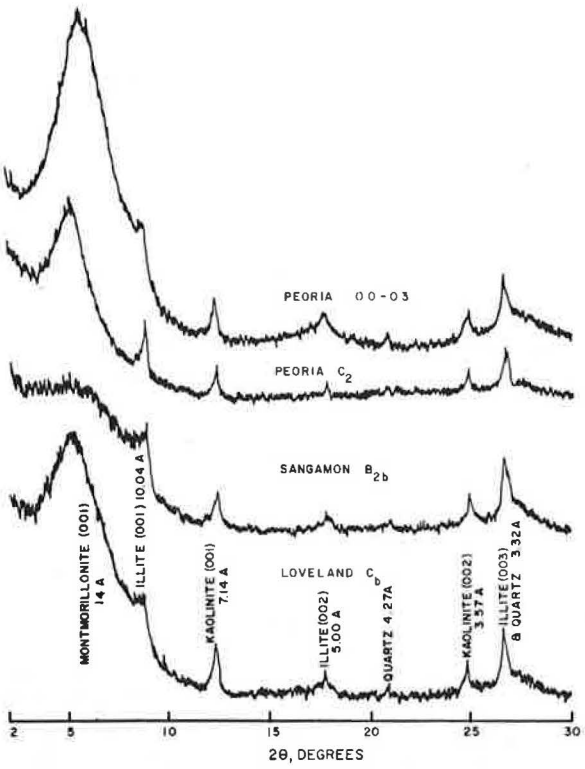

Physicochemical Characteristics

The results of chemical analyses are routinely reported by the Kansas Department of Transportation in connection with earthwork projects. A study of the test results involving loessial soils is summarized in Table 2.

Table 3 presents selected chemical characteristics of three horizons in three western Kansas loessial soils (8). The Colby soil is a light-colored well to excessively drained Regosol developed in Peorian loess. The Keith soils have a darker surface layer and a more clayey subsoil than the Colby soils. The Richfield soils are dark-colored, moderately fine-textured, chestnut soils. The moderate amounts of organic matter and its decrease with depth are characteristic of soils formed under grass in this climatic area. The high organic matter content of Colby A horizon, compared with that of the other soils, occurred because the Colby soil was in native grassland whereas the other soils were cultivated. All profiles were on the alkaline side of neutrality. The lower pH of the surface layers compared with the underlying horizons of the loessial soils is a normal relationship. Calcium and magnesium cations constitute from 75.9 to 91.7 percent of the exchangeable cations, a normal percentage for western Kansas soils.

Table 2. Physicochemical characteristics of Kansas loessial soils.

Chemical Characteristics	Range
pH	7.1 to 8.7
Soluble salts	0.06 to 0.90 millimhos/cm
Available phosphorus	0.01 to 0.5 meq/100 gm
Exchangeable potassium	0.4 to 2.6 meq/100 gm
Exchangeable magnesium	1.1 to 10.5 meq/100 gm
Exchangeable calcium	11.6 to 22 meq/100 gm

Loess soils with high silt content and medium salinity are dispersible and therefore may cause piping in dams built of such soils. The main physicochemical factor governing the sensitivity of a dam to piping or tunneling is the dispersion-deflocculation characteristic associated with the hydraulic conductivity of the material. For piping to set in, the soil particles must disperse and go into suspension in the seepage water passing through the dam. Increased dispersion of a soil is associated with (a) increase in cation exchange capacity, (b) decrease in cation valency, (c) decrease in ionic concentration of the pore fluid, and (d) increase in water content. The effect of dispersion can be reduced by proper compaction, but loess soils with total cation exchange capacity greater than 15 meq/100 gm (9) should be avoided in small dam construction.

Plasticity, Density, Permeability, and Shear Strength

The plasticity index of unweathered Kansas loess units tends to be highest in the eastern counties (except for Doniphan County, where the texture of the loess was undoubtedly modified by wind-deposited sediments from the Missouri River basin) and lowest in the western counties. Plasticity data of loess samples obtained from various counties are plotted as a function of 5-micron clay content (c) in Figure 4. The nature of the curve is similar to that Sheeler (10) obtained for loess in the United States, except that the plasticity index values of Kansas loessial soils are relatively higher. The high values of the plasticity index can generally be

Figure 4. Plasticity index as a function of 5-micron clay content.

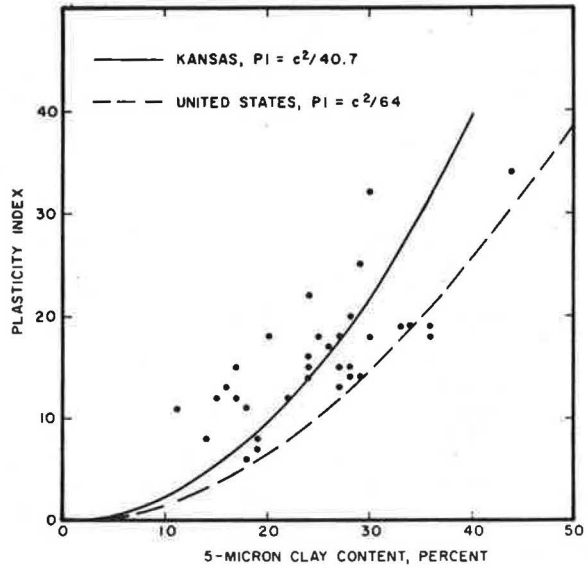

Table 3. Selected chemical characteristics of three horizons in three western Kansas loessial soils (8).

Depth (in.)	Horizon	Organic Matter (%)	pH	Exchangeable Cations (meq/100 gm soil)					Cation Exchange Capacity (meq/100gm)	Base Saturation (%)	Exchangeable Sodium (%)	Ca/Mg
				Na^+	K^+	Ca^{++}	Mg^{++}	Total				
Colby Silt Loam												
0 to 5	A_1	2.3	7.5	.63	1.81	5.88	1.80	10.12	11.48	88.2	6.2	3.3
5 to 24	AC	0.9	7.7	.67	1.07	5.31	2.20	9.25	10.82	85.5	7.2	2.4
24 +	C	0.5	7.9	.67	1.02	5.91	2.10	9.70	10.53	92.1	6.9	2.8
Keith Silt Loam												
0 to 11	$A_p + A_1$	2.2	7.2	.39	2.56	9.11	2.31	14.37	17.10	84.0	2.7	3.9
18 to 24	B_{21}	1.4	7.3	.37	1.66	10.52	3.42	15.97	18.54	86.1	2.3	3.1
28 to 40	B_{ca}	0.7	7.7	.41	1.17	10.61	3.06	15.25	16.86	90.4	2.7	3.5
Richfield Silt Loam												
0 to 5	A_p	1.4	7.1	.37	1.43	9.12	2.61	13.53	15.64	86.5	2.7	3.5
5 to 18	$B_{21} + B_{22}$	1.2	7.3	.32	1.66	9.71	2.84	14.53	16.96	85.7	2.2	3.4
27 to 38	C_{ca}	0.8	7.8	.47	0.82	10.45	2.30	14.04	15.70	89.4	3.3	4.5

associated with the relatively high percentage of montmorillonite present in the Kansas loess.

The specific gravity of loess in Kansas ranges from 2.55 to 2.67. Typical in-place density in the top 10 ft ranges from 75 to 90 pcf for Bignell loess and is always less than 85 pcf for Peoria loess. Sangamon soil and Loveland loess, because of their dense fabric, generally have higher densities than do Bignell and Peoria loess. The density of loess is a significant parameter with respect to the usefulness of loess as a foundation material. The moisture content of undisturbed loess is usually about 10 percent.

The Peoria loess shows good internal drainage and its vertical permeability is greater than its horizontal permeability (11, p. 1909). The high vertical permeability of Peoria loess, typically on the order of 9×10^2 ft/yr (9×10^{-4} cm/sec), is partly due to the existence of vertical tubules and shrinkage joints within the soil mass. Some of the root and worm holes within the loess are lined with a few thin layers of barrel-shaped calcite crystals found in a parallel arrangement forming crystal tubes in dendritic patterns. Sangamon soil and Loveland loess, because of their higher field densities and smaller pore space, have lower permeability than does Peoria loess. Remolded loess shows considerably lower permeability than in situ loess, and the vertical coefficient of permeability of remolded Peoria loess generally ranges from 1.3 ft/yr (1.3×10^{-6} cm/sec) to 8.6 x 10^{-2} ft/yr (8.6×10^{-8} cm/sec). The low permeability values are believed to occur because of densification and destruction of the tubules and joints. The permeability of in situ and remolded soil is of importance in the design of landfills, waste ponds, and hazardous waste impoundments. To avoid piping in loess dams, the upper limiting value of permeability for collapsible soils should be set at 10 ft/yr (10^{-5} cm/sec) (12).

Clay content as well as moisture and density at the time of testing control the shearing strength of loess. A study of numerous Kansas Department of Transportation open file reports revealed that in undrained triaxial tests, the angle of internal friction for Kansas loess fell between 11 and 29 degrees for samples tested with moisture contents below saturation, while the cohesion value ranged from 600 to 2,000 psf. Samples that were tested at low density and near saturated moisture conditions gave internal friction angles of zero or near zero at low normal stress. High values of cohesion resulted from high density, low moisture content, and high clay content. Plate-bearing tests reported by Holtz and Gibbs (3) and Clevenger (13) indicate that the bearing capacity of dry loess may exceed 5 tsf and may drop to 0.25 tsf when loess is wetted. The variance of density and moisture content, even within limited areas, necessitates investigations at each important site.

DESIGN CONSIDERATIONS

Foundation Design

Loessial soil found in many parts of the United States is typically considered unstable as a foundation material because of its potential for large settlements due to inundation or rise in groundwater levels (3,13-17). Terms like "collapse," "hydroconsolidation," or "hydrocompaction" have been used to describe this phenomenon that differs from classical consolidation because no water is being forced out, and, in fact, soil may be adsorbing additional water and progressively losing strength. Because not all loessial soils are susceptible to hydroconsolidation (18-20), identification of collapsible loess is of utmost importance to geotechnical engineers when structural safety and foundation economy are concerns.

The literature (3,13,17,21,22) suggests that soils susceptible to hydroconsolidation can be identified by a density criteria--that is, if density is sufficiently low to give a space larger than needed to hold the liquid-limit water content, collapse problems on saturation are likely. In general, if the density is greater than 90 pcf, the settlement will be rather small. As noted earlier, the in situ density of Kansas loess, especially Bignell and Peoria loess, in the top 10 ft is generally less than 85 pcf, which indicates potential hydroconsolidation problems. The Bureau of Reclamation (22) proposed the use of the natural dry density and liquid limit as criteria for predicting collapse as shown in Figure 5. Soil densities that plot above the line shown in Figure 5 are in a loose condition and, when fully saturated, will have a moisture content greater than the liquid limit. Another criterion proposed by the Bureau of Reclamation is based on an empirical relationship between D, dry density in place, divided by Proctor maximum dry density, and w_o-w, optimum moisture content minus in-place water content (see Figure 6). Use of clay activity to identify potentially collapsible soils has also been suggested (18,23).

Some investigators have questioned the use of density for identification. Use of a consolidation

Figure 5. Criteria for evaluating looseness and probability of collapse (22).

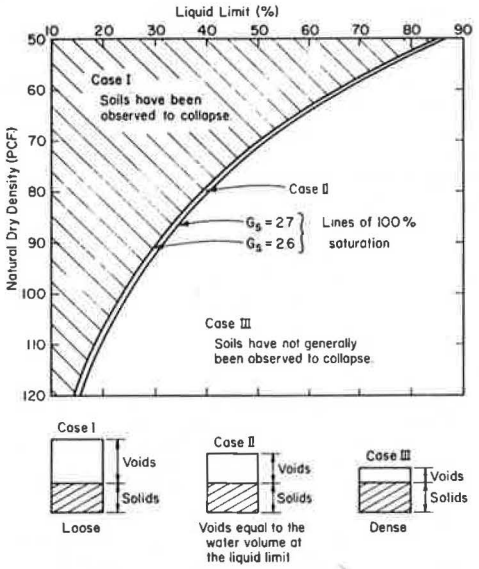

Figure 6. Criteria for treatment of relatively dry loessial soils (22).

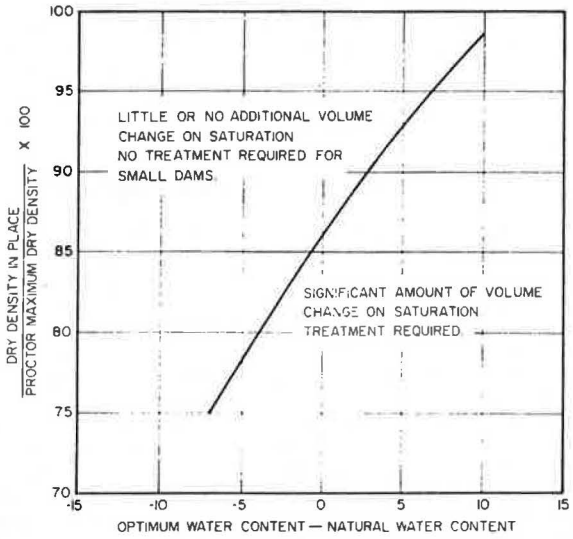

test to predict the collapse potential is generally favored (13,15,18,19,24,25). The consolidation test will give not only a qualitative determination of the possibilities of collapse but also quantitative information to permit estimates to be made of the magnitude of the collapse. Results of such a test on a loess sample obtained from Grant County, Kansas (26, pp. 233-235), are shown in Figure 7. The loess was obtained in relatively dry condition from a test pit. Consolidation tests were performed on two, as nearly identical as possible, specimens of the sample. The first test was loaded to about overburden pressure and flooded; increments of loads were then added at 48-hr intervals. In the second test, the dry specimen was loaded, unloaded, then flooded, reloaded, and unloaded again. From the results, it can be concluded that dry loess will support fairly heavy loads with only small settlements and that saturation may produce sudden large settlements. Results of similar tests and field experience indicate that Kansas loessial soils, especially the Bignell and Peoria members, are susceptible to hydroconsolidation.

Figure 7. Void ratio-pressure curve for Grant County loess (22).

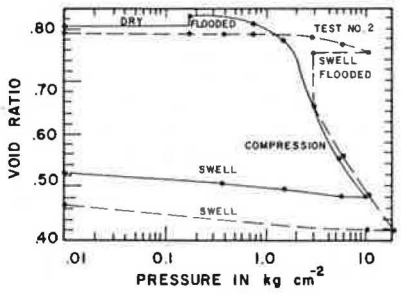

Many failures in flexible surfacing in Kansas have been attributed to moisture buildup in the loessial subgrade (27-30), especially if the surfaced grade fell within 3.5 ft of the top of the Sangamon soil. It has been found repeatedly that there is an increase in moisture content of the Peoria loess just above the Sangamon soil; this results in weakening of the subgrade. The moisture buildup just above the Sangamon soil is due to the good internal drainage and vertical permeability of Peoria loess and the high field density, smaller pore space, and more clay braces in Sangamon soil. As a result, in Kansas, Sangamon soils are generally subgraded if they are located within a few feet of the finished grade on new construction projects.

The high susceptibility of Kansas loess, especially Bignell and Peoria loess, to hydroconsolidation [in contrast with that of Palouse loess in southeastern Washington, for example, (19,20)] may be partly due to the mineralogy of the clay. The chief cementing agent in most Kansas loess deposits is montmorillonite, whereas the chief cementing agent of Palouse loess is illite, with only a trace of montmorillonite (19). Different clay minerals vary in their ability to adsorb hydrogen cations and thus in their ability to adsorb water. The number of hydrogen cations per 100 mg adsorbed by montmorillonite ranges from 360×10^{20} to 50×10^{20}, whereas the number for illite ranges from 120×10^{20} to 240×10^{20}. Therefore, montmorillonite adsorbs 1.5 to 4 times more hydrogen cations (water) than does illite. Because Kansas loess units are cemented by montmorillonite not illite, softening can be expected when the moisture content is increased. If the effective stress is sufficient, the weakened clay will fail in shear at points of contact between grains. Destruction of the intergranular supports allows the grains to move into void spaces yielding a net decrease in volume and permanent settlement.

Foundation design in loessial soils depends to a large extent on the proper identification of collapse potential and on the amount of collapse that may occur. In many cases, deep foundations (e.g., piles or caissons) may be required to transmit foundation loads to suitable bearing strata below the collapsible soil deposit. However, if the loess deposit is not susceptible to hydroconsolidation, spread footings can be successfully used (19) and are economically preferable to deep foundations. In cases where it is feasible to support the structure on shallow foundations on or above loessial soils, continuous strip footings may provide a more economical and safer foundation than isolated footings (15). Differential settlement between columns can be minimized, and a more equal distribution of stresses may be achieved with the use of strip footings. Foundation systems comprised of reaction beams formed by footing beams and load-balancing beams in the longitudinal direction have also been suggested (31) for collapsible soil. The load-bal-

ancing beams are reinforced to make the system sufficiently stiff. The performance of continuous footings, as well as other shallow foundation schemes, may be improved [i.e., the vertical displacements may be reduced, and more load-carrying capacity may be gained by the use of compensated footings (31)]. If the footing area becomes greater than 50 percent of the entire area of the building, a mat foundation should be considered for the entire foundation.

The results from laboratory or field tests can be used to predict the amount of settlement to be expected. Sometimes the cost associated with obtaining relatively undisturbed specimens, transporting the specimens in a manner that will not result in additional disturbance, preparing the specimens when they reach the laboratory, and performing elaborate time-consuming tests may prove too high; in these cases in situ testing may be used. Density-in-place measurements for loessial soils by means of standard penetration tests are not sufficiently reliable (13,32). In situ testing with plate-bearing equipment is more reliable. The test can be conducted by placing the plate apparatus at the footing bearing level and jacking against a heavy construction vehicle such as a dozer or backhoe (19). The test area is then inundated and the water level maintained for a time commensurate with the adverse hydraulic conditions being designed for. Field testing is, of course, not without its limitations and is not practical where field saturation occurs from rises in the groundwater table.

In the natural state, loess is protected against excessive wetting by a blanket of topsoil and vegetation. Stripping these materials leaves the porous loess vulnerable to rapid wetting by rainfall. Water from construction operations and from leaking pipes and improper site drainage is another cause of excessive wetting and loss of structure in loess (33). Attention to grading and drainage can do much to prevent settlement or failure of loess soils. Clevenger (13) reported the case of a grain elevator in Kansas that tilted very badly on the north side because of ponding of water on that side after heavy rains. The tilting was partly corrected by wetting beneath the southern part of the foundation. Peck and Ireland (4), however, have disputed this claim. Preconsolidation of loess foundations by ponding has been successfully applied for hydraulic structures such as dams (13) and canals (13,17,34) where the material will eventually become wetted.

Stability Analysis

The loess of Kansas occurs in flat to undulating areas in the south central portion of the state, whereas in the northeastern part the area is dissected and rough. The vegetation-covered, wind-blown, silt hills give the landscape a characteristic hummocky but soft appearance. Where there is severe erosion nearly vertical slopes prevail. Highway engineers have long been familiar with this peculiarity and have constructed cuts through these silt hills with vertical slopes.

> Loess slope stability may be analyzed using total or effective stress parameters. The selection is dependent upon the type of slope determined to be necessary. This, in turn, is dependent upon the type of loess, "silty" or "clayey", and the moisture content with particular attention to zones of saturation. Total stress parameters [are used in Kansas] to design slopes approaching the vertical as loesses suitable for such slopes have low moisture contents and strengths which are a function of negative intergranular stresses, not amenable to effective stress analysis. Effective stress methods are particularly applicable in dealing with saturated loess and with seepage stresses where flattened slopes are required (35, p. 65).
>
> Slope design in "silty loess" may require either vertical or flattened slopes depending upon the moisture content existing and anticipated (35). [In Kansas,] vertical slopes are often feasible at moisture contents below the critical moisture range and are analyzed using total stress parameters. With existing or anticipated moisture contents above the critical moisture range, but less than saturation, 2:1 slopes will normally be indicated to be adequately safe using total or effective stress analysis. Slope selection under these conditions is not critical and, for low moderate heights, will rarely require analysis. With saturated soils, effective stress analyses are required for flattened slope designs with realistic assumptions as to seepage forces existing during excavation and likely to persist after the cut is opened. Depending upon the degree of seepage forces considered and the strength parameters used, slopes will be no steeper than 2-1/2 to 1 and probably much flatter. The possibility of artesian pressures transmitted through saturated silty or sandy loesses or underlying glacial outwash sands should be given consideration (35, p. 66).
>
> Regardless of moisture content, vertical slopes are not practical in clayey loess and flattened slopes are used. Procedures discussed above (except vertical slopes) are also applicable depending upon the need to consider seepage forces (35, p. 66).

Seismic Response and Current Treatment Methods

A saturated loess may collapse under its own weight or when additionally loaded, and subsidence caused by earthquakes may be expected. Soil liquefaction is also probable due to the cyclic nature of earthquake loading. Although no report is available on the seismic response of Kansas loess, subsidence and liquefaction of loess due to earthquake loading have been reported elsewhere (36). From a detailed study of buildings and other structures after the March 4, 1977, earthquake (magnitude 7.4) in Romania, Minkov and Evstatiev (36) concluded that other conditions being equal (equal depth of the rock bed, equal thickness of the loess cover), buildings and installations built on stabilized or compacted loess bases suffered practically no damage during the earthquake. Their seismic performance is evaluated at degree VI according to the modified Mercalli intensity scale. Buildings and installations built on natural loess were affected at degrees VII and VIII. It is important to emphasize that in all buildings examined, no antiliquefaction measures had been taken. It has been reported (37) that the seismic intensity decreases by 1 to 2 degrees and the elastic modulus increases 5 to 7 times when the base density is increased by 20 to 30 percent. Stabilization and compaction of loess, therefore, represent not only an antisubsidence but also an antiliquefaction measure.

The type and amount of treatment depends on the depth of collapsible soil and the support requirements for the proposed facility. A great variety of treatment methods have been used in the past. Table 4 presents a summary by Bara (38) of various treatment methods. Further technological advances are necessary before heat treatment, ultrasonics, or chemical additives (other than lime or cement) are feasible.

The Soviets have conducted extensive studies of

Table 4. Methods of treating collapsible foundation soils (38).

Depth of Subsoil Treatment Desired (ft)	Treatment Method	
	Past and Current	Possible Future
0 to 5	Moistening and compacting (conventional extra-heavy, impact, or vibratory rollers)	
5 to 30	Overexcavation and recompaction (earth pads with or without stabilization by additives such as lime or cement) Vibrofloation (free-draining soils) Rock columns (vibroreplacement) Displacement piles Injection of silt or lime Ponding or flooding (if no impervious layers exist)	Heat treatment to solidify soils in place Ultrasonics to produce vibrations to destroy bonding mechanism of metastable soil Chemical additives to strengthen bonding mechanism of metastable soil structure (possible electrochemical methods of application) Use of groutlike additives to fill pore spaces before solidification
30+	Any of the above or combinations thereof Ponding and infiltration wells Ponding and infiltration wells with use of explosives	

chemical stabilization techniques (39,40). The methods currently employed are (a) gaseous silicatization of sandy and loessial soils, (b) strengthening of carbonate cements by polymers, and (c) chemical strengthening of alluvial soils by clay-silicate solutions. The gaseous silicatization treatment involves a mixture of soil, carbon dioxide, and a sodium silicate solution. Recent investigations by Sokolovich (40) have shown that stabilization of loessial soils by treatment with ammonia is possible. In this method, gaseous ammonia is injected via boreholes into loessial soil prone to slump-type settlements (15). The ammonia is absorbed by water films of the loessial soil and reacts with its absorbing complex. As the result of an exchange reaction with the absorbed calcium, highly dispersed calcium hydroxide is formed. Reaction of the precipitated calcium hydroxide with the silica and colloidal silicic acid of the soil leads to formation of a calcareous-siliceous binder that stabilizes the soil (15).

Zoning Considerations

Because significant differences occur in the loessial soils of different regions, a preliminary zoning of the areas of collapsible loessial soils will be beneficial to highway agencies, geotechnical engineers, geologists, and technical agencies. Factors that should be considered for zoning of loessial soils include thickness of collapsible soils; sensitivity to wetting of soils, particularly their susceptibility to self-subsidence on wetting; degree or category of collapsibility; and local experience in highway and building construction. Such zoning, if developed, will help in regional planning, site selection, and development of construction measures compatible with local soil conditions. China, where loess and loesslike soils are widely distributed in the north and the northwest and cover 6.6 percent of the country's land surface, has developed a zoning map (41-43).

SUMMARY

The widely distributed loessial soils of Kansas inevitably bear the imprints of local geographical and geological conditions. The major loess members associated with the Pleistocene age are Bignell, Peoria, and Loveland along with Sangamon soil above the Loveland unit. A trend of gradual, steady reduction in the average clay content is found from east to west across the state. The Sangamon soil and Loveland loess each contain more clay than do Bignell loess and Peoria loess. Montmorillonite is the most predominant clay constituent in Kansas loess. Calcium and magnesium cations constitute 75 to 92 percent of the exchangeable cations. Plasticity index values of Kansas loess are relatively high compared with those for the rest of the United States, and vertical permeability is greater than horizontal permeability. Kansas loess, especially the Bignell and Peoria formations, is highly susceptible to hydroconsolidation. Low in situ density and presence of montmorillonite as the chief cementing agent are two key factors responsible for the collapse potential of Kansas loess. The results from appropriate laboratory or field tests can be used to predict the amount of settlement that can be expected. Where severe erosion is present, nearly vertical slopes prevail in Kansas silty loess. Total stress parameters are used to design loess slopes approaching the vertical, and effective stress methods are particularly applicable in dealing with saturated loess and with seepage stresses where flattened slopes are required. Stabilization and compaction of loess represent not only an antisubsidence but also an antiliquefaction measure. Consideration should be given to proper zoning of areas of collapsible loessial soils.

ACKNOWLEDGMENTS

The author would like to thank Carl Crumpton for his help. Partial support provided by National Soil Services during the preparation of this paper is appreciated. The contents of this paper reflect the views of the author who is responsible for the facts and accuracy of the data presented.

REFERENCES

1. K. Terzaghi. Consolidation and Related Properties of Loessial Soils, Discussions. ASTM, Special Tech. Publ. 126, 1951, pp. 30-32.
2. A. Scheidig. Der Loess. Theorder Steinkoff, Dresden, Germany, 1934.
3. W.G. Holtz and H.J. Gibbs. Consolidation and Related Properties of Loessial Soils. ASTM, Special Tech. Publ. 126, 1951, pp. 9-26.
4. R.B. Peck and H.O. Ireland. Experiences with Loess as a Foundation Material, Discussion. Transactions, ASCE, Vol. 123, 1958, pp. 171-179.
5. J.E. Frye and A.B. Leonard. Pleistocene Geology of Kansas. State Geological Survey of Kansas, Bull. 99, 1952.
6. C.F. Crumpton and W.A. Badgley. A Study of the Clay Mineralogy of Loess in Kansas in Relation to its Engineering Properties. Research Department, State Highway Commission of Kansas, 1965.
7. A. Swineford and J.C. Frye. Petrography of the Peoria Loess in Kansas. Journal of Geology, Vol. 59, 1951, pp. 306-322.
8. K.V. Paliwal, J.A. Hobbs, O.H. Bidwell, and R. Ellis, Jr. Mineralogical and Chemical Characteristics of Four Western Kansas Soils. Transactions of the Kansas Academy of Science, Vol. 67, No. 4, 1965, pp. 617-629.

9. G. Kassiff and E.N. Henkin. Engineering and Physico-Chemical Properties Affecting Piping Failure of Low Loess Dams in the Negev. 3rd Asian Conference on Soil Mechanics and Foundation Engineering, Haifa, Israel, 1967, pp. 13-16.
10. J.B. Sheeler. Summarizations and Comparison of Engineering Properties of Loess in the United States. HRB, Highway Research Record 212, 1968, pp. 1-9.
11. R.C. Mielenz, W.Y. Holland, and M.E. King. Engineering Petrography of Loess. Geological Society of America Bulletin, Vol. 60, 1949.
12. C.C. Wood, G.D. Aitchison, and D.G. Ingles. Physico-Chemical and Engineering Aspects of Piping Failures in Small Dams. Colloquium on Failure of Small Dams, Commonwealth Scientific Industrial Research Organization, Victoria, 1964.
13. W.A. Clevenger. Experiences with Loess as a Foundation Material. Journal of the Soil Mechanics and Foundation Division, ASCE, Vol. 82, No. SM3, 1956, pp. 1-26.
14. J.E. Jennings and K. Knight. The Additional Settlement of Foundations due to Collapse of Structure on Sandy Soils on Wetting. Proc., Fourth International Conference on Soil Mechanics and Foundation Engineering, Vol. 3A, 1957, pp. 316-319.
15. S.P. Clemence and A.O. Finbarr. Design Considerations for Collapsible Soils. Journal of the Geotechnical Engineering Division, ASCE, Vol. 107, No. GT3, March 1981, pp. 305-317.
16. H.A. Sultan. Collapsing Soils, State-of-the-Art. Seventh International Conference on Soil Mechanics and Foundation Engineering, No. 5, 1969.
17. P.C. Knodel. Construction of Large Canal on Collapsing Soils. Journal of the Geotechnical Engineering Division, ASCE, Vol. 107, No. GT1, Jan. 1981, pp. 79-94.
18. J.H. Dudley. Review of Collapsing Soils. Journal of the Soil Mechanics and Foundation Division, ASCE, Vol. 96, 1970, pp. 925-947.
19. G.T. Lobdell. Hydroconsolidation Potential of Palouse Loess. Journal of the Geotechnical Engineering Division, ASCE, Vol. 107, 1981, pp. 733-742.
20. B.O. Olson. Loess Soils in Southeastern Washington. Journal of the Geotechnical Engineering Division, ASCE, Vol. 105, 1979, pp. 786-791.
21. H.J. Gibbs and J.P. Bara. Predicting Surface Subsidence from Basic Soil Tests. ASTM, Special Tech. Publ. No. 322, 1962, pp. 231-247.
22. W.G. Holtz and J.W. Hilf. Settlement of Soil Foundations due to Saturation. Proc., Fifth International Conference on Soil Mechanics and Foundation Engineering, Vol. 1, 1961, pp. 673-679.
23. C.V. Lucas. Design and Construction Studies of Shallow Land Subsidence for the California Aqueduct in the San Joaquin Valley. California Department of Water Resources, Dec. 1964.
24. J.E. Jennings and K. Knight. A Guide to Construction on or with Materials Exhibiting Additional Settlement due to Collapse of Grain Structure. Sixth Regional Conference for Africa on Soil Mechanics and Foundation Engineering, Sept. 1975, pp. 99-105.
25. H.E. Moore. The Engineering Properties of Silty Soils, Snake River Canyon, State of Washington. U.S. Army Corps of Engineers, Engineer District, Walla Walla, Washington, July 1967, pp. 1-31.
26. R.E. Means and J.V. Parcher. Physical Properties of Soils. Charles E. Merril, Columbus, Ohio, 1963.
27. J.A. Barnett and L.G. Hitzeman. Geological Report, Project Numbers 9-29-5516-(3) and 281-92-F035-3(6), Osbourne County and Smith County. Open file rept., Kansas Highway Commission, 1954.
28. J.A. Barnett and J.R. Miller. Supplemental Geological Report to Project 36-92-F092-2-(8), Smith County. Open file rept., Kansas Highway Commission, 1956.
29. D.L. Lacey. Report of Soil Survey, Project Number 36-92-F092-2(6), Smith County. Open file rept., Kansas Highway Commission, 1953.
30. W.K. Taylor and J.A. Barnett. Geological Report, Project Number 36-92-F-092-2(9), Smith County. Open file rept., Kansas Highway Commission, 1953.
31. L. Zeevaert. Foundation Engineering for Difficult Subsoil Conditions. Van Nostrand, New York, 1972.
32. C.O. Riggs and N.O. Schmidt. Foundation Design for Loessial Collapsible Soils. Presented at the April 14-18 ASCE Annual Convention and Exposition, Portland, Oregon, 1980.
33. G.A. Leonards. Foundation Engineering. McGraw-Hill, New York, 1962.
34. A.A. Beles, I.I. Stanculescu, and V.R. Schally. Prewetting of Loess-Soil Foundations for Hydraulic Structures. Proc., Seventh International Conference on Soil Mechanics and Foundation Engineering, Mexico, 1969, pp. 17-25.
35. Development of Design Criteria for Cut Slopes in Loess. Missouri State Highway Department, final rept. 74-1, April 1978.
36. M. Minkov and D. Evstatiev. On the Seismic Behavior of Loess Soil Foundations. Proc., Second U.S. National Conference on Earthquake Engineering, 1979, pp. 988-996.
37. I. Illiev. Possibilities of Reducing the Destructive Effects of Earthquakes by Artificial Alteration of Engineering-Geological Conditions (in Bulgarian). Bulgarian Academy of Science, Engineering Geology and Hydrogeology, Book 8-9, 1978.
38. J.P. Bara. Collapsible Soils. Presented at the September Annual Convention and Exposition, ASCE, Philadelphia, 1976.
39. V.E. Sokolovich. New Developments in the Chemical Strengthening of Ground. Osnovaniya Fundamenty i Mekhanika Gruntov, No. 2, March-April 1971, pp. 23-25.
40. V.E. Sokolovich and V.A. Gubkin. Gaseous Silicatization of Loessial Ground. Osnovaniya Fundamenty i Mekhanika Gruntov, No. 5, Sept.-Oct. 1970, pp. 26-28.
41. Z. Lin and W. Liang. Distribution and Engineering Properties of Loess and Loess-Like Soils in China. Bulletin of the International Association of Engineering Geology, Vol. 21, 1980, pp. 112-117.
42. Z. Lin. Engineering Geological Investigations for Industrial and Civil Construction. Bureau of Publication of the Building Industry of China, Beijing, 1981, pp. 204-235.
43. Z. Lin and W. Liang. Engineering Properties and Zoning of Loess and Loess-Like Soils in China. Canadian Geotechnical Journal, Vol. 19, No. 1, Feb. 1982, pp. 76-91.

Publication of this paper sponsored by Committee on Soil and Rock Properties.

Ultimate Bearing Capacity of Closely Spaced Strip Foundations

BRAJA M. DAS AND SAID LARBI-CHERIF

Laboratory model test results for the ultimate bearing capacity of two closely spaced, rough, shallow, strip foundations resting on sand are presented. The experimental results are compared with the existing theory. The ultimate bearing capacity of foundations increases with the decrease of the center-to-center spacing; however, the magnitude of increase is considerably smaller than that predicted by theory.

Numerous theoretical and experimental studies of the ultimate bearing capacity of isolated foundations in homogeneous and layered soils are available in the literature. However, studies of the change in the load-bearing capacity of foundations when they are closely spaced are relatively scarce. This change may be important in some foundation design problems such as rest area buildings and mass transit stations. Two questions might arise during the design: (a) How does the ultimate bearing capacity change when two shallow foundations are placed rather close to each other? (b) What is the settlement of the foundations at ultimate load as compared with that obtained when they are far apart? Stuart (1) proposed a theoretical solution for the ultimate bearing capacity of two closely spaced, rough, shallow, strip foundations on sand (see Figure 1) as

$$q_u = qN_q\alpha_q + \tfrac{1}{2}\gamma BN_\gamma\alpha_\gamma \quad (1)$$

where

q_u = ultimate bearing capacity of each foundation,
γ = unit weight of soil,
B = width of foundation,
$q = \gamma D$,
D = depth of foundation,
N_q, N_γ = bearing capacity factors, and
α_q, α_γ = efficiency factors.

The variation of α_γ and α_q with the center-to-center spacing (Δ) of foundations is shown in Figures 2 and 3. From these figures, it may be seen that for a given soil friction angle (ϕ) the two closely spaced foundations behave as one from $\Delta/B = 1$ up to a given value. This is because, at small values of Δ/B, the soil located in between the two foundations forms an inverted arch that travels down as a unit with the foundation as the load is applied. At a value of $\Delta/B = 1$, the zone or arching disappears, and the system behaves as a single unit of foundation having a width of 2B.

Figure 1. Definition of parameters for the ultimate bearing capacity of two closely spaced, shallow foundations as given by Equation 1.

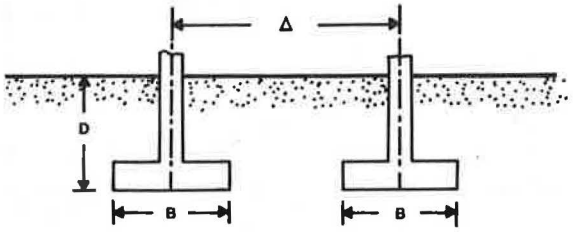

In this paper some laboratory model test results are compared with the theoretical efficiency factors. Also, based on the laboratory results, some discussion of foundation settlement at ultimate load is presented. The tests were conducted in the Soil

Figure 2. Variation of efficiency factor α_γ with center-to-center spacing of foundations [theoretical curves after Stuart (1)].

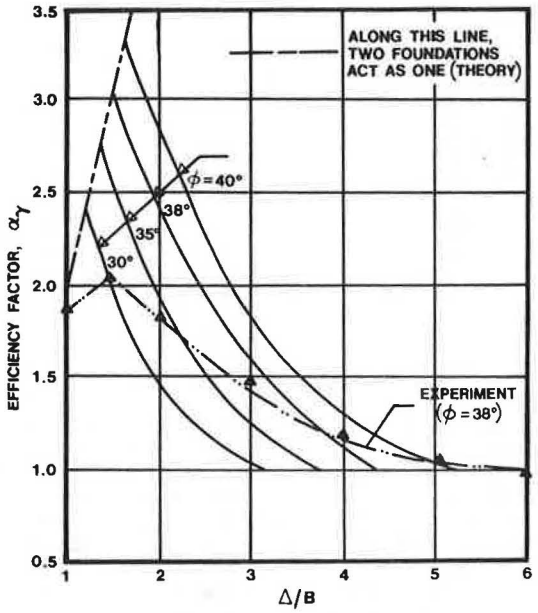

Figure 3. Variation of efficiency factor α_q with center-to-center spacing of foundations [theoretical curves after Stuart (1)].

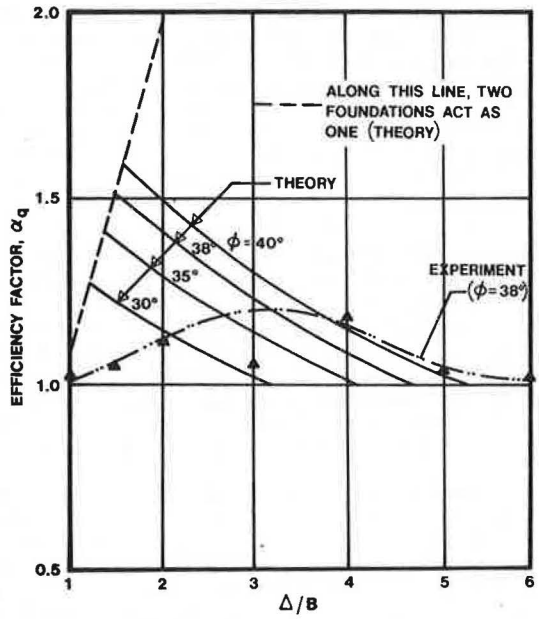

Mechanics Laboratory of the University of Texas at El Paso.

LABORATORY MODEL TESTS

Laboratory model tests were conducted in a box having a length, width, and height of 1.524 m, 0.305 m, and 0.914 m, respectively. The sand used for the tests had 100 percent passing No. 10 sieve, 87 percent passing No. 20 sieve, and 2 percent passing No. 200 sieve. The grain-size distribution of the sand is shown in Figure 4. To conduct the model tests, sand was poured in 50.8-mm layers in the test box and compacted to a unit weight of 15.88 kN/m³, which gave a relative density of compaction of about 54 percent. The angle of friction at this unit weight of compaction was determined from direct shear tests to be equal to 38 degrees. This relative density of compaction was chosen for two primary reasons, one of which is the reproducibility in the model test box. The second reason is to check the opinion of some investigators, such as Vesic (2), that interference effect on ultimate bearing capacity of shallow foundations may be practically negligible when the foundations are located on loose soil (i.e., local shear failure condition).

Figure 4. Grain-size distribution of sand used for model tests.

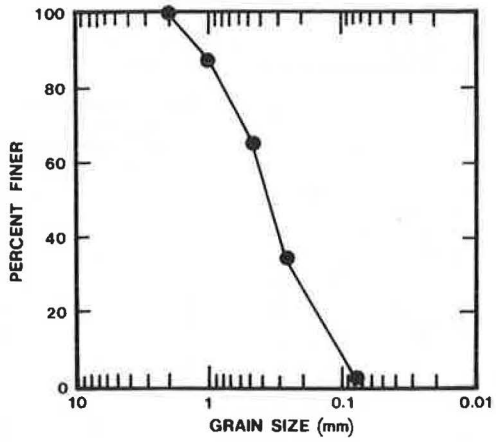

Two model steel foundations measuring 50.8 mm x 304.8 mm were used for the tests. The ends of the model foundations and the sides of the box were polished to make them as smooth as possible to keep friction resistance to a minimum. Sandpaper was glued to the bottoms of these model foundations to make them rough. The gradation of the sand on the sandpaper was similar to that used for the tests. Each model foundation was rigidly attached to a steel shaft having a diameter of 19 mm. For tests on a single foundation, load to the foundation was applied through this shaft by means of a hydraulic jack. To conduct tests on two closely spaced foundations, the steel shafts were rigidly attached to a horizontal steel crossbar 50.8 mm x 25.4 mm in cross section. Load to the foundation was applied at the center of the crossbar. The loads on the foundation and the corresponding foundation settlements were measured by a proving ring and a dial gauge, respectively.

Model tests were conducted for D/B ratios of zero and one, with center-to-center foundation spacing-to-width ratios (ΔB) of 1, 1.5, 2, 3, 4, 5, and 6. Tests on single isolated foundations ($\Delta/B = \infty$) were also conducted for D/B ratios of zero and one. After each test the sand in the test box was completely emptied and recompacted in layers before the next test was begun.

In all tests the nature of variation of load versus displacement plots was similar to the type obtained for local shear failure in soils. A typical load versus settlement plot obtained from the laboratory tests is shown in Figure 5. The ultimate load at failure for each test was determined by using the criteria proposed by Vesic (2). This means that the ultimate load in a load-settlement plot is defined as the point where the slope of the load-settlement curve first reaches zero or a steady minimum value. Figure 6 shows the variation of the ultimate failure load (q_u) for all tests conducted.

For single isolated foundations the bearing capacity factors N_γ and N_q can be determined as follows.

$$N_\gamma = [q_{u(\Delta/B = \infty,\ D/B = 0)}]/0.5\gamma B \quad (2)$$

$$N_q = [q_{u(\Delta/B = \infty,\ D/B = 1)} - q_{u(\Delta/B = \infty,\ D/B = 0)}]/\gamma D \quad (3)$$

Figure 5. Typical load-settlement curves from laboratory tests.

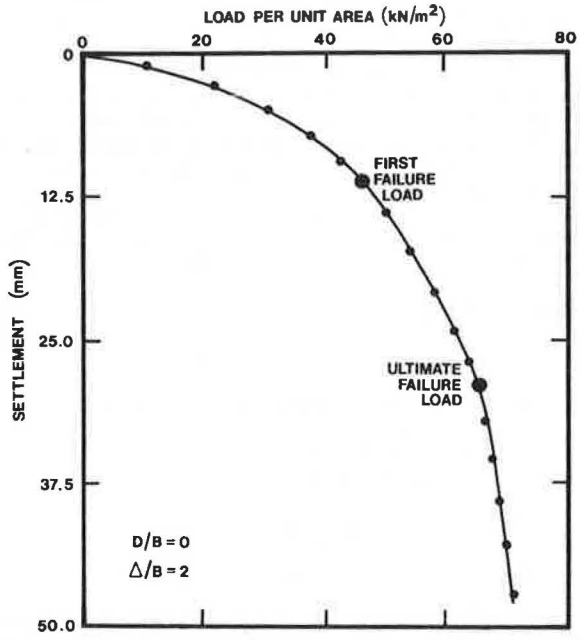

Figure 6. Variation of ultimate bearing capacity obtained from laboratory model tests.

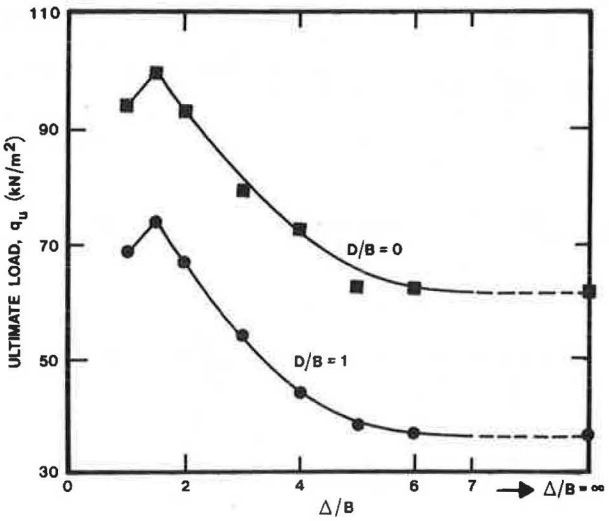

Based on Equations 2 and 3 the experimental values of N_γ and N_q were determined to be 91 and 31, respectively. This value of N_γ = 91 is in reasonable agreement with the theoretical values of Terzaghi (3) and Caquot and Kerisel (4) for a soil friction angle of 38 degrees. However, a comparison shows that this experimental value of N_q is in better agreement with the theory given by Vesic (5) and can be expressed as

$$N_q = (e^{3.8\phi \tan\phi}) \tan^2(45 + \phi/2) \quad (4)$$

According to Equation 4, for ϕ = 38°, N_q = 30.1. This compares well with the experimental results of N_q = 31.

The efficiency factor α_γ for the closely spaced foundations can be determined as

$$\alpha_\gamma = (\tfrac{1}{2}\gamma B N_\gamma \alpha_\gamma)/(\tfrac{1}{2}\gamma B N_\gamma) = [q_{u(\Delta/B,\, D/B = 0)}]/[q_{u(\Delta/B = \infty,\, D/B = 0)}] \quad (5)$$

In a similar manner the efficiency factor α_q can be determined from the following equation.

$$\alpha_q = (qN_q\alpha_q)/(qN_q) = [q_{u(\Delta/B,\, D/B = 1)} - q_{u(\Delta/B,\, D/B = 0)}] \div [q_{u(\Delta/B = \infty,\, D/B = 1)} - q_{u(\Delta/B = \infty,\, D/B = 0)}] \quad (6)$$

By using these equations and the experimental values given in Figure 6, the experimental variations of the efficiency factors have been calculated. Figures 2 and 3 also show the variation of α_γ and α_q. Comparison of the experimental results with the theory shows that, although the nature of variation of the experimental α_γ and α_q is approximately similar to that predicted by theory, their magnitudes are considerably smaller than that predicted by theory for Δ/B < about 3. Note that the value of α_q reached a maximum of about 1.2 and, for all practical purposes, may be assumed to be equal to one. The discrepancy between the theoretical and experimental values of α_γ and α_q may be due to the assumption of ideal rigid-plastic behavior of soil. Also, the theory neglects the self-weight of soil (6).

Figure 7 shows a nondimensional plot of the foundation settlement (S) at ultimate load against the center-to-center spacing of the foundation. Note that, although the ultimate bearing capacity of model foundations increased with the reduction of center-to-center spacing (Δ), it was accompanied by an increased foundation settlement, particularly for the range of Δ/B < about 4.5. This is potentially important for practical design problems where settlement normally controls.

CONCLUSION

Laboratory model test results for the ultimate bearing capacity of two closely spaced, rough, strip foundations on sand have been presented. The experimental results have been compared with the theory presented by Stuart (1). Based on this comparison, the following conclusions can be drawn.

The ultimate bearing capacity of two closely spaced foundations increases as their center-to-center spacing decreases.

The efficiency factors α_γ and α_q generally vary only in the patterns predicted by Stuart's theory for Δ/B > about 4. For Δ/B < about 4, the magnitudes of α_γ and α_q are considerably smaller than those predicted by theory.

In soils where local shear failure occurs, the value of the efficiency factor α_q is practically equal to one for all center-to-center spacings.

In these tests, the settlement of foundations at ultimate load increased with the decrease of Δ/B. The settlement is expressed by $(S/B)_{\Delta/B\,=\,1} \approx 2\,(S/B)_{\Delta/B\,=\,4.5}$.

Figure 7. Nondimensional plot of foundation settlement (S/B) against the center-to-center spacing of foundations (Δ/B).

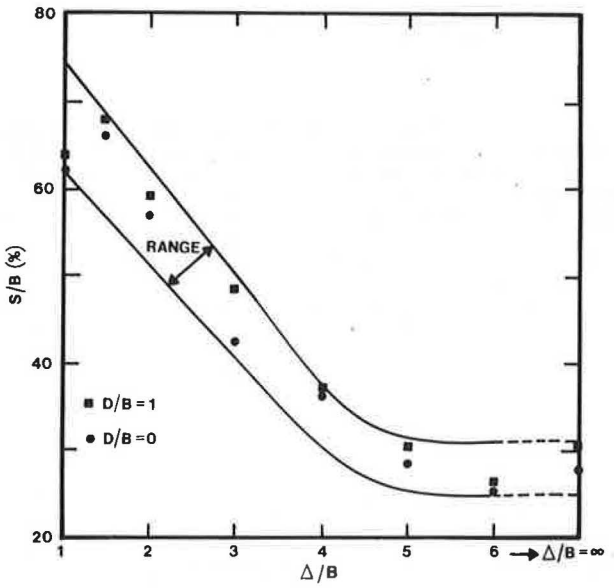

REFERENCES

1. J.G. Stuart. Interference Between Foundation With Special Reference to Surface Footings in Sand. Geotechnique, Vol. 12, No. 1, 1962, pp. 15-22.
2. A.S. Vesic. Analysis of Ultimate Loads on Shallow Foundations. Journal of the Soil Mechanics and Foundations Division, ASCE, Vol. 99, No. SM1, 1973, pp. 45-73.
3. K. Terzaghi. Theoretical Soil Mechanics. Wiley, New York, 1943.
4. A. Caquot and J. Kerisel. Sur le termes de surface dans le calcul des foundations en milieu pulverulent. Proc., Third International Conference on Soil Mechanics and Foundation Engineering, Zurich, Switzerland, Vol. 1, 1953, pp. 336-337.
5. A.S. Vesic. Bearing Capacity of Deep Foundations in Sand. HRB, Highway Research Record 39, 1963, pp. 112-153.
6. J.M. West and J.G. Stuart. Oblique Loading Resulting From Interference Between Surface Footings on Sand. Proc., Sixth International Conference on Soil Mechanics and Foundation Engineering, Montreal, Canada, Vol. 2, 1965, pp. 214-217.

Publication of this paper sponsored by Committee on Foundations of Bridges and Other Structures.

Ultimate Uplift Capacity of Piles in Sand

BRAJA M. DAS AND DAVID B. ROZENDAL

Laboratory model test results for determination of the ultimate uplift capacity of piles embedded in dry sand are presented. In the tests the unit weight of compaction and the embedment ratio were varied. For a given unit of weight of compaction, and thus relative density of compaction and angle of soil friction, unit skin friction increases with depth up to a limiting value. Beyond the critical depth, unit skin friction remains practically constant. The ratio of critical depth of embedment to pile diameter increases with the relative density of compaction. The soil-pile friction angle also increases with relative density of compaction. Based on the results of the model study and a theoretical relation, equations for estimation of the uplift capacity of piles have been suggested. These equations are based on tests conducted on a single pile. More laboratory and field tests are needed to verify the reliability of the equations for design use.

Numerous studies of the compressive load-bearing capacity of piles are available in the literature. A similar problem involving the uplift capacity of piles subjected to tensile load has received much less attention. Pile foundations for structures such as transmission towers and offshore platforms are required to sustain uplifting loads. A limited number of theoretical and experimental studies of the uplift capacity of piles embedded in sand have been reported by Das and Seeley (1), Meyerhof (2,3), Ireland (4), and Esquivel-Diaz (5). Sowa (6) summarizes similar field studies on concrete piles embedded in clay soils. More recently, results of laboratory model studies for determination of the ultimate uplift capacity of wooden piles in saturated clay have been presented by Das and Seeley (7).

A review of the literature previously cited reveals that there are several aspects of the problem that are not yet clearly understood. The purpose of this paper is to review the past theoretical and experimental works and to present some recent laboratory model test results for the ultimate uplift capacity of rough piles in sand.

REVIEW OF PREVIOUS INVESTIGATIONS

Ireland (4) reported the results of six pull-out tests in the field for Raymond step taper piles in sand. Based on the analysis of these results, he proposed an equation for the net ultimate uplift capacity of piles:

$$P_o = K\sigma_v' A_s \tan\phi \quad (1)$$

where

P_o = net ultimate uplift capacity,
K = lateral earth pressure coefficient,
σ_v' = average effective overburden pressure,
A_s = surface area of the pile in contact with sand, and
ϕ = soil angle of friction.

The ultimate uplift capacity (see Figure 1) can be defined as

$$P_u = P_o + W \quad (2)$$

where

P_u = gross ultimate uplift capacity, and
W = effective self-weight of the pile.

The average value of K as recommended by Ireland was approximately 1.75. For piles of length L at depth z with uniform circular cross section (diameter = d) and skin friction f in dry sand (unit weight = γ),

$$\sigma_v' = \gamma L/2$$

$$A_s = \pi dL$$

Thus, the net ultimate capacity is expressed by

$$P_o = (1.75)(\gamma L/2)(\pi dL)\tan\phi = 2.749\,\gamma L^2 d\tan\phi \quad (3)$$

In conjunction with his study of the ultimate uplift capacity of horizontal anchors subjected to oblique loading, Meyerhof (3) proposed the following equation for the net ultimate capacity of rigid piles subjected to vertical uplifting load.

$$P_o = 0.5\,\gamma K_b L^2 d \quad (4)$$

where K_b = uplift coefficient that is a function of the soil-friction angle (ϕ) and the embedment ratio (L/d). The variation of K_b with the soil-friction angle and the embedment ratio (L/d) is shown in Figure 2.

Esquivel-Diaz (5) reported several uplift tests performed in the laboratory. The tests were conducted with model aluminum pipe piles with an outside diameter of 76.2 mm. The outside surface of the piles was roughened by coating with sandpaper. A summary of the results of his tests is given in Table 1.

Figures 3 and 4 show the plots of the ultimate uplift load against embedment ratios as given in Table 1 for dense and loose sand, respectively. For preliminary comparison purposes, Equations 3 and 4

Figure 1. Parameters for ultimate uplift capacity of piles.

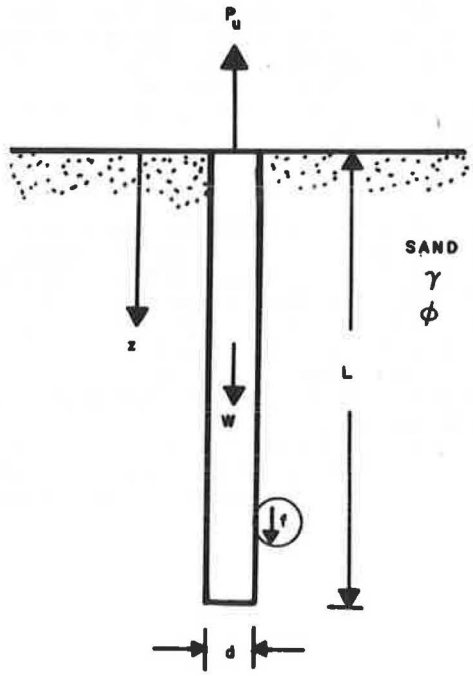

Figure 2. Variation of uplift coefficient, K_b, with soil-friction angle (3).

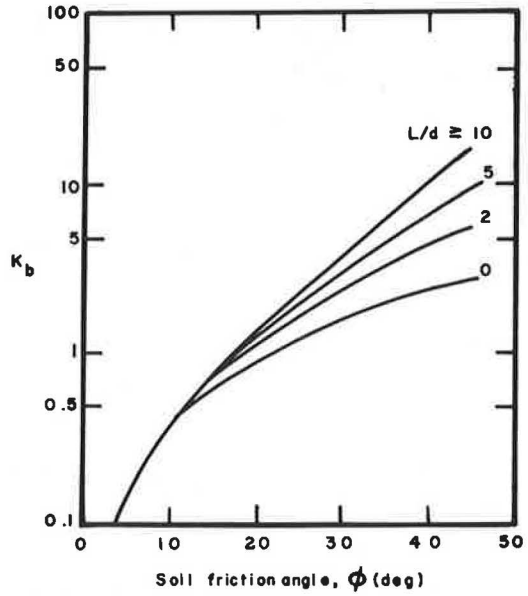

Figure 3. Comparison of test results of Esquivel-Diaz (5) with Equations 3 and 4: dense sand.

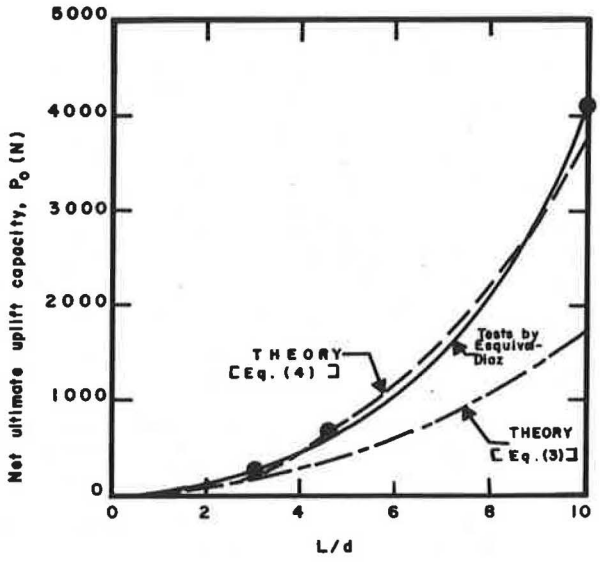

are also plotted in Figures 3 and 4. Based on these plots, the following observations may be made.

1. For dense sand, Equation 3 yields substantially lower values of ultimate load at any given value of L/d.
2. For dense sand, Equation 4--that is, the equation proposed by Meyerhof--gives excellent agreement with the experimental results.
3. For very loose sand, both Equations 3 and 4 yield values of ultimate load that are too high. Note, however, that the equation given by Ireland was developed for steel taper piles made most likely of corrugated steel. The pile tests conducted by Esquivel-Diaz were with straight-shafted steel piles coated with sandpaper.

Another theoretical equation for the ultimate uplift capacity of piles has also been proposed by

Figure 4. Comparison of test results of Esquivel-Diaz (5) with Equations 3 and 4: loose sand.

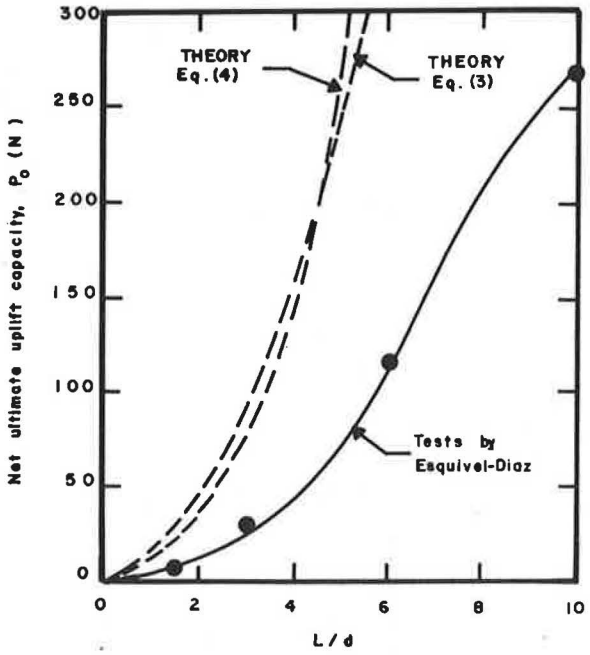

Meyerhof (2). According to this equation, the ultimate capacity can be expressed by

$$P_o = K_u \sigma_v' A_s \tan \delta \quad (5)$$

where

K_u = uplift coefficient, and
δ = angle of friction between the soil and the surface of the pile.

The terms σ_v' and A_s are as defined in Equation 1. For circular piles, Equation 5 takes the form:

$$P_o = K_u(\gamma L/2)(\pi d L) \tan \delta = (\pi/2) K_u \gamma d L^2 \tan \delta \quad (6)$$

The variation of the values of K_u with the soil-friction angles is given in Figure 5. Equation 6 is similar to Equation 1; however, K_u is determined theoretically as compared to the experimental value of K. The angle δ in Equation 6 will depend on several factors, the most important of which are (a) the soil-friction angle, ϕ; (b) the relative density of compaction, D_r; and (c) the roughness of pile surface. This will be discussed later.

Equation 6 essentially is the sum of the frictional resistance developed along the pile surface or

$$P_o = \int_{z=0}^{z=L} (\pi d) f dz \quad (7)$$

where f is the unit skin friction at a depth z. So

$$f = \gamma z K_u \tan \delta \quad (8)$$

LABORATORY MODEL TESTS

Uplift capacity tests in the laboratory were conducted with a wooden pile 25.4 mm in diameter and 0.61 m long. The outside surface of the pile was roughened by applying glue to the pile and then rolling it over the sand used for the tests. The pile was allowed to dry for several days before the tests. Questions might arise about whether gluing might negate the influence of friction between pile and sand, but it is doubtful that this will occur.

Table 1. Laboratory uplift tests on model piles as reported by Esquivel-Diaz (5).

Sand Compaction	Average Unit Weight of Compaction, γ (kN/m^3)	L/d	P_o (N)	Angle of Friction, ϕ (degree)	Approximate Relative Density, D_r (%)
Dense	15.03	3.0	241.97	43	75
		3.0	253.09		
		4.5	698.40		
		4.5	689.40		
		10.0	4,132.20		
Loose	12.81	1.5	5.78	33	13
		3.0	31.14		
		4.5	57.83		
		6.0	117.43		
		10.0	269.55		

Note: Diameter of pile = 76.2 mm.

Figure 5. Variation of K_u with soil-friction angle (2).

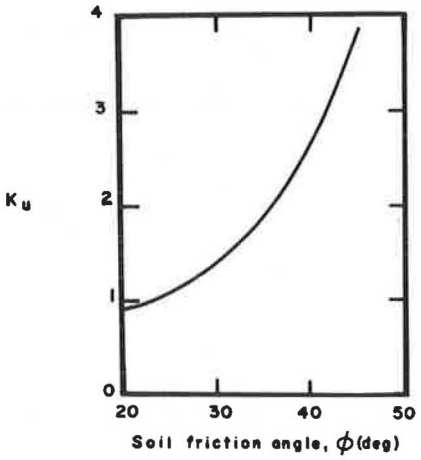

The model tests were conducted in a box measuring 0.61 m x 0.46 m x 0.76 m. A dry silica sand was used for the model tests. The sand had 99 percent passing No. 20 sieve, 55 percent passing No. 40 sieve, and 0 percent passing No. 200 sieve. With the model pile located centrally, the sand was poured into the test box in layers 25.4 to 50.8 mm thick and compacted to the desired unit weights and heights. A steel cable 3.18 mm in diameter was attached to the top of the pile. This cable, in turn, was attached to a lever arm type arrangement. The steel frame that contained the lever arm was attached rigidly to the top of the test box. For some tests in dense sand, the cable was replaced by a steel rod 6.35 mm in diameter. Step loads were applied at the other end of the lever arm and deflection monitored by a dial gauge. The lever arm ratio was 1 to 1.5. Three series of tests were conducted, and the details of the test parameters are given in Table 2.

Table 2. Details of the test parameters.

Series No.	L/d	Unit Weight, γ (kN/m^3)	Relative Density of Compaction, D_r (%)	Triaxial Angle of Friction at Test Density, ϕ (degree)
1	4 to 24	14.81	21.7	31
2	4 to 24	15.79	47.6	34
3	4 to 24	16.88	72.9	40.5

The ultimate uplift load obtained from the laboratory tests is shown in Figures 6 and 7.

ANALYSIS OF TEST RESULTS

The average skin friction that contributes to the resistance against uplift force between depths L = L_1 to L = L_2 can be given by the relation

$$f = [P_{o(L=L_1)} - P_{o(L=L_2)}]/\pi d(L_1 - L_2) \quad (9)$$

The value of skin friction evaluated by Equation 9 may be assumed to be the representative skin friction at a depth $z = (L_1 + L_2)/2$. Using the net uplift capacity from two consecutive tests in a given series, the values of the experimental skin friction for all three series of tests have been evaluated and are shown in Figures 8 and 9. Figure 8 is the plot of the results for test series I and II. The variation of skin friction as calculated from the results of Esquivel-Diaz (5) for the case of loose sand is also plotted. The variation of skin friction of test series III, along with those obtained by Esquivel-Diaz (5) in dense sand, is shown in Figure 9.

From the variation of the skin friction f in Figures 8 and 9, it can be seen that

1. The skin friction, in all cases, increases from zero to a certain critical depth. Beyond the critical depth, skin friction remains almost constant.
2. The nondimensional critical embedment ratio, $(L/d)_{cr}$, increases with the relative density of compaction.
3. For the tests in dense sand made by Esquivel-Diaz, the critical embedment ratio could not be determined because the tests were not extended far enough.

In order to formulate a tentative procedure for the estimation of net ultimate uplift capacity, it was assumed that Equation 8 can be used for $0 \leq L/d \leq (L/d)_{cr}$. Using the proper values of the soil-friction angle and the uplift coefficient given in Figure 5, the values of δ were back-calculated for all experimental test series. The variation of δ/ϕ obtained from these calculations is plotted in Figure 10 with the corresponding relative density of compaction. Note that, in arriving at Figure 10, the theoretical K_u values have been assumed to be correct and the values of δ/ϕ are deduced quantities.

The procedure adopted here for the determination of the approximate critical embedment ratio, $(L/d)_{cr}$,

Figure 6. Net ultimate uplift load for series I and II tests.

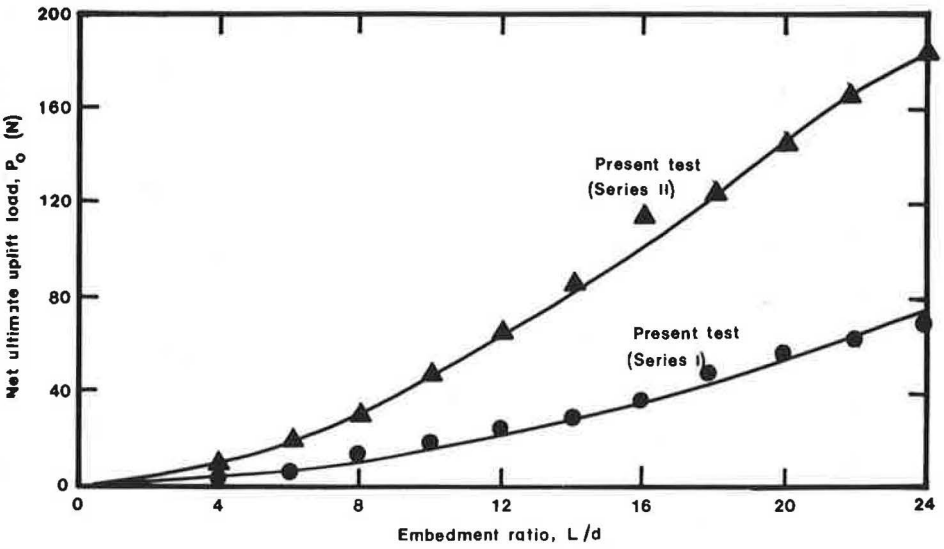

is shown in Figure 11. The critical embedment ratios in Figures 8 and 9 were determined in this manner and are plotted in Figure 10 against corresponding relative densities. From these plots, it appears that an approximate equation can be formulated as

$$(L/d)_{cr} = 0.138D_r + 4.5 \qquad (\text{for } D_r \leq 80\%) \tag{10}$$

TENTATIVE PROCEDURE FOR ESTIMATION OF UPLIFT CAPACITY

Based on the observations made during the model tests, it appears that the uplift capacity of the model piles can be reasonably estimated by the following steps for $D_r \leq 80$ percent.

1. Estimation of the critical embedment ratio using Equation 10.
2. For $L \leq L_{cr}$

$$P_o = \int_0^L (\pi d)(\gamma z K_u \tan\delta)dz = \tfrac{1}{2}\pi d\gamma L^2 K_u \tan\delta \tag{11}$$

The values of K_u and δ can be obtained from Figures 5 and 10.

3. If $L > L_{cr}$ (Figure 11),

$$P_o = \int_0^L (\pi d)fdz = \int_0^{L_{cr}} \pi d(\gamma z K_u \tan\delta)dz + \pi d\gamma L_{cr} K_u \tan\delta\,(L - L_{cr})$$

$$= \tfrac{1}{2}\pi d\gamma L_{cr}^2 K_u \tan\delta + \pi d\gamma L_{cr} K_u \tan\delta\,(L - L_{cr}) \tag{12}$$

APPLICATION TO FIELD CONDITIONS

The results are interesting; however, the uplift capacity estimation procedure given in Equations 11 and 12 is based only on this model test. Therefore, it is not recommended for immediate use in the field because

1. The depth beyond which the unit skin friction remains constant is highly dependent on the critical embedment ratio. The estimation given in Figure 10 is based only on tests conducted for a pile of a single diameter. Results of future investigations should be compared with the present findings. Future tests should be conducted in both the field and the laboratory.
2. The method used to place sand in the present tests differs from that used in the field. This may affect the values of $(L/d)_{cr}$ and δ. Without sufficient large-scale field test results, the problem cannot be confidently resolved.

Questions may also arise when piles are driven below the groundwater table. For example, the surface tension effect may tend to increase the gross ultimate uplift capacity. However, in our opinion, this should not be taken into account because it is unpredictable.

CONCLUSIONS

Laboratory model test results for determination of the ultimate uplift capacity of piles in sand have been presented. Based on these results, the following conclusions can be drawn.

1. The unit skin friction, f, between the soil and the piles increases in an approximately linear manner up to a critical depth. Beyond the critical depth, the unit skin friction remains practically constant.
2. The critical embedment ratio, $(L/d)_{cr}$, as determined from these tests, increases with relative density of compaction up to about 1.5 for $D_r \leq 80$ percent.
3. Based on the limited test results, equations for the prediction of ultimate uplift capacity have been developed. Before they are applied to field design problems, these equations may need to be modified to reflect the results of additional field and laboratory tests.

REFERENCES

1. B.M. Das and G.R. Seeley. Uplift Capacity of Buried Model Piles in Sand. Journal of the Geotechnical Engineering Division, ASCE, Vol. 101, No. GT10, 1975, pp. 1091-1094.
2. G.G. Meyerhof. Uplift Resistance of Inclined Anchors and Piles. Proc., 8th International Conference on Soil Mechanics and Foundation Engineering, Vol. 2, Moscow, 1973, pp. 167-172.
3. G.G. Meyerhof. The Uplift Capacity of Foundations Under Oblique Loads. Canadian Geotechnical Journal, Vol. 10, No. 1, 1973, pp. 64-70.
4. H.O. Ireland. Pulling Tests on Piles in Sand. Proc., 4th International Conference on Soil

Figure 7. Net ultimate uplift load for series III tests.

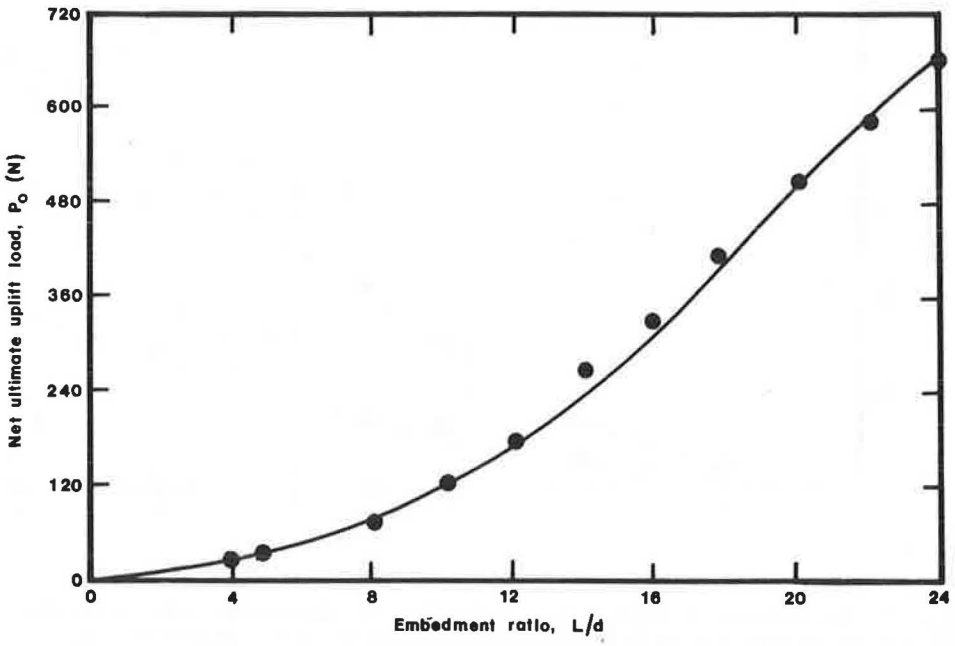

Figure 8. Variation of unit skin friction of test series I and II.

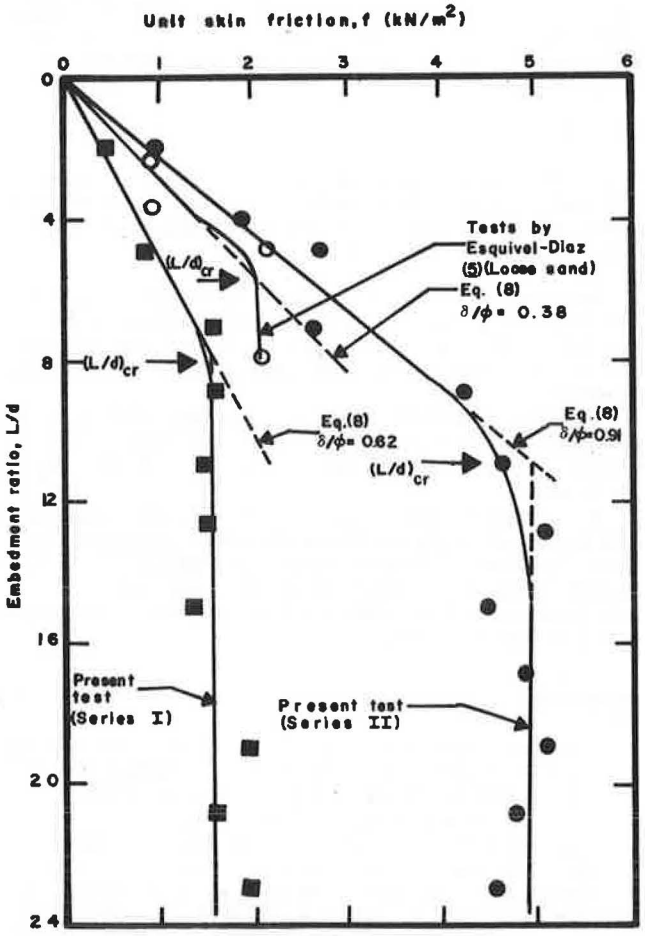

Figure 9. Variation of unit skin friction of test series III.

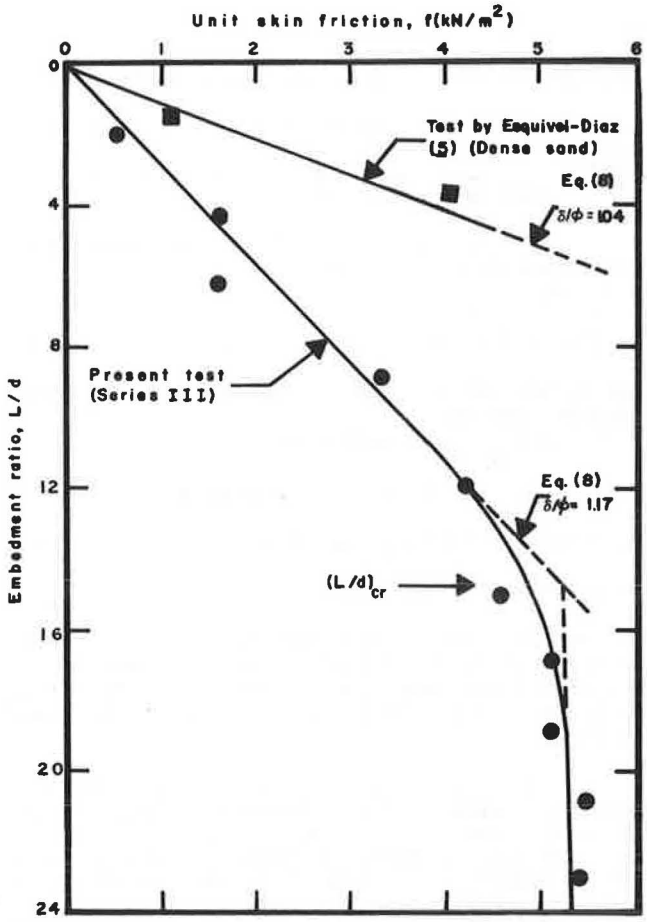

Figure 10. Plot of δ/ϕ and $(L/d)_{cr}$ against relative density of compaction.

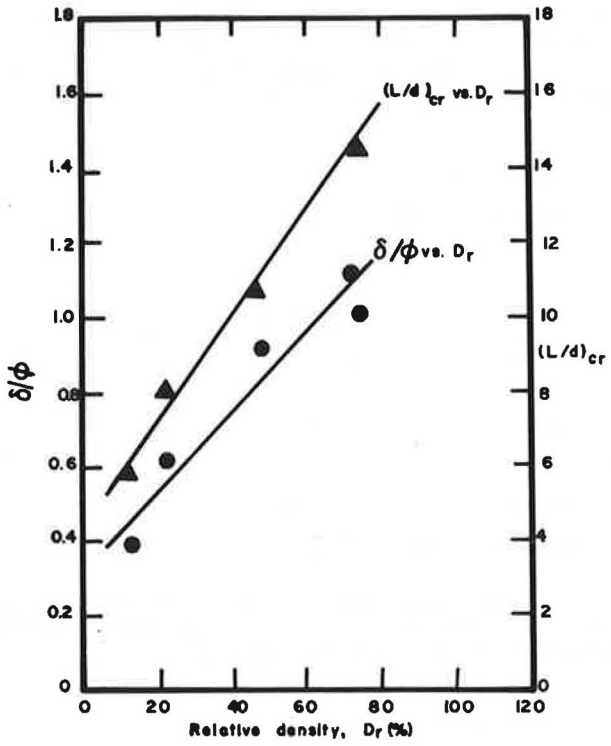

Figure 11. Procedure for determining critical embedment ratio.

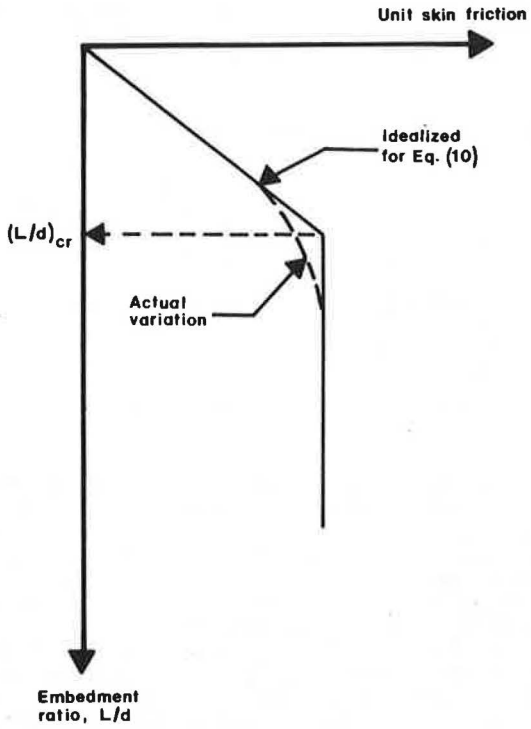

Mechanics and Foundation Engineering, Vol. 2, London, 1975, pp. 43-46.

5. R.F. Esquivel-Diaz. Pullout Resistance of Deeply Buried Anchors in Sand. M.S. thesis, Duke University, Durham, N.C., 1967.
6. V.A. Sowa. Pulling Capacity of Concrete Cast In Situ Bored Piles. Canadian Geotechnical Journal, Vol. 7, 1970, pp. 482-493.
7. B.M. Das and G.R. Seeley. Uplift Capacity of Pipe Piles in Saturated Clay. Soils and Foundations, The Japanese Society of Soil Mechanics and Foundation Engineering, Vol. 22, No. 1, 1982, pp. 91-94.

Publication of this paper sponsored by Committee on Foundations of Bridges and Other Structures.

Analysis of a Spiling Reinforcement System in Soft-Ground Tunneling

S. BANG

An investigation of a spiling reinforcement system used for stabilizing tunnels is presented. The system is composed of a series of radially installed reinforcing spiles placed around the perimeter of the tunnel heading before excavation. This system provides immediate stabilization of an opening as well as permanent stabilization. It has been successfully used for tunneling in weak rock formations and, to a lesser extent, in soft grounds. To date, no rational design methodology has been formulated because no reasonable analytic method of analysis has been suggested. A generalized plane strain composite finite-element analysis, which uses the proper simulation of the excavation and reinforcement to calculate three-dimensional stresses and displacements while the finite-element grid remains in two dimensions, is presented. The effects of the reinforcement, the inclination, and the spacing of the spiles on the performance of the system have been analyzed with the proposed method. The ground surface movements are used to calculate the vertical and horizontal distortions that are directly related to damage to buildings located above the tunnel.

A spiling reinforcement system has been successfully used in tunneling to strengthen weak rock formations as well as other soft grounds (1). The system typically consists of a series of radially installed 15- to 20-ft reinforcing spiles spaced from 2.5 to 5 ft with an inclination angle of approximately 30

degrees to the tunnel axis. The reinforcing spiles are formed by inserting rebars 1 to 1.5 in. in diameter in predrilled holes with subsequent grout. Figure 1 shows a schematic representation of the system. The general principle is to stabilize a

Figure 1. Spiling reinforcement ahead of the face.

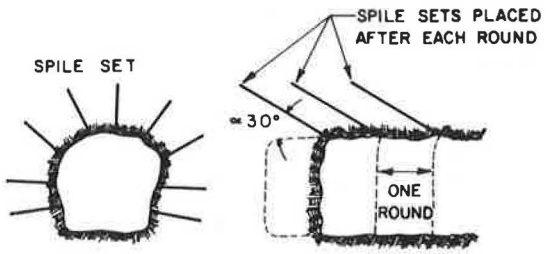

weak mass by installing an annular spiling reinforcement network along the perimeter of the tunnel heading before excavation. The reinforcing network is extended into the in situ ground both radially and longitudinally; therefore, the tunneling operation is always performed inside a tubular reinforced zone encircling the tunnel opening.

It has been reported (1) that the use of this scheme helps control both the immediate stabilization of an opening by preventing loosening and the permanent stabilization by restricting deformations. To date, a rational design methodology has not been formulated nor has a reasonable analysis procedure been offered. A method of analysis together with results obtained from the analysis for a spiling reinforcement system in soft-ground tunneling are presented here.

METHOD OF ANALYSIS

In formulating a method of analysis, it is important to take into consideration the tunnel excavation process and the soil-reinforcement composite behavior. These factors, which greatly influence the performance of the spiling reinforcement system, favor the use of finite-element analysis.

A generalized plane strain finite-element method has been developed to investigate the detailed behavior of the spiling reinforcement system. The generalized plan strain condition assumes three nonzero displacement components, none of which is dependent on the out-of-plane coordinate; thus the out-of-plane strain remains zero, and the displacement does not remain zero, which is commonly the case in the conventional plane strain approach. This approach was chosen because the conventional plane strain approach cannot effectively capture the out-of-plane behavior of the inclined spiling reinforcement, and a full three-dimensional analysis may be prohibitively expensive and time consuming. The main advantage of the generalized plane strain approach is that it calculates three-dimensional stresses and displacements while the finite-element grid remains in two dimensions. A brief description of the element stiffness matrix formulaton in a generalized plane strain condition follows.

The total virtual work is defined as

$$\delta V = \sum_{e=1}^{N} \delta V_e = \sum_{e=1}^{N} (\delta U_e - \delta W_e) = 0 \tag{1}$$

where N is the number of elements and δU_e and δW_e are the element virtual internal energy and external work, respectively. With an incremental material law,

$$\Delta \underset{\sim}{\sigma} = \underset{\sim}{C}\, \Delta \underset{\sim}{\epsilon} \tag{2}$$

where $\Delta\underset{\sim}{\sigma}$ and $\Delta\underset{\sim}{\epsilon}$ are vectors of small changes in stresses and strains and the constitutive matrix $\underset{\sim}{C}$ is dependent on current stress state and history, the element virtual internal work is written incrementally as

$$\delta \Delta U_e = \int_{V_e} \delta \underset{\sim}{\epsilon}^T \Delta \underset{\sim}{\sigma}\, dV_e \tag{3}$$

Using the incremental constitutive law, one can write

$$\delta \Delta U_e = \int_{V_e} \delta \underset{\sim}{\epsilon}^T \underset{\sim}{C}\, \Delta \underset{\sim}{\epsilon}\, dV_e \tag{4}$$

Because the displacement components in generalized plane strain are independent of the coordinate in the out-of-plane direction, z, i.e.,

$$\begin{aligned} u &= u(x,y) \\ v &= v(x,y) \\ w &= w(x,y) \end{aligned} \tag{5}$$

the strain components become

$$\underset{\sim}{\epsilon} = \left\{ \partial u/\partial x,\ \partial v/\partial y,\ 0,\ \partial u/\partial y + \partial v/\partial x,\ \partial w/\partial x,\ \partial w/\partial y \right\}^T \tag{6}$$

Using linear approximation of displacements, the three displacements at each node of the quadrilateral element can be approximated as

$$\begin{aligned} u &= \sum_{i=1}^{4} N_i u_i \\ v &= \sum_{i=1}^{4} N_i v_i \\ w &= \sum_{i=1}^{4} N_i w_i \end{aligned} \tag{7}$$

where u_i, v_i, and w_i are approximate nodal displacements and N_i is the first-order shape function.

From Equations 6 and 7 the strain component along x direction can be calculated as

$$\epsilon_x = \partial u/\partial x = (\partial/\partial x)\left(\sum_{i=1}^{4} N_i u_i \right) = \sum_{i=1}^{4} F_i u_i \tag{8}$$

where $F_i = \partial N_i/\partial x$.

Similarly, one can obtain

$$\begin{aligned} \epsilon_y &= \sum_{i=1}^{4} G_i v_i \\ \gamma xy &= \sum_{i=1}^{4} (G_i u_i + F_i v_i) \\ \gamma xz &= \sum_{i=1}^{4} F_i w_i \\ \gamma yz &= \sum_{i=1}^{4} G_i w_i \end{aligned} \tag{9}$$

where $G_i = \partial N_i/\partial y$.

The strain-displacement relationships can be written as

$$\Delta \underset{\sim}{\epsilon}_e = \underset{\sim}{B}\, \Delta \underset{\sim}{u}_e \tag{10}$$

where $\Delta\underset{\sim}{u}_e$ is vector of nodal displacement increments.

Equation 4 can then be rewritten as

$$\begin{aligned} \delta \Delta U_e &= \int_{V_e} [(\underset{\sim}{B}\delta \underset{\sim}{u}_e)^T \underset{\sim}{C} (\underset{\sim}{B} \Delta \underset{\sim}{u}_e)]\, dV_e \\ &= \delta \underset{\sim}{u}_e^T \underset{\sim}{K}\, \Delta \underset{\sim}{u}_e \end{aligned} \tag{11}$$

where the element tangent stiffness matrix $\underset{\sim}{K}$ is expressed as

$$\underset{\sim}{K} = \int_{V_e} \underset{\sim}{B}^T \underset{\sim}{C} \underset{\sim}{B}\, dV_e \tag{12}$$

Here

$$\underset{\sim}{B} = \begin{bmatrix} \underset{\sim}{F}^T & \underset{\sim}{0}^T & \underset{\sim}{0}^T \\ \underset{\sim}{0}^T & \underset{\sim}{G}^T & \underset{\sim}{0}^T \\ \underset{\sim}{0}^T & \underset{\sim}{0}^T & \underset{\sim}{0}^T \\ \underset{\sim}{G}^T & \underset{\sim}{F}^T & \underset{\sim}{0}^T \\ \underset{\sim}{0}^T & \underset{\sim}{0}^T & \underset{\sim}{F}^T \\ \underset{\sim}{0}^T & \underset{\sim}{0}^T & \underset{\sim}{G}^T \end{bmatrix} \tag{13}$$

where $\underset{\sim}{F}^T = \{F_1, F_2, F_3, F_4\}$ and $\underset{\sim}{G}^T = \{G_1, G_2, G_3, G_4\}$. Thus a 12 x 12 element tangent stiffness matrix can be obtained.

COMPOSITE ELEMENT

The composite representation of the reinforced system used in this analysis is an expansion of the approach developed by Romstad et al. (2), which expresses the orthotropic composite material properties as functions of the properties of each of the constituent materials (i.e., the soil mass, the reinforcing members, and their geometric arrangement).

This approach is based on the concept of the unit cell, an isolated small unit of the material that completely exhibits its composite characteristics. The average values of the stresses distributed over the cell faces are equal to the stresses in the equivalent composite material, and the average values of strains for the cell are those of the composite. Thus the average response of the unit cell to a homogeneous state of composite stress or strain is the same as the composite response of the material. Therefore, the desired composite properties may be calculated from detailed consideration of the behavior of the unit cell. These composite properties may then be used in the analysis of the complete structure. Such as analysis yields the composite stress and strain throughout the structure. Once the composite stress state is determined at a particular point in the structure, the corresponding constituent stress state (e.g., soil or spile) may be determined by returning to the analysis of the unit cell.

A schematic representation of the unit cell is shown in Figure 2. The composite material consists of a soil reinforced with spiles parallel to one another at a chosen spacing, S, and extending deep into the soil mass. The 1-axis in Figure 2 is chosen parallel to the spile and the 2- and 3-axes form a plane perpendicular to the longitudinal axis of the spile, where the 2-axis passes through the center of the tunnel. For a given reinforcing pattern, all spiles in a given 1-2 plane are assumed to be equally spaced.

Figure 2. Unit cell.

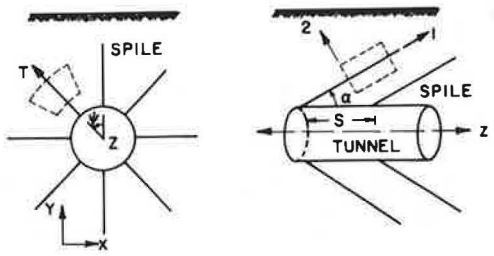

The basic composite properties defining the stress-strain relationship were calculated by Romstad et al. (2) by successively considering a number of simple composite stress-strain states and approximately determining the response of the unit cell. The constitutive relationship in global coordinates can be obtained by considering two successive general two-dimensional axes rotations described by Mohr's circle relations (see Figure 3).

SHOTCRETE LINING

To prevent soil fall-out, a thin shotcrete lining may be used immediately after excavation and before installation of a permanent lining. The shotcrete lining was considered to be a flexible membrane element with no bending stiffness. Figure 4 shows a general membrane element with a thickness, t. This approach was chosen because the shotcrete lining is relatively thin and no separate representation of the lining in the finite-element grid is necessary in this approach. The resulting stiffness matrix of the membrane element can be added directly to that of the soil element adjacent to the lining.

Figure 3. Coordinate transformation of unit cell.

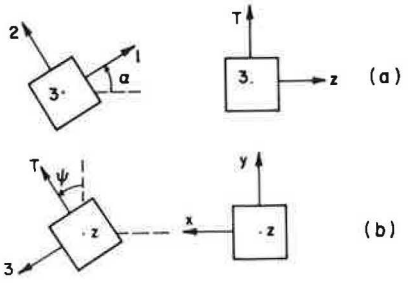

Figure 4. Membrane element representation.

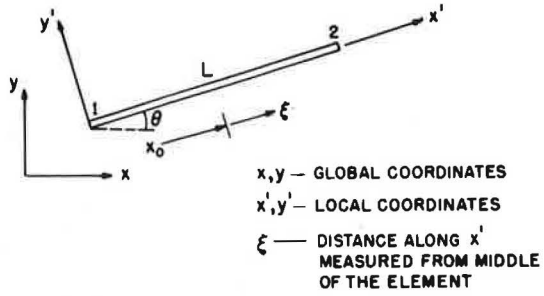

Assuming $\sigma y'$, $\tau x'y'$, and $\tau y'z'$ are zero, the stress-strain relationship reduces to

$$\begin{bmatrix} \sigma_{x'} \\ \sigma_{z'} \\ \tau_{x'z'} \end{bmatrix} = \begin{bmatrix} C_{11} & C_{12} & 0 \\ C_{12} & C_{22} & 0 \\ 0 & 0 & C_{33} \end{bmatrix} \begin{bmatrix} \epsilon_{x'} \\ \epsilon_{z'} \\ \gamma_{x'z'} \end{bmatrix} \tag{14}$$

Taking the x' and z' displacements at any point as u' and w', respectively,

$$\epsilon_{x'} = \partial u'/\partial x'$$

$$\epsilon_{z'} = \partial w'/\partial z' = 0$$

$$\gamma_{x'z'} = (\partial u'/\partial z') + (\partial w'/\partial x') = \partial w'/\partial x' \tag{15}$$

are obtained. Note that the generalized plane strain condition is applied.

Because $x' = x_o + \xi(\ell/2)$ (from Figure 4),

$$\partial/\partial x' = (\partial/\partial\xi)(\partial\xi/\partial x') = (2/\ell)(\partial/\partial\xi) \quad (16)$$

Also

$$u' = [(1/2)\, u_1'(1 - \xi)] + [(1/2)\, u_2'(1 + \xi)]$$
$$= (1/2)\, [(u_2' + u_1') + \xi(u_2' - u_1')]$$

$$w' = (1/2)\, [(w_2' + w_1') + \xi(w_2' - w_1')] \quad (17)$$

The nodal displacements are expressed as

$$u_i' = u_i \cos\theta + v_i \sin\theta$$
$$v_i' = -u_i \sin\theta + v_i \cos\theta$$
$$w_i' = w_i \quad (18)$$

for i = 1, 2, where u, v, and w are the nodal displacements with respect to the x, y, and z coordinates. Substituting Equations 15 into the element virtual internal work expression, the following element stiffness matrix is obtained.

$$\underset{\sim}{K} = \begin{bmatrix} S_{11} & S_{12} & 0 & -S_{11} & -S_{12} & 0 \\ S_{12} & S_{22} & 0 & -S_{12} & -S_{22} & 0 \\ 0 & 0 & S_{33} & 0 & 0 & -S_{33} \\ -S_{11} & -S_{12} & 0 & S_{11} & S_{12} & 0 \\ -S_{12} & -S_{22} & 0 & S_{12} & S_{22} & 0 \\ 0 & 0 & -S_{33} & 0 & 0 & S_{33} \end{bmatrix} \quad (19)$$

where

$$S_{11} = (t/\ell)\, C_{11} \cos^2\theta$$
$$S_{12} = (t/\ell)\, C_{11} \cos\theta \sin\theta$$
$$S_{22} = (t/\ell)\, C_{11} \sin^2\theta$$

and

$$S_{33} = (t/\ell)\, C_{33}$$

INCREMENTAL ITERATIVE PROCEDURE

A finite-element computer program incorporating the previously mentioned features was developed. The construction and excavation process was simulated by a two-step incremental procedure. The first increment computes the initial stress state of the whole soil mass simulating in situ soil condition. This increment results in the development of stresses only (i.e., displacements are reset to zero). The second increment handles installing the spiles and excavating the tunnel as well as the construction of the shotcrete lining.

Within each increment, the nonlinear soil properties are accounted for by an iterative solution procedure using a nonlinear soil model developed by Duncan and Wong (3). This model assumes that the soil does not experience any stress- or strain-induced anisotropy (i.e., soil behavior is described by the instantaneous value of Young's modulus dependent on the stress state). A hyperbola is assumed to represent the stress-strain relationship for primary loading, and a straight line is assumed for unloading and reloading. A constant Poisson's ratio of 0.3 was used because the expressions for initial and tangent Poisson's ratio do not include the effect of unloading.

To improve the rate of convergence in the iteration process, a modified estimate of the soil modulus was used. For iteration n this value was expressed in terms of the calculated modulus and the modulus from the previous iteration, n - 1. That is,

$$E^{*(n)} = rE^{(n)} + (1 - r)E^{(n-1)} \quad (20)$$

where r is a relaxation factor. Because the convergence was oscillatory, a study was conducted to obtain the factor that gives the minimum number of iterations to be solved in the finite-element analysis. A factor of 0.7 was found. Using this underrelaxation factor, the solution usually converged within 4 to 8 iterations for each increment.

RESULTS

To understand the spiling reinforcement system in soft-ground tunneling, an investigation has been performed using the developed computer program. The investigation was limited to the study of a horizontal, single, circular tunnel with all spiles having the same axial and circumferential spacing and the same inclination angle along the entire circumference of the tunnel. Figure 5 shows the typical finite-element grid used in the study. The pertinent soil properties adopted in the study are given in Table 1.

Figure 5. Typical finite-element grid.

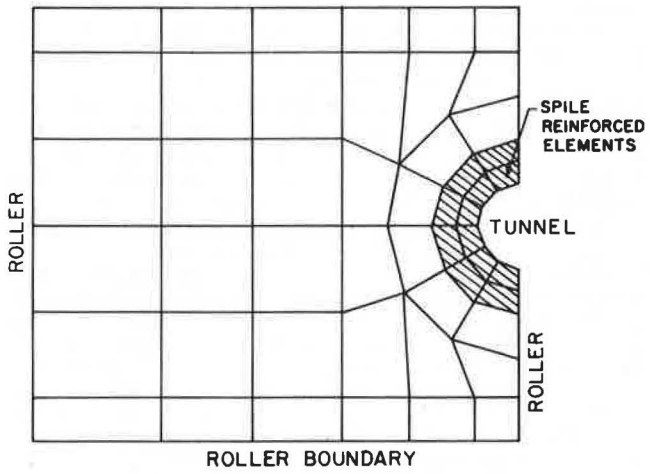

Table 1. Pertinent soil properties (4).

	Soils		
	No. 1 (SM[a])	No. 2 (CL[b])	No. 3 (CL[b])
Loading modulus	200	120	60
Unloading modulus	330	198	153
Modulus exponent	0.6	0.45	0.45
Failure ratio	0.7	0.7	0.7
Cohesion (psi)	2.778	2.083	0.694
Friction angle (°)	33	30	30
Poisson's ratio	0.3	0.3	0.3

[a]SM is silty sand.
[b]CL is clay with low plasticity.

The main variables considered were the depth of the tunnel center (H), the spacing (S), and the inclination of the spiles (α). Both the diameter of the tunnel and the length of the spiles remained constant at 20 ft. These values were chosen because the diameters of the tunnels used in Washington, D.C., Metro; Frankfurt; Sao Paulo; and San Francisco

were in the range of 18 to 21 ft (4) and, for the soil region farther than one radius from the opening, any increase in strength related to the presence of the reinforcement is small (5). (Note that spiles equal in length to the diameter of the tunnel with 30 degree inclination form a reinforced zone one radius from the tunnel opening.) The reinforcing spiles consisted of 1-in.-diameter rebars in 4-in. predrilled holes filled with grout. A brief description of the results obtained from the analysis follows.

Generally, there is a dramatic reduction in deformations when the spiling reinforcement system is used. Figure 6 shows a comparison of the tunnel deformations for unreinforced and reinforced tunnels. Quantitative comparisons of the deformation are given in Table 2. It is obvious that the use of spiling reinforcement reduces the crown and bottom movements of the tunnel by approximately 87 percent and 48 percent, respectively. A similar reduction in vertical ground surface movements is shown in Figure 7. The reduction may be as great as 90 percent of the unreinforced case.

To evaluate the stability of structures located above or adjacent to the tunnel, vertical and horizontal distortions were calculated and compared. The vertical distortion is defined as the differential vertical movement between two points divided by the distance separating them. The horizontal distortion is defined in a similar manner for the differential horizontal movement. These parameters have been used to describe the possible damage potential of various types of structures (6-10). Figure 8 shows the distribution of the vertical distortions for unreinforced and reinforced tunnels. Maximum vertical distortion of 1.25 percent results for the unreinforced tunnel, whereas only 0.12 percent is observed for the reinforced tunnel--a 90 percent reduction. According to Bjerrum (11), cracking in panel walls is to be expected if vertical distortion exceeds 0.33 percent. Similar reductions are observed in maximum horizontal distortions (i.e., 0.79 percent and 0.065 percent, respectively). According to O'Rourke et al. (12), 0.3 percent is the threshold value of horizontal distortion causing architectural damage in buildings.

The relative significance of the spile inclination angle to the performance of the system can be seen in Figure 9, which shows the resulting deformation of the tunnel due to different angles of spile inclination. Note that different scales are used for the tunnel and the displacement. An angle of spile inclination of approximately 30 degrees to the tunnel axis produces the least movement at the crown, the bottom, and the side of the tunnel. This finding can be further confirmed by comparing the ground surface distortions. The results indicate that an inclination angle of 30 degrees produces approximtely 30 percent less vertical distortion than an inclination angle of 40 degrees and approximately 5 percent less than an inclination angle of 20 degrees.

The effect of the spile spacing, a measure of the reinforcing intensity, has also been studied. A summary of the tunnel deformations obtained with different spile spacings is given in Table 3. The reduction in crown movement is much larger than the reduction in bottom movement, and the rate of improvement increases as spile spacing is reduced. The effect of spile spacing is even more pronounced in reducing the ground surface settlement. For in-

Figure 6. Deformation of the tunnel.

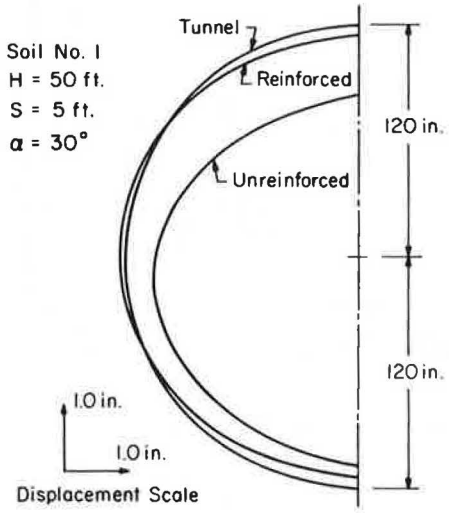

Figure 7. Vertical ground surface movement.

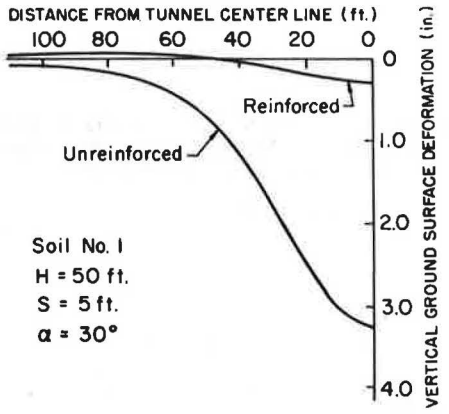

Table 2. Reduction of tunnel deformation spiling reinforcement in soil No. 1 (H = 50 ft).

	Unreinforced (in.)	Reinforced (in.)	Reduction (%)
Crown	-4.439	-0.5734	87
Bottom	1.4	0.7214	48

Figure 8. Vertical ground surface distortion.

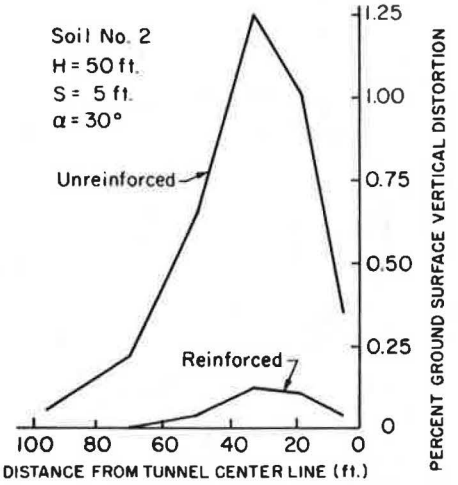

stance a reduction of 34 percent in surface settlement above the tunnel center can be achieved by reducing spile spacing from 4 ft to 2 ft, whereas approximately 29 percent and 6 percent reduction in crown and bottom movements are expected. Generally, the effect of spile spacing on the performance of the system, including tunnel deformations and ground surface movements, is much greater in weaker soils. Even though the effect of spile spacing is smaller in stronger soils, the reinforcing effect is still remarkable when the behavior of the reinforced system is compared with that of the unreinforced system.

The location of the potential failure surface was estimated by observing the variation of the maximum shear strains obtained from three-dimensional strains. A typical maximum shear strain distribution is depicted by the contours in Figure 10. The potential failure surface was approximated by connecting the highest maximum shear strain points. This indicates that the potential failure surface passes more or less through the side of the tunnel and propagates upward forming a circlelike curved surface as shown in Figure 10. The potential failure surface may be approximated in the design of the system by a series of straight lines or a continuous curve.

CONCLUSION

An investigation of a spiling reinforcement system used in soft-ground tunneling is described. A generalized plane strain finite-element analysis has been developed to calculate the three-dimensional stresses and displacements while the finite-element grid remains in two dimensions. From the information obtained from the analysis, effects of the reinforcement, the inclination, and the spacing of the spiles on the performance of the system have been discussed and quantified.

The developed method of analysis can be used for the calculation of tunnel and ground surface movements under various field conditions (e.g., soil type, tunnel depth, inclination and spacing of the spiles, and tunnel diameter). The results can then be used for the design of the spiling reinforcement system. An appropriate spile spacing can be chosen from the results to ensure that the deformation characteristics of the system can be kept within acceptable bounds. Because the method of analysis produces three-dimensional displacements, the out-of-plane direction displacement can be included in the calculation of the ground surface distortions. Figure 11 is an example that indicates the variation

Figure 9. Tunnel deformation for different spile inclinations.

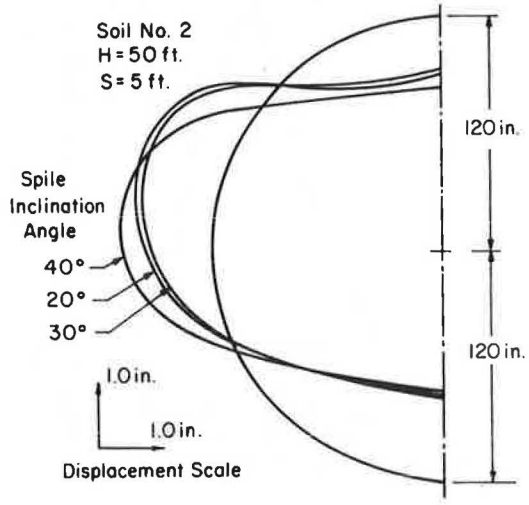

Figure 10. Contours of maximum shear strain.

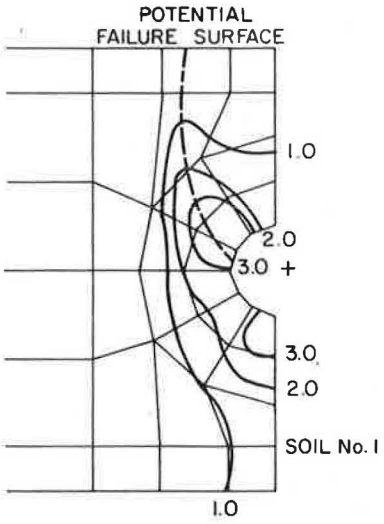

Figure 11. Variation of ground angular distortion.

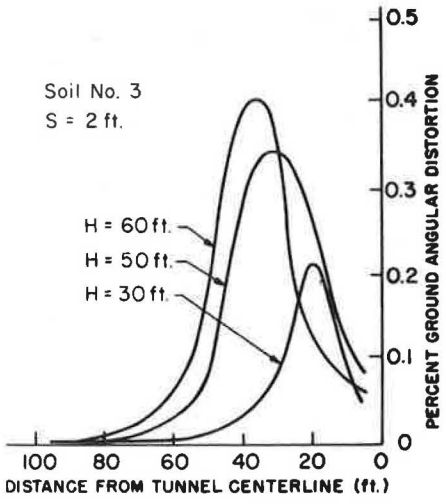

Table 3. Tunnel deformation with different spile spacings in soil No. 3 (H = 50 ft).

Spile Spacing (ft)	Crown (in.)	Bottom (in.)
5	-2.37	1.78
4	-2.29	1.76
3	-2.19	1.74
2	-1.65	1.65

of ground surface angular distortion, a measure of combined vertical distortion in three dimensions. Angular distortion can be obtained from

$$\text{Angular distortion} = (1/L)(\Delta\delta_y^2 + \Delta\delta_z^2)^{1/2} \quad (21)$$

where

L = distance between nodes,
$\Delta\delta_y$ = differential vertical displacement, and
$\Delta\delta_z$ = differential out-of-plane displacement.

The developed method of analysis was intended to capture the most essential characteristics involved in the spiling reinforcement system in soft-ground tunneling without resorting to three-dimensional grids. However, the validity of the developed method of analysis remains to be tested. Further research should be done in areas such as field instrumentation and monitoring of prototype systems or large-scale centrifuge model testing. In this way the validity and effectiveness of the developed analytic methods can be checked and extended.

ACKNOWLEDGMENTS

The work presented in this paper is based on research supported by the U.S. Department of Transportation under contract No. DTRS-5681-C-00024. The author is extremely grateful for this support.

REFERENCES

1. G.E. Korbin and T.L. Brekke. Field Study of Tunnel Prereinforcement. Journal of Geotechnical Engineering Division, ASCE, Vol. 104, No. GT8, 1978.
2. K.M. Romstad, L.R. Herrmann, and C.K. Shen. Integrated Study of Reinforced Earth-I: Theoretical Formulation. Journal of Geotechnical Engineering Division, ASCE, Vol. 102, No. GT5, 1976.
3. J.M. Duncan and K.S. Wong. Hyperbolic Stress-Strain Parameters for Non-Linear Finite Element Analysis of Stress and Movements in Soil Masses. University of California, Berkeley, Rept. TE-74-3, 1970.
4. E.J. Cording and W.H. Hansmire. Displacements Around Soft Ground Tunnels. 5th Panamerican Congress on SM & FE, Session IV, General Rept., Buenos Aires, Nov. 1975.
5. G.E. Korbin and T.L. Brekke. Model Study of Tunnel Prereinforcement. Journal of Geotechnical Engineering Division, ASCE, Vol. 102, No. GT9, 1976.
6. J.B. Burland and C.P. Wroth. Settlement of Buildings and Associated Damage. Proc., Conference on Settlement of Structures, 1975.
7. R. Grant, J.T. Christian, and E.H. Vanmarcke. Differential Settlement of Buildings. Journal of Geotechnical Engineering Division, ASCE, Vol. 100, No. GT9, 1974.
8. J. Kreisel. Fifteenth Ranken Lecture: Old Structure in Relation to Soil Conditions. Geotechnique, Vol. 25, No. 3, 1975.
9. D.E. Polshin and R.A. Tokar. Maximum Allowable Non-Uniform Settlement of Structures. Proc., 4th International Conference on SM & FE, Vol. 1, 1957.
10. A.W. Skempton and D.H. MacDonald. Allowable Settlement of Buildings. Proc., Institution of Civil Engineers, Part 3, Vol. 5, 1956.
11. L. Bjerrum. Discussion. Proc., European Conference on Soil Mechanics and Foundation Engineering, Vol. II, Wiesbaden, 1963.
12. T.D. O'Rourke, E.J. Cording, and M. Boscardin. The Ground Movements Related to Braced Excavation and Their Influence on Adjacent Buildings. U.S. Department of Transportation, Rept. DOT-TST-76T-23, Aug. 1976.

Publication of this paper sponsored by Committee Subsurface Soil-Structure Interaction.

Compactive Prestress Effects in Clays

ALBERT DiBERNARDO AND C.W. LOVELL

The load-deformation behavior of natural clays is strongly influenced by the geologic maximum past pressure. If such clays are excavated and manipulated before compaction, the geologic effect is largely lost. However, the compaction process establishes a new prestress value, and the ratio of this prestress to the effective normal stress in a compacted fill forms a new overconsolidation ratio (OCR). If the material and compactive prestress values are held constant in a moderately high embankment, the OCR values range from quite high at lesser depths to unity in lower embankment locations. Consequently, the nature of the shearing and compressibility responses varies considerably with position in the embankment. Laboratory studies have been conducted on both compacted shales and clays to demonstrate the empirical prediction of the prestress value and its relative effect on saturated compressibility and undrained shear behavior. The prestress varies with the nominal compaction pressure and its rate of application, as well as with the material and its water content. This value is predicted from the conventional oedometer test on the as-compacted material. When the compacted materials are soaked at a variety of confining pressures, which simulate differing embankment positions, the volume changes are highly dependent on the major compaction variables and the prestress. To achieve a homogeneous and predictable load-deformation response in major embankments, it is necessary to better understand and control the prestress effected by compaction. The research discussed here was conducted to examine the compressibility behavior of a laboratory-compacted soil in the as-compacted and soaked condition. A highly plastic residual clay and a kneading type of compaction were used. To determine the as-compacted compressibility characteristics, the compacted samples were trimmed to appropriate size and incrementally loaded in the oedometer. Of particular interest was the value of compactive prestress.

Early hypotheses concerning compaction of fine-grained soils explained the compaction process in terms of a predominant influence of individual clay particles (or clusters). More recently, the role of agglomerations or peds of clay particles has been emphasized.

BACKGROUND

Compaction Hypotheses

Barden and Sides (1) attempted to relate the engineering behavior of compacted clay to its fabric. Photomicrographs of the fabric of two clays revealed that the main difference between samples compacted

at different moisture contents was at the larger size levels. Observations revealed an apparently homogeneous fabric wet of optimum and 3-mm to 6-mm diameter pelletlike macropeds dry of optimum. These findings led to the following general analysis of the compaction process.

"At low compaction moisture contents the low dry density is caused by the presence of large air-filled macropores" (1, p. 1195). In addition, the macropeds, or clusters of clay particles, are able to resist the compaction pressure without much distortion. As the water content is increased, the macropores become filled with soil (easy slippage); the result is an increase in density. As the water content is increased further, the water layers increase in thickness, and the aggregates, easily distorted, fuse together making them indistinguishable. This, in turn, decreases compacted density (1).

Hodek (2) explained the characteristics and engineering behavior of a compacted soil in terms of a deformable aggregate model. He concluded that this model is appropriate to use in interpreting swell and compaction characteristics of a laboratory static compacted kaolinite. His theory of the compaction process is similar to that of Barden and Sides.

According to Garcia-Bengochea (3), pore-size distribution measurements for compacted clays have also provided strong evidence for a deformable aggregate model. He cites Bhasin (4) who found that as the compactive effort increases, the fraction of pores on the dry side of optimum decreases, whereas, on the wet side, the distribution remains the same. These findings are of interest because they directly affect compacted clay permeability, which, in turn, directly affects the rate of compressibility of compacted clay.

Hodek and Lovell (5) have proposed a model that explains the achievement of compacted unit weight for the laboratory static compaction of kaolinite. They propose that the initial soil fabric of the as-molded soil (before compaction) is that of aggregations of different size and water content. The size and distribution of these aggregates play an important role in the compaction process; that is, densification is associated with the decrease in interaggregate void ratio due to translation and rotation, the deformation of aggregates into the shape of available voids, and the reduction of intra-aggregate voids. Accordingly, the type of compaction and the aggregate-size distribution establish the fluid and continuity condition within the mass, and, once the air voids are no longer interconnected, little densification occurs regardless of the input effort. Hodek and Lovell (5) also introduce the concept of net energy imparted to the soil during the compaction process. It was found that the net energy required to obtain different conditions on the same moisture-density curve is inversely proportional to the aggregate size; uncomplicated mathematical models were developed to show this relationship.

Compressibility Characteristics

During the compaction process, the soil experiences the load for only a short time. The energy supplied in this short period is received by the soil skeleton, as an intergranular stress, and the pore fluids, as a pressure in each of the phases. Upon completion of the process, there is an induced prestress in the soil; this prestress may or may not be equal to the compaction pressure. According to Abeyesekera (6), it is this value of compactive prestress that is important with respect to compacted clay behavior.

Woodsum (7) defined compactive prestress as analogous to the preconsolidation pressure of a natural soil; specifically, the apparent pressure effect caused by the compaction process. Lambe (8) similarly defined compactive prestress but realized that its value was affected by other factors, namely, time and chemical changes. For the purposes of this study, the compactive prestress will be defined as the precompression pressure, in terms of total stress, that has been induced in the soil as a result of the compaction process and is determined on an as-compacted oedometer specimen directly after compaction.

To determine compactive prestress Woodsum (7) statically compacted Fort Union clay and Mississippi loess directly in oedometer rings, allowed the soil to come to equilibrium with water under an applied load, and performed the conventional oedometer test. The data showed that as the confining pressure (P_o) remained constant and, as the compaction pressure (P_c) increased or the initial void ratio (e_o) decreased, the value of prestress increased. Moreover, the data suggest that although the value of prestress increased with increasing compaction pressure, the prestress ratio (P_s/P_c), which is similar to the overconsolidation ratio for saturated soils, varied slightly not increasingly as might be expected. This may mean that, for a given compaction process and type of soil, the efficiency of the process does not increase with increasing effort.

Abeyesekera (6) determined the prestress induced by the kneading compaction of a shale material. The material was compacted at pressures ranging from 345 kN/m² to 1380 kN/m² (50 to 200 psi) and loaded in the as-compacted condition, either incrementally in the oedometer or at constant rate of strain. The elapsed time for each oedometer load increment was 10 minutes--the same loading time used by Yoshimi and Osterbert (9). The estimated prestress was determined in terms of total stress from the void ratio-log pressure curve using the Casagrande construction.

In the seven tests performed, Abeyesekera (6) found the prestress values and the prestress ratio to range from 345 kN/m² to 865 kN/m² (50 to 126 psi) and 0.49 to 1.0, respectively. The ratio range is greater than Woodsum's (0.1 to 0.2). The difference in ratio range may be attributable to the differences between kneading and static methods, shale and clay, unsoaked condition and soaked condition, either singly or in combination. However, some interesting correlations can be made with Abeyesekera's results.

Table 1 summarizes the results of other investigators who were concerned with the compressibility of compacted materials but not specifically with compactive prestress. If only the data related to soils are examined, it can be seen that static compaction methods are the most efficient with respect to induced prestress. Seed, Mitchell, and Chan (10) examined the effect of the difference in compaction method on the undrained shear strength of compacted clay; they found that static compaction resulted in smaller shear strains, lower pore water pressures, and higher strength values at low strains and that kneading compaction resulted in larger shear strains, higher pore water pressures, and lower strength at low strains. This appears to be a reasonable explanation of differences in statically induced prestress and prestress induced by kneading methods.

EXPERIMENTAL APPARATUS AND PROCEDURE

The soil used in this study was obtained from Perry County, Indiana. It will hereafter be referred to

Table 1. Compaction pressure and prestress (6).

Investigator	Material	Compaction Mode	Compaction Pressure [P_c (psi)]	Dwell Time (sec)	Prestress Values [P_s (psi)]	Prestress Ratio (P_s/P_c)
Cambell (1952)	Bituminous concrete	Static	2,500	60	150-210	0.06-0.08
Yoshimi and Osterberg (1963)	Silty clay	Static (20 psi/min)	94	280	94	1.00
Mishu (1963)	Residual clay	Kneading (30 blow/min)	95	1	36.1	0.38
			125	1	36.1	0.29
			170	1	55.6	0.33
Abeyesekera (1978)	Shale aggregate	Kneading (30 blow/min)	50	1	50	1.00
			100	1	68-74	0.68-0.74
			200	1	98-126	0.49-0.63

as St. Croix clay. The St. Croix clay is medium gray-brown at its natural moisture content. It is classified as a fat clay (CH) and falls within the AASHTO classification of an A-7-6 material.

The kneading method of compaction was selected for use in this study for two reasons: (a) The compaction characteristics obtained are comparable, for the same soil, to those obtained by sheepsfoot- and pneumatic-type rollers on actual earthen embankments, and (b) the degree of uniformity with respect to moisture content and density is greater than that of other methods.

The soil was compacted in 5 approximately equal layers at a rate of 30 tamps per minute per layer. Between layers, the top surface was scarified to ensure compacted mass homogeneity. A constant compaction pressure was maintained throughout the process; the value was based on moisture-density relations for the impact method. The results and implications of this procedure will be discussed later.

Typically, density and water content are the prescribed elements in an end-result approach and are based on results obtained by the laboratory impact method. It was therefore considered appropriate to use the impact moisture-density relations as a base reference for the kneading method.

The moisture-density curves for the three basic impact energy levels used are shown in Figure 1. Each energy level is characterized as follows.

1. Low-energy Proctor--304.8 mm (12 in.) drop, 24.5N (5.5 lb) rammer, 3 layers, 15 blows per layer.
2. Standard Proctor--304.8 mm drop, 24.5N rammer, 3 layers, 25 blows per layer.
3. Modified Proctor--457.2 mm (18 in.) drop, 44.5N (10 lb) rammer, 3 layers, 25 blows per layer.

The compaction assembly and procedure were as specified in AASHTO T99070; however, fresh samples were used for each point on the curve.

A series of kneading compaction tests was performed on the St. Croix clay using different compaction pressures. For each pressure a moisture-density relation was obtained for a range of moisture contents between 4 percent wet and dry of optimum. These relations were correlated approximately to the three impact levels to select a kneading compaction pressure that would produce the same densities at equivalent water contents.

A fixed-ring consolidation cell was used in this study; it will be referred to as an "oedometer" in subsequent discussions. The oedometer ring was 63.5 mm (2.50 in.) in diameter, 2.54 mm (1 in.) in height, and 19.1 mm (0.75 in.) in wall thickness. Following a seating load adjustment period (typically 10 min), the applied pressure on the compacted sample was increased, using a load increment ratio (LIR) of 0.5 to 15.2, 22.6, 34.0, 49.5, 76.5 kN/m², and so on until the prestress value for the particular sample could be well defined. The duration of each load was 10 minutes; dial readings were typically recorded at 0, 0.1, 0.5, 1, 2, 4, 8, and 10 minutes.

Figure 1. Moisture-density-energy relations for impact method (11).

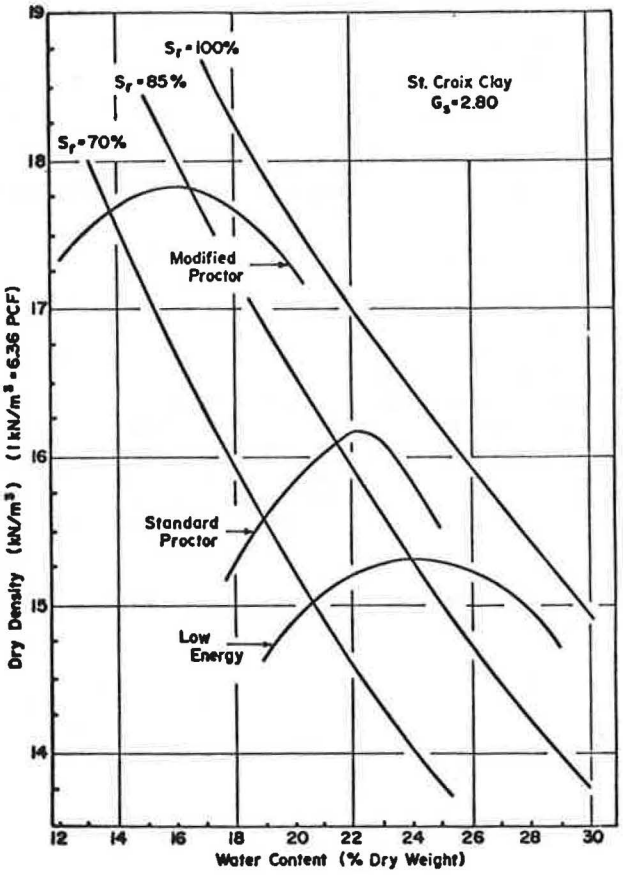

The 10-minute load duration criterion was based principally on the findings of Yoshimi (12). To determine what load increment ratio to use for the as-compacted compression test, it was decided that the following requirements should be met.

1. A large portion of the compression must take place within 10 minutes.
2. As few loads as possible should be used, to limit moisture loss by evaporation.
3. The prestress value should be accurately defined using the Casagrande construction.

If an LIR = 1 were used, the first and second requirements would be satisfied; however, the third requirement might not be, based on the results of

Leonards and Girault (13) for determining the preconsolidation value for saturated soils. If an LIR = 0.1 or 0.2 were used, the third requirement would be satisfied, but the first and second requirements would not be (12). Ideally, a load increment ratio equal to actual field loading conditions should be used; however, this ratio is dependent on a given application and may be difficult to determine. An LIR = 0.5 was chosen because it most suitably matched the requirements.

RESULTS

As-Compacted Compressibility

The compaction variables used to characterize each as-compacted compressibility test sample are defined as follows.

1. Water content (w,%)--the average of the as-compacted moisture determinations.
2. Dry density (γ_d, kN/m³)--the dry density of the oedometer sample computed from its unit weight, water content (w), and volume.
3. Compaction pressure (P_c, kN/m²)--the maximum dynamic kneading foot pressure applied during compaction, expressed nominally.

The other computed variables were initial degree of saturation (S_r,%) and initial void ratio (e_o). Both were calculated from the first and second variables just defined.

The compaction water contents ranged between 4 percent wet and dry of optimum and were based on the results of the impact method. Thirty-two as-compacted compressibility tests were performed; the values of the previously defined compaction variables are listed in Table 2. In this table and in subsequent discussions the sample number characters are defined as follows: L, S, M represent the compaction condition corresponding to the equivalent low-energy, standard Proctor, and modified Proctor impact levels, respectively. D, O, or W represent dry, at, or wet-of-optimum conditions, respectively; and 1, 2, ..., and so forth represent the sample number for that condition. For example, the sample designated MD1 is the first sample compacted to a dry of optimum condition using an equivalent modified Proctor kneading compaction pressure.

Table 2. Initial compaction variables for as-compacted compressibility samples (11).

Sample No.	Water Content (%)	Dry Density γ_d (kN/m³)	Compaction Pressure P_c (kN/m²)	Degree of Saturation S_r (%)	Initial Void Ratio e_o
LD1	20.60	13.97	460	59.77	0.9649
LD2	20.60	14.85	525	65.26	0.8838
LD3	20.51	14.27	426	62.15	0.9240
LO1	23.26	15.74	426	80.14	0.8126
LO2	23.85	15.77	558	89.62	0.7451
LO3	24.27	14.91	683	80.68	0.8423
LW2	27.94	14.88	525	92.47	0.8460
LW3	26.98	14.82	657	88.42	0.8544
SD4	18.95	15.26	788	66.40	0.7990
SD8	19.38	14.62	788	61.82	0.8770
SD9	19.59	15.06	788	66.58	0.8238
SD10	19.37	15.65	788	71.87	0.7545
SO3	12.37	15.76	657	80.61	0.7423
SO8	21.71	15.78	657	82.02	0.7411
SO9	21.21	15.99	657	82.70	0.7180
SO11	21.65	15.72	814	81.12	0.7473
SO12	22.32	16.15	788	89.20	0.7066
SO13	22.67	16.25	762	92.92	0.6905
SO16	22.68	15.97	762	88.18	0.7202
SW2	25.38	15.24	722	88.67	0.8014
SW3	25.71	15.13	722	88.27	0.8155
SW4	25.05	15.42	722	89.80	0.7810
SW6	24.72	15.64	722	91.49	0.7565
SW7	24.87	15.38	722	88.66	0.7854
SW8	24.71	15.68	722	92.08	0.7514
MD1	14.67	18.31	3191	82.10	0.5003
MD2	13.96	17.65	3071	70.23	0.5565
MO1	16.20	17.97	2905	85.90	0.5281
MO2	15.71	18.10	2735	85.10	0.5168
MW1	19.59	16.99	2466	87.85	0.6243
MW3	19.74	16.87	2439	88.05	0.6277
MW5	19.57	16.86	2466	87.18	0.6285

Figure 2 shows the effects of increasing water content and degree of saturation on compressibility behavior for samples compacted to equivalent standard Proctor conditions. As may be inferred, there is a marked difference in the compressibility behavior for wet- and dry-side samples depending on the range of consolidation pressure considered. That is, in the low-pressure range, the wet-side sample is more compressible than the dry-side sample, whereas in the high range the opposite is true.

Lambe (8,14) explained this behavior in terms of compacted clay structure, colloidal chemistry, and soil-particle rearrangement. However, more recently, Hodek and Lovell (15) examined this behavior in terms of pore-size distribution, pore-size magnitude, and deformable aggregate theory. Based on supporting evidence (2,3,16), their explanation can be stated as follows.

1. Dry-side compressibility--the pores are typically large and numerous; the clay aggregates are shrunken, hard, and brittle; compressibility is governed by the collapse of large pores under straining.
2. Wet-side compressibility--the pores are small and numerous; the clay aggregates are swollen and plastic; compressibility is governed by the fusing of aggregates under load.

In view of this explanation, a dry-side sample would compress less in the low-pressure range due to the large intergranular forces resulting from the many well-developed menisci. However, on loading, these forces are overcome, and the brittle aggregates displace into adjacent pores. Consequently, a large amount of compression occurs because of the large amount of available interaggregate pore space. On the other hand, a wet-side sample compresses more in the low-pressure range because of the smaller number of developed menisci (high degree of saturation) and less in the higher range because of the relatively small number of large interaggregate pores.

Figure 3 shows the effect of increasing compaction pressure on the compressibility behavior of samples compacted near optimum. The slope of the curves within the respective high-pressure ranges becomes steeper (i.e., increasingly more negative) with decreasing compaction pressure. With respect to the structural models previously discussed, this suggests that for dry-side samples the magnitude and frequency of the large pore mode decreases with increasing compaction pressure.

Compactive Prestress

The results presented in the previous section illustrate compressibility behavior within specific ranges of applied pressure. However, an important characteristic not considered is the value of compactive prestress. Clearly, its value could be useful in design, because the compressibility behavior of the mass may be different at embankment confining pressures above and below this value. That is, each specific value of compactive prestress, as determined in the manner presented in this section, is the approximate pressure value

Figure 2. Effect of moisture content on compressibility (standard Proctor) (11).

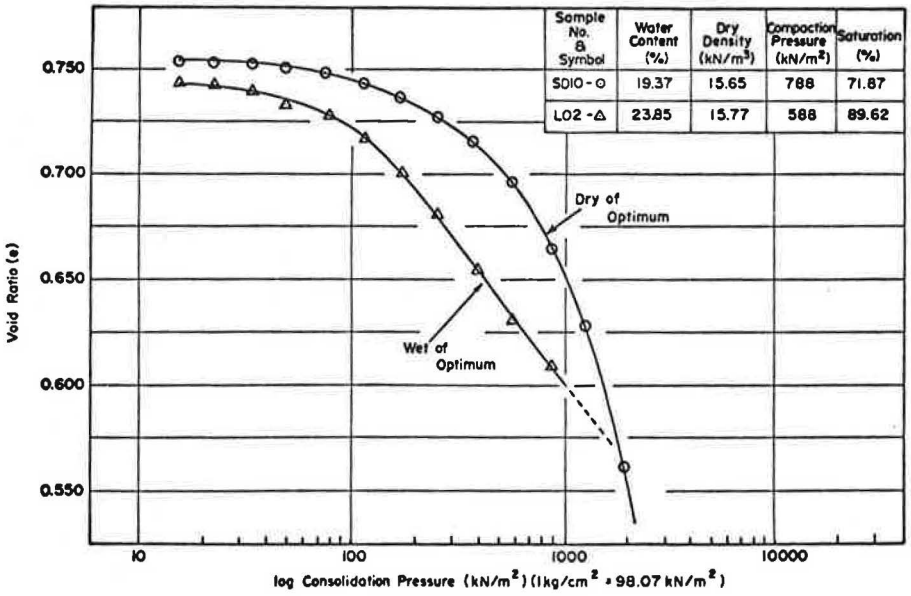

Figure 3. Effect of compactive effort on compressibility (near optimum) (11).

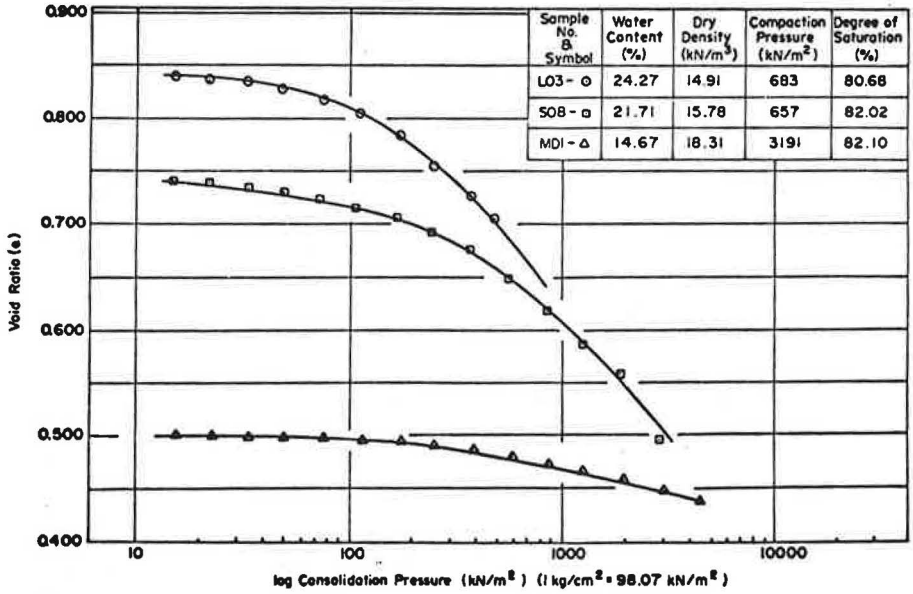

below and above which low-range compressibility behavior and high-range compressibility behavior, respectively, occur.

The value of compactive prestress (P_s) and the prestress ratio (P_s/P_c) for each of the thirty-two as-compacted compressibility test samples are listed in Table 3. Each value of compactive prestress was determined from its corresponding e-log p curve using the Casagrande approximation commonly employed for determining the most probable preconsolidation pressure for saturated soils. In the strictest sense, its use may be unjustified. However, the current state of the art is such that little is known of the fundamental relationships governing unsaturated compression.

Figure 4 shows the values of compactive prestress plotted at their respective values of water content, dry density, and equivalent impact effort level. The 87 percent saturation curve was arbitrarily selected and plotted in this figure and, for the purpose of this discussion, will be referred to as a means of separating wet and dry compaction conditions.

From Figure 4, the following general conclusions may be drawn with respect to prestressing capacity.

1. For dry of optimum conditions (S_r < 87%): (a) At a given equivalent impact effort level, as the water content increases, the value of compactive prestress decreases. (b) As the equivalent impact effort increases, the value of compactive prestress also increases.

2. For wet of optimum conditions (S_r > 87%): (a) At a given equivalent impact effort level, the capacity for prestressing is small and remains virtually unchanged with increasing water content. (b) As the equivalent impact effort level increases, the capacity for prestressing is virtually unchanged.

Table 3. Values of compactive prestress and prestress ratio (11).

Sample No.	Compactive Prestress [P_s (kN/m2)]	Compaction Pressure [P_c (kN/m2)]	Prestress Ratio (P_s/P_c)	Degree of Saturation [S_r (%)][a]
LD1	290	460	0.63	59.8
LD2	315	525	0.60	65.3
LD3	220	426	0.52	62.2
LO1	185	426	0.43	80.1
LO2	155	588	0.26	89.6
LO3	85	683	0.12	80.7
LW2	76	525	0.14	92.5
LW3	72	657	0.11	88.4
SD4	505	788	0.64	66.4
SD8	470	788	0.60	61.8
SD9	490	788	0.62	66.6
SD10	500	788	0.63	71.9
SO3	410	657	0.62	80.6
SO8	340	657	0.52	82.0
SO9	235	657	0.36	82.7
SO11	105	814	0.13	81.1
SO12	95	788	0.12	89.2
SO13	105	762	0.14	92.9
SO16	125	762	0.16	88.2
SW2	95	722	0.13	88.7
SW3	135	722	0.19	88.3
SW4	80	722	0.11	89.8
SW6	160	722	0.22	91.5
SW7	90	722	0.12	88.7
SW8	55	722	0.08	92.1
MD1	830	3191	0.26	82.1
MD2	1120	3071	0.36	70.2
MO1	1030	2905	0.35	85.9
MO2	1100	2753	0.40	85.1
MW1	85	2466	0.03	87.9
MW3	86	2439	0.04	88.1
MW5	150	2466	0.01	87.2

[a]The degrees of saturation were rounded to the nearest tenth.

Figure 4. Prestress values (kN/m2) for as-compacted compressibility tests (11).

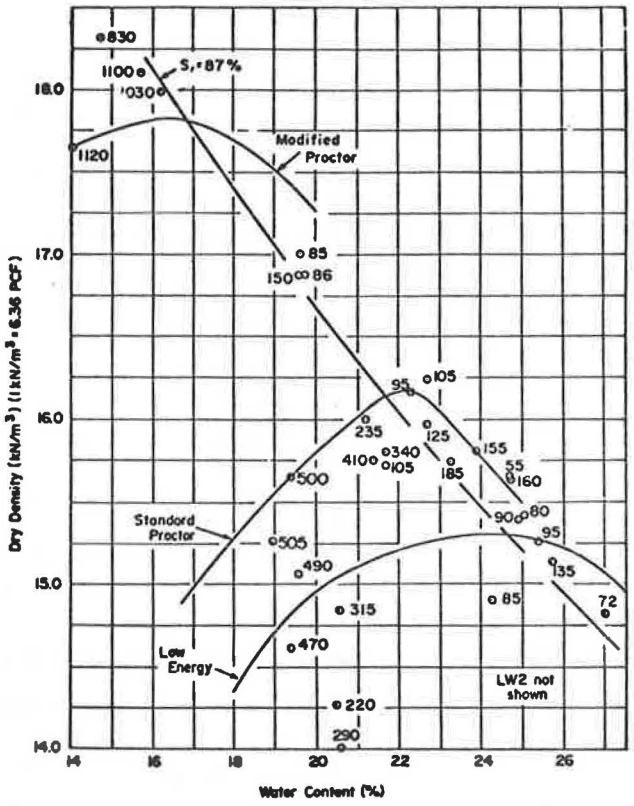

This suggests that at dry-side water contents, prestressing capacity is largely affected by compaction water content and compaction pressure. In addition, compactive prestress is little affected by water content and compaction pressure for initially wet samples. Finally, for the range of saturation considered in this study, the prestress ratio is always less than one, which may indicate that not all of the energy delivered is achieving densification.

In this connection, it is important to realize that the compaction pressures reported here are only nominal pressures; that is, they are the pressures expended by the kneading compactor during the compaction process. Therefore, the actual prestress ratios (i.e., compactive prestress/effective compaction pressure) are more than likely greater than the values presented here.

Statistical Correlations

The predictive models presented here were developed using the Statistical Package for the Social Sciences (SPSS) procedural programs on Purdue University software. It should be mentioned that any best model isolated by these programs is highly dependent on the procedure used, and an equivalent model may not be established given another set of procedures.

The first phase of the isolation process involved plotting the independent variables against the dependent variable. This was facilitated using the SPSS procedure SCATTERGRAM. If the scatter plots showed a linear relationship, the independent variable was considered highly correlated with the dependent variable. If a linear trend was not found, the independent variable was considered statistically insignificant.

The next step was to isolate a subset of the independent variables considered highly correlated with the dependent variable, so that an optimal expression with as few variables as possible could be established. This was achieved using the automatic SPSS search procedure STEPWISE. This procedure combines a forward inclusion of independent variables already in the model at each successive step. In addition, it conducts a statistical test to screen out any independent variable that is too highly correlated with the independent variables already in the model.

The final step of the isolation process was to obtain the best estimated prediction model from the subset of independent variables isolated by the STEPWISE procedure. This was done using the SPSS procedure REGRESSION [developed by Nie, et al. (17)]. Various regression equations were obtained using different combinations. From these, the procedure for selecting the best model was based on the following statistical criteria.

1. For the overall multiple regression equation, (a) The coefficient of multiple determination (R^2) is greater than 0.65; that is, at least 65 percent of the variation must be explained by the variables included in the model. (b) The adjusted coefficient of multiple determination (R^2_a) must increase with each additional independent variable entered in the model. (c) The overall F-test at the $\alpha = 0.05$ significance level must be met. (This tests for multiple linearity of the model.)

2. For the partial regression coefficients, (a) The F-test for each partial regression coefficient at the $\alpha = 0.05$ significance level must be met. (This tests whether an independent variable should be dropped from the model.) (b) The coefficients of partial determination ($r_{i.jk}$) are significant. (c) The 95 percent confidence limit for each b_i is

small and does not cross zero. [This restriction is similar to (a).]

3. For the computed residuals, (a) The scatter plots of the residuals versus the independent variable(s) show normal constancy of variance trends. (b) The residuals are normally distributed random variables; that is, the values of e_k/MSE (residuals divided by the error root mean square) must range between ±3.

When all criteria were suitably met by more than one model, the model with the fewest variables was selected, provided there was no appreciable difference (i.e., less than 5 percent) in either of the R^2 or R^2_a values.

Based on the foregoing, the following prediction model was selected for compactive prestress (P_s).

$$P_s = -343.13 - 0.0020w^2 \cdot P_c + 48.91\, P_c^{1/2}$$

where

P_s = estimated value of compactive prestress in kN/m²,
$w^2 \cdot P_c$ = interaction term between water content (%) squared and compaction pressure (kN/m²), and
$P_c^{1/2}$ = the square root of compaction pressure $(kN/m^2)^{1/2}$.

The R^2 value was 88 percent. In addition, all of the other statistical criteria were suitably met. A graphic representation of this relationship is presented in Figure 5.

As shown in this figure, for a given water content the estimated compactive prestress increases with increasing compaction pressure. Woodsum (7) and Abeyesekera (6) obtained similar results. Also, for a given compaction pressure an increase in water content is accompanied by a decrease in compactive prestress. More clearly, at a given effort level, an increase in water content reduces prestressing capacity.

Figure 5. Prediction of compactive prestress (11).

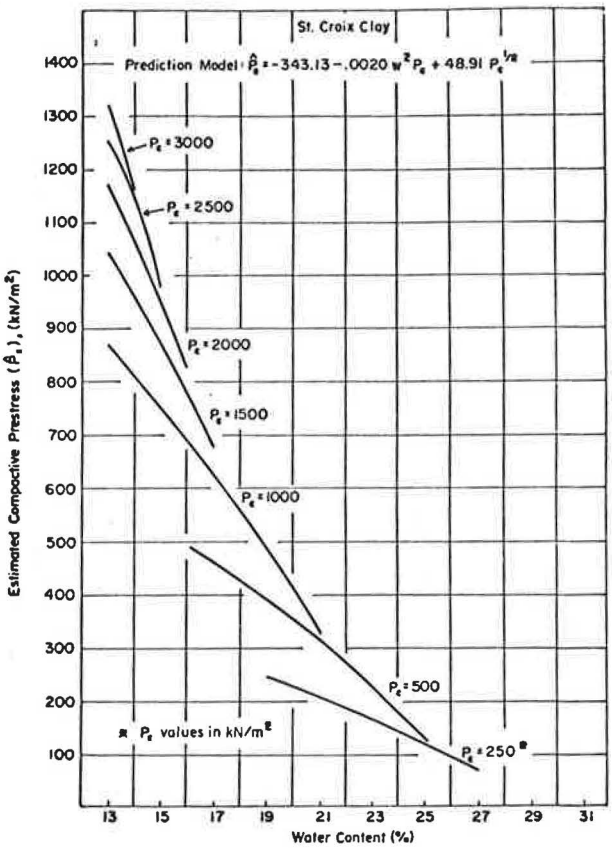

The relations shown in Figure 5 are not entirely applicable for the values of water content and compaction pressure plotted. Rather, they are applicable only for a joint region of observations; that is, the region covered by both independent variables (18). Neither model can be used with confidence in design until the results presented here are correlated with results for field-compacted samples of the same soil. Such research is currently in progress at Purdue University.

CONCLUSIONS

The experimental and statistical results of this study lead to the following conclusions.

1. For an increasing water content and equivalent impact level, the as-compacted compressibility behavior was in agreement with the results presented by Wilson (19), Lambe (8), and Wahls et al. (20). It is believed that this behavior can be explained in view of more recent evidence (1,5,15) concerning compacted clay macrostructure.
2. Dry of optimum, the value of compactive prestress decreased with increasing water content and increased with increasing equivalent impact effort level. Wet of optimum, the value of compactive prestress was not influenced appreciably by varying the initial compaction variables.
3. For the range of partial saturation considered, the ratio of compactive prestress to nominal compaction pressure was less than unity. This ratio tended to decrease with increasing initial degree of saturation.
4. The best predictive model for compactive prestress was isolated using the SPSS procedures SCATTERGRAM, STEPWISE, and REGRESSION. The proposed model was statistically valid and accurate.

ACKNOWLEDGMENT

The authors are grateful to the Indiana State Highway Commission and the Federal Highway Administration for the financial sponsorship of this study. The research was administered through the Joint Highway Research Project, Purdue University, West Lafayette, Indiana.

The contents of this paper reflect the view of the authors who are responsible for the facts and the accuracy of the data presented.

REFERENCES

1. L. Barden and G.R. Sides. Engineering Behavior and Structure of Compacted Clay. Journal of the Soil Mechanics and Foundations Division, ASCE, Vol. 96, No. SM4, 1970, pp. 1171-1200.
2. R.J. Hodek. Mechanism for the Compaction and Response of Kaolinite. Purdue Univ., West Lafayette, Ind., Joint Highway Research Project, Rept. 72-36, Dec. 1972.
3. I. Garcia-Bengochea. The Relation Between Permeability and Pore Size Distribution of Compacted Clayey Silts. Purdue Univ., West Lafayette, Ind., Joint Highway Research Project, Rept. 78-4, May 1978.
4. R.N. Bhasin. Pore Size Distribution of Compacted Soils After Critical Region Drying.

Purdue Univ., West Lafayette, Ind., Joint Highway Research Project, Rept. 75-3, May 1975.
5. R.J. Hodek and C.W. Lovell. Soil Aggregates and Their Control Over Soil Compaction and Swelling. TRB, Transportation Research Record 733, 1979, pp. 94-99.
6. R.A. Abeyesekera. Stress Deformation and Strength Characteristics of a Compacted Shale. Purdue Univ., West Lafayette, Ind., Joint Highway Research Project, Rept. 77-24, May 1978.
7. H.C. Woodsum. The Compressibility of Two Compacted Clays. Master's thesis, Purdue Univ., West Lafayette, Ind., 1951.
8. T.W. Lambe. The Engineering Behavior of Compacted Clay. Journal of the Soil Mechanics and Foundations Division, ASCE, Vol. 84, No. SM2, 1958, pp. 1-35.
9. Y. Yoshima and J.D. Osterberg. Compression of Partially Saturated Cohesive Soils. Journal of the Soil Mechanics and Foundations Division, ASCE, Vol. 89, No. SM4, 1963, pp. 1-23.
10. H.B. Seed, J.B. Mitchell, and C.K. Chan. The Strength of Compacted Cohesive Soils. Research Conference on Shear Strength of Cohesive Soils, Boulder, Colo., 1960, pp. 877-964.
11. A. DiBernardo and C.W. Lovell. The Effect of Laboratory Compaction on the Compressibility of a Compacted Highly Plastic Clay. Purdue Univ., West Lafayette, Ind., Joint Highway Research Project, Rept. 79-3, Feb. 1979.
12. Y. Yoshimi. One Dimensional Consolidation of Partially Saturated Soil. Ph.D. diss., Northwestern Univ., Evanston, Ill., 1958.
13. G.A. Leonards and P. Girault. A Study of the One-Dimensional Consolidation Test. Proc., Fifth International Conference on Soil Mechanics and Foundation Engineering, Paris, Vol. 1, 1961, pp. 213-218.
14. T.W. Lambe. The Structure of Compacted Clay. Journal of the Soil Mechanics and Foundations Division, ASCE, Vol. 84, No. SM2, 1958, pp. 1-34.
15. R.J. Hodek and C.W. Lovell. A New Look at Compaction of Landfills. Presented at AEG Conference, Hershey, Pa., Oct. 18, 1979.
16. M.A. Reed. Frost Heaving Rate of Silty Soils as a Function of Pore Size Distribution. Purdue Univ., West Lafayette, Ind., Joint Highway Research Project, Rept. 77-15, 1977.
17. N.H. Nie, et al. Statistical Package for the Social Sciences. 2nd ed. McGraw-Hill, New York, 1975.
18. J. Neter and W. Wasserman. Applied Linear Statistical Models. Irwin, Homewood, Ill., 1974.
19. S.L. Wilson. Effect of Compaction on Soil Properties. Proc., Conference on Soil Stabilization, MIT, Cambridge, Mass., 1952, pp. 148-158.
20. H.E. Wahls, C.P. Fisher, and L.J. Langfelder. The Compaction of Soils and Rock for Highway Purposes. FHWA-RD-73-8, 1966.

Publication of this paper sponsored by Committee on Earthwork Construction.